UNIVERSITÀ
DEGLI STUDI
DI BRESCIA

DOTTORATO DI RICERCA IN

INGEGNERIA DELL'INFORMAZIONE

settore scientifico disciplinare

Experimental Physics (FIS/01)

CICLO

XXXVI

TITOLO TESI

Fabrication and Characterization of Metal Oxides for their Gas Sensor and Li-ion Battery Applications

NOME DEL DOTTORANDA

Hakimeh Pakdel

NOME DEL Primo SUPERVISORE

Prof. Elisabetta Comini

NOME DEL Co-SUPERVISORE

Dr. Vardan Galstyan

Abstract

This thesis explores the applications of metal oxide nanomaterials in gas sensing and Li-ion batteries. It presents a detailed exploration of their state-of-the-art, definitions, and mechanisms. The focus is on tungsten trioxide (WO_3), zinc oxide (ZnO), copper oxide (CuO), and vanadium pentoxide (V_2O_5), analyzing their crystalline structures, properties, and potential applications. The thesis covers the synthesis methods and the functional applications of these materials in gas sensing and battery technology.

Traditional methods for synthesizing WO_3 involve hazardous substances, raising environmental and health concerns. This study proposes an eco-friendly synthesis using water and vitamin C as a green surfactant. The research examines the growth mechanism, particularly the surfactant's role in nanoparticle formation. The monoclinic WO_3 synthesized through this method shows high sensitivity and selectivity to acetone, with stable performance across various humidity levels. This contributes to green synthesis procedures for WO_3 nanomaterials, enhancing their application in gas sensors.

The thesis investigates the impact of crystalline phase junctions on the gas sensing performance of WO_3. Two samples synthesized without and with PEG 200, were analyzed. XRD and Raman spectroscopy confirmed monoclinic and monoclinic-orthorhombic phases. ATR-FTIR spectroscopy provided insights into the materials' vibrational characteristics and chemical composition. Gas sensing experiments revealed that WO_3 with PEG 200, exhibited superior acetone sensitivity at higher operating temperatures. The inhibition of hydrate formation and the presence of ortho/mono n-n homojunction improved hydrate adsorption, enhancing sensitivity. The gas sensing performance across different humidity levels (40 to 95%) indicates its potential for breath analysis.

Another study addresses the critical need for effective nitrogen dioxide (NO_2) detection for human health and environmental sustainability. The study focuses on the synthesis of a novel CuO-ZnO composite through a polyol and sol-gel technique. The controlled synthesis of hierarchical CuO and porous ZnO structures using the polyol technique, coupled with sol-gel

composite formation, proves effective in enhancing gas sensing performances, including sensitivity, selectivity, and low detection limits for NO_2. The composite displays excellent selectivity towards NO_2, contributing to advancements in gas sensor technology for sensitive and selective NO_2 detection.

Finally, the thesis explores the synthesis and electrochemical analysis of porous V_2O_5 microsheets as anode materials in Li-ion batteries. Addressing challenges like poor conductivity and limited cycling stability, the study tailored the synthesis to achieve specific microstructures and high porosity. Two samples were prepared at two different reaction temperatures, showcasing porous microsheet structures with their crystallinity and morphologies. Electrochemical analysis indicated stable redox behavior, multiple-phase transitions, and superior specific capacities for V_2O_5 (which is synthesized at lower temperatures) at high current densities. This research highlights the potential of microstructures to improve Li-ion battery efficiency and stability.

Abstract Italiano

Questa tesi esplora le applicazioni dei nanomateriali di ossidi metallici nella rilevazione di gas e nelle batterie agli ioni di litio. Presenta un'esplorazione dettagliata dello stato dell'arte, delle definizioni e dei meccanismi. L'attenzione è rivolta al triossido di tungsteno (WO_3), all'ossido di zinco (ZnO), all'ossido di rame (CuO) e al pentossido di vanadio (V_2O_5), analizzando le loro strutture cristalline, proprietà e potenziali utilizzi. La tesi copre i metodi di sintesi e le applicazioni funzionali di questi materiali nella rilevazione di gas e nella tecnologia delle batterie.

I metodi tradizionali per la sintesi del WO_3 coinvolgono sostanze pericolose, sollevando preoccupazioni ambientali e sanitarie. Questo studio propone una sintesi ecocompatibile utilizzando acqua e vitamina C come tensioattivo verde. La ricerca esamina il meccanismo di crescita, in particolare il ruolo del tensioattivo nella formazione delle nanoparticelle. Il WO_3

monoclino sintetizzato con questo metodo mostra alta sensibilità e selettività all'acetone, con prestazioni stabili a diversi livelli di umidità. Questo contribuisce alle procedure di sintesi ecologica per i nanomateriali di WO_3, migliorando la loro applicazione nei sensori di gas.

La tesi indaga l'impatto delle giunzioni di fase cristallina sulle prestazioni di rilevazione dei gas del WO_3. Sono stati analizzati due campioni sintetizzati senza e con PEG 200. La spettroscopia XRD e Raman ha confermato le fasi monoclina e monoclina-ortorombica, rispettivamente. La spettroscopia ATR-FTIR ha fornito informazioni sulle caratteristiche vibrazionali e sulla composizione chimica dei materiali. Gli esperimenti di rilevazione dei gas hanno rivelato che il WO_3 con PEG 200 ha mostrato una sensibilità superiore all'acetone a temperature operative più elevate. L'inibizione della formazione di idrati e la presenza di omo-giunzioni n-n orto/mono hanno migliorato l'adsorbimento degli idrati, aumentando la sensibilità. Le prestazioni di rilevazione dei gas a diversi livelli di umidità (dal 40 al 95%) indicano il suo potenziale per l'analisi del respiro.

Un altro studio affronta la necessità cruciale di una rilevazione efficace del diossido di azoto (NO_2) per la salute umana e la sostenibilità ambientale. Lo studio si concentra sulla sintesi di un nuovo composito CuO-ZnO attraverso una tecnica di poliolo e sol-gel. La sintesi controllata di strutture gerarchiche di CuO e di ZnO poroso utilizzando la tecnica del poliolo, accoppiata con la formazione del composito sol-gel, si dimostra efficace nel migliorare le prestazioni di rilevazione dei gas, inclusi sensibilità, selettività e limiti di rilevazione bassi per il NO_2. Il composito mostra un'eccellente selettività verso il NO_2, contribuendo ai progressi nella tecnologia dei sensori di gas per una rilevazione sensibile e selettiva del NO_2.

Infine, la tesi esplora la sintesi e l'analisi elettrochimica di microfogli porosi di V_2O_5 come materiali anodici nelle batterie agli ioni di litio. Affrontando sfide come la scarsa conducibilità e la stabilità limitata del ciclo, lo studio ha adattato la sintesi per ottenere microstrutture specifiche e alta porosità. Sono stati preparati due campioni a due diverse temperature di reazione, mostrando strutture di microfogli porosi con la loro cristallinità e morfologie. L'analisi elettrochimica ha indicato un comportamento redox stabile, transizioni di fase multiple e capacità specifiche superiori per il V_2O_5 (sintetizzato a temperature più basse) a densità di

corrente elevate. Questa ricerca evidenzia il potenziale delle microstrutture per migliorare l'efficienza e la stabilità delle batterie agli ioni di litio.

Acknowledgment

I would like to express my sincere gratitude to my supervisor, Prof. Elisabetta Comini, for her invaluable guidance, expertise, and support throughout conducting and completing this research. Her dedication to excellence, patience, and encouragement have been instrumental in shaping this thesis.

I extend my sincere appreciation to my co-supervisor, Dr. Vardan Galstyan, for his insightful contributions and dedicated involvement in steering this research. His expertise has added a valuable dimension to the depth and quality of this thesis.

I am thankful to Prof. Dario Zappa for his invaluable contributions to our research endeavors in the Sensor lab. Special thanks to Nicola Poli and Matteo Borsi as a technician of Sensor Lab for their invaluable help and support. I am grateful to Stefano Lupi, Annalisa D'Arco, and Tiziana Mancini at the University of Rome ‘La Sapienza’ (Physics Department) for RAMAN and ATR-IR measurement. I would like to say thanks to Vyacheslav Golovanov for the DFT calculation.

I extend my heartfelt gratitude to Prof. Nicola Pinna and Yanchen Liu at Humboldt-Universität zu Berlin (Institut für Chemie & IRIS Adlershof) for their invaluable collaboration and expertise in guiding the electrochemical measurements for the Li-ion battery and hosting me in prof. Pinna laboratory. Their profound insights and commitment have significantly enhanced the precision and reliability of our research. Special thanks to Christoph Erdmann for his invaluable contributions to conducting the TEM measurements in Prof. Pinna's Laboratory.

I would like to express my appreciation to the members of the sensor lab, Dr. Federica, Massimo, Hadjer, Marwa, Hicham, Safia, Stefano, Dr. Chathuranga, Dr. Abderrahim, Dr.

Navpreet, Dr. Om Pal, Alessandro, Abbas, and Saeideh for their collaboration and friendship throughout our research journey.

Thanks to all members of Prof. Pinna's laboratory for their friendship, which made my stay enjoyable in Berlin.

I express my deepest appreciation to my parents, Hossein and Melika, for their support, love, and sacrifices throughout my academic journey. Their belief in my potential has inspired me to strive for excellence. I am also grateful to my siblings, Zahra, Reza, and Mohammadhadi, for their encouragement and companionship. Their love and support have played a pivotal role in my accomplishments. I am grateful to my friends, whose support, encouragement, and companionship have been a constant source of joy and strength throughout my journey.

Contents

List of Figure

List of Table

Introduction and objectives

In recent years, the rapid pace of industrialization and the widespread use of energy has resulted in severe air pollution, an issue with multifaceted implications, affecting not only the environment but also social, economic, and ecological systems. The consequences of air pollution extend beyond environmental hazards to include risks to human health and the economy. Recognizing these consequences, international organizations and governments have increasingly prioritized addressing air pollution through various initiatives and policies.

The global concerns about the consequences of air pollution have prompted significant international initiatives and resolutions. The journey began with the issuance of WHO air quality guidelines in 2010, followed by subsequent UNEA conferences in 2014, 2016, and 2017 that underscored the commitment to combat air pollution. Reports and evaluations, such as Action Air Quality and The Process of Air Pollution Control in Beijing, highlighted both global and localized perspectives on air quality measures. International conferences, including the Global Conference on Air Pollution and Health in 2018, aimed at achieving substantial reductions in air pollution-related deaths by 2030. The 2021 release of the Air Pollution Series by UNEA emphasized the global concern surrounding air pollution, prompting a comprehensive review of air quality legislation worldwide. This underscores the imperative to address air pollution as a critical global environmental and health challenge.

Sensors could detect toxic gases to improve human safety and environmental protection. Therefore, it is urgent to develop gas sensors for the detection of NO_2, CO, CO_2, NH_3, O_3, Volatile Organic Compounds (VOCs), H_2S, and H_2, each characterized by different and specific threshold limit values of exposure. Metal oxides play an important role in sensing materials due to their low cost, small size, ease of fabrication, stability, reproducibility, and abundance. Consequently, metal oxide semiconductor materials have received extensive attention due to their application in various fields, including solar cells, Li-ion batteries, electrocatalysts/photocatalysts for water splitting and gas sensing applications.

There is a growing demand for green chemistry, which has been intensified to reduce the utilization and production of hazardous substances. Green synthesis methods, aligned with the twelve fundamental principles of green chemistry, have emerged as crucial pathways to achieve this goal. These methods prioritize the fabrication of nanostructured materials without hazardous organic solvents, corrosive acids (e.g., HNO_3, HCl, or H_2SO_4), and non-toxic reagents, thereby minimizing reliance on harmful substances. Therefore, our studies are focused on developing different gas sensing materials, including metal oxides and their composites, using environmental friendly and cost-effective sol-gel and polyol methods to enhance gas sensing performance.

The imperative to create new methods for generating and storing energy arises from the need to decarbonize our future energy supply. Given the massive threat of climate change, we need new ways to make and store energy. The global effort to reduce our dependency on finite fossil fuels and mitigate their environmental effects, such as carbon dioxide emissions, has led to a strong emphasis on scientific research. These studies are aimed at advancing renewable energy sources. It is crucial that we prioritize the development of energy storage solutions alongside the progress in technologies for harvesting renewable energies like solar and wind power. Thus, this development can effectively and securely store electrical energy over extended periods. Lithium-ion batteries have emerged as a key player in this transition. Lithium-ion batteries play a critical role in the global transition to cleaner and more sustainable energy systems. Their ability to store electrical energy ensures a steady supply of power from renewable sources, reduces carbon emissions and promotes a greener future for generations to come.

In response to the demand for Li-ion batteries characterized by heightened energy and power densities, along with enhanced stability, the development of next-generation Li-ion batteries emerges as a critical pursuit. Within the key components of these batteries, the anode plays a pivotal role, and conventional materials like graphite encounter limitations in capacity, rate capability, and safety. Transition metal oxides (TMOs) have attracted attention for their substantial theoretical capacities and distinctive electrochemical properties. Among various VO_x materials, V_2O_5 stands out due to its high theoretical capacity and volume stability, despite facing challenges in conductivity and cycling stability. While extensively studied as a cathode

material, V_2O_5's potential as an anode material remains relatively unexplored. This thesis aims to unlock the potential of V_2O_5 as an anode material for Li-ion batteries by designing specific porous microstructures. Through tailored microstructures, the objective is to optimize the charge transport mechanism, ultimately leading to improved capacities and steady cycling performance of V_2O_5 anodes.

This thesis aims to develop high-performance chemical gas sensors and advanced Li-ion battery materials through the exploration of semiconductor metal oxide nanomaterials and their synthesis methods. Accordingly, the thesis is structured into eight chapters dedicated to specific facets of chemical gas sensors and lithium-ion battery materials, as outlined below.

Chapter 1:

Provides a comprehensive overview of chemical gas sensors, focusing on semiconductor-based sensors, highlighting their properties such as sensitivity, stability, selectivity, and miniaturization potential. Additionally, it discusses the historical perspective and key components of Li-ion batteries, emphasizing the importance of understanding materials and measurement techniques.

Chapter 2:

Explores the advantages of nanomaterials in gas sensors and battery technologies, detailing the crystalline structures, properties, and potential applications of tungsten trioxide, zinc oxide, copper oxide, and vanadium pentoxide.

Chapter 3:

Reports synthesis methods for metal oxide nanoparticles and instrumental setups for gas sensor fabrication and Li-ion batteries anode preparation, providing a foundation for exploring specific metal oxide structures and their applications in subsequent chapters.

Chapter 4:

Focuses on the successful synthesis of WO_3 nanoparticles using an environmentally friendly method and their high sensitivity towards acetone, indicating potential applications in gas sensors for medical diagnostics and environmental monitoring.

Chapter 5:

Examines the gas sensing performance and phase junction formation of WO_3 nanoparticles with PEG 200 as a surfactant, elucidating their enhanced sensitivity to acetone and the role of crystalline modification in gas sensing.

Chapter 6:

Explores CuO-ZnO composites for gas sensing applications, detailing their characteristics and excellent selectivity to NO_2, suggesting practical environmental monitoring applications.

Chapter 7:

Investigates V_2O_5 microsheets as an anode material for Li-ion batteries, demonstrating superior performance in terms of rate capability, cycling stability, and charge transfer kinetics, suggesting its potential for high-performance lithium-ion batteries.

Chapter 8:

Concludes the findings of the previous seven chapters, integrating their contributions to the fields of gas sensing and energy storage.

Chapter 1: Chemical Gas Sensor and Lithium-ion Batteries: State of the art and their mechanisms

Introduction

This chapter explores the state-of-the-art in metal oxide gas sensors and Li-ion batteries, encompassing their definition and mechanisms. It delves into the components and performance characteristics of semiconductor sensors, highlighting the advantages of semiconductor metal oxide sensors over alternative technologies. The discussion extends to conductometric sensors, explaining gas sensing mechanisms. Furthermore, the chapter outlines how parameters such as temperature, humidity, additives, and composite materials impact the gas sensors performance, emphasizing the necessity for precise control to achieve accurate measurements.

The chapter further investigates the key components of Li-ion cells, emphasizing the roles of anodes, cathodes, electrolytes, and separators. It also discusses significant aspects, including the formation of the solid-electrolyte interphase and various electrochemical measurement techniques essential for evaluating battery performance.

1.1 Chemical Gas sensor

1.1.1 State of the art on Chemical sensor

In 1952, Brattain and Bardeen published alterations in the conductivity of germanium-based semiconductors due to changes in the oxygen partial pressure within the environment [1]. A decade later, Seiyama reported the gas sensing capabilities of metal oxides [2]. Subsequently, Taguchi introduced metal oxide semiconductor gas sensors to the market, utilizing an alumina ceramic tube equipped with the metal oxide, electrodes, and a heating coil running through it. In 1969 he established Figaro Engineering Inc., the leading global semiconductor gas sensor producer [3].

1.1.1.1 Definition

A chemical sensor is a specialized device designed to detect and quantify the presence of specific chemical substances in the environment. It operates by converting the chemical information of the target analyte into a measurable signal, typically an electrical or optical output, which can then be interpreted to determine the concentration or identity of the substance of analytes [4]. Typically, a chemical sensor consists of three fundamental components call as receptor, transduce and packaging module.

1. Receptor

The receptor is the component which is responsible for interacting with the target analyte. It is designed to have a specific affinity for the chemical information, which allows it to adsorb the analyte molecules. Receptors can be organic or inorganic materials, such as enzymes, antibodies, polymers, or metal oxide, tailored to react with particular chemicals or chemical groups [5].

2. Transducer

The transducer is the central component responsible for converting the chemical signal generated by the receptor into a quantifiable output signal. This conversion is typically achieved using physical or chemical changes induced by the receptor and analyte interaction. Transducer types vary widely and can include electrochemical, optical, piezoelectric, or conductive elements, depending on the sensor's design and intended application [6, 7].

3. Packaging Module

The packaging module, also known as the housing or encapsulation, provides protection and stability to the sensor's internal components. It shields the receptor and transducer from external factors such as humidity, temperature, and mechanical stress, which can affect the sensor's performance.

1.1.1.2 Semiconductor performance characteristics

The performance characteristics of semiconductor sensors, including response, response and recovery times, selectivity, stability, and repeatability determine their suitability for various applications. Semiconductor-based sensors are widely used for a variety of applications, and their performance characteristics are crucial for determining their effectiveness in specific tasks. Five key performance characteristics of semiconductor sensors are defined below [8-10]:

1. Response

   Response is a fundamental performance characteristic of semiconductor sensors, representing how effectively the sensor reacts with the target analyte (gas or chemical). The sensing response of the n-type materials toward reducing and oxidizing gases is calculated according to Equations 1 and 2, respectively:

   $$\frac{(G_{f-}G_0)}{G_0} = \frac{\Delta G}{G_0} \quad (1)$$

   $$\frac{(\mathrm{G_{0-}\,G_f})}{G_f} = \frac{\Delta \mathrm{G}}{\mathrm{G_f}} \quad (2)$$

   Here, $\mathrm{G_0}$ is the baseline conductance of the semiconductor metal oxide sensor in air and $\mathrm{G_f}$ the steady-state conductance value of the sensor in the presence of the analyte.

2. Response and Recovery Times

   The response time of a sensor corresponds to its reaction time when exposed to an analyte. It is specifically defined as the duration required for the sensor to achieve a stable value in the presence of the analyte. We will define it at the time required to reach 90% change in its final conductance while the gas is present. Conversely, the recovery time is related to the time necessary for the sensor to recover its initial value in air after the analyte is removed. We will define it as the time required for the sensor to reach 70% of the initial conductance variation during the recovery. The response and recovery times are essential parameters for assessing how quickly a semiconductor sensor can adapt to changes in analyte concentration and return to its initial state.

3. Selectivity

   Selectivity refers to a sensor's ability to distinguish between the target analyte and other interfering substances present in the environment. A highly selective semiconductor sensor

will respond primarily to the intended analyte, even in the presence of potential interferences. Achieving good selectivity often involves using specific receptor materials that interact selectively with the target analyte, minimizing false readings caused by cross-reactivity with other compounds.

4. Stability

   Stability is a critical performance characteristic that reflects the sensor's ability to maintain its sensing characteristics over time without significant degradation. Stable semiconductor sensors deliver reliable measurements throughout their operational lifetime. Factors that can affect stability include temperature, humidity, exposure to contaminants, and the materials used in the sensor's fabrication.

5. Repeatability

   Repeatability assesses the consistency of a semiconductor sensing parameters when exposed to the same analyte concentration under the same conditions. Repeatability is a key factor for ensuring the reliability of sensor data and minimizing measurement errors.

1.1.1.3 Advantage of semiconductor metal oxide sensors compared to other technologies

Semiconductor metal oxide sensors offer a range of advantages when compared to various other sensing technologies, including GC-mass spectroscopy, electrochemical sensors, catalytic combustion, thermal conductive sensors, and infrared absorption sensors. The advantages of semiconductor metal oxide sensors are [7, 11]:

- Sensitivity: Semiconductor metal oxide sensors are highly sensitive to a wide range of gases and volatile compounds, making them suitable for detecting low concentrations of analytes.
- Stability: They exhibit good long-term stability, maintaining their sensitivity and performance over extended periods, which is critical for continuous monitoring of analytes.

- Selectivity: While not as selective as some other technologies like GC-mass spectroscopy, semiconductor sensors can be tailored for selectivity through specific material, allowing them to distinguish between certain gaseous compounds.
- Response time: Semiconductor metal oxide sensors offer rapid response times, often in seconds, making them suitable for real-time monitoring.
- Accuracy: They provide acceptable accuracy for many applications.
- Durability: These sensors are robust and can withstand a range of environmental conditions, making them suitable for harsh or remote monitoring.
- Maintenance: Semiconductor metal oxide sensors require minimal maintenance and calibration, contributing to their cost-effectiveness in long-term use.
- Cost: They are generally more cost-effective compared to other analytical techniques like GC-mass spectroscopy, making them accessible for a wider range of applications.
- Miniaturization: Semiconductor sensors can be easily miniaturized, allowing the development of portable and wearable devices for environmental monitoring and medical diagnostics.

Therefore, semiconductor metal oxide sensors strike a balance between sensitivity, selectivity, cost-effectiveness, and ease of use, making them suitable for a wide range of applications, especially where real-time monitoring, durability, and low maintenance are essential. However, the choice of sensor technology should depend on the specific requirements and constraints of the given application.

1.1.2 Conductometric Sensor

A conductometric sensor is a type of chemical sensor that measures changes in the electrical conductivity of a sensitive material when exposed to gases (as explained in the definition of chemical gas sensor). These sensors consist of several key components such as sensing material, electrodes, heaters each playing a crucial role in their measurement [12]. Accordingly, it's important to include a brief description of the role of each component in this section.

1. Sensing Material

   Common sensing materials include metal oxides (such as tin dioxide, and tungsten oxide), polymers, and even enzymes or antibodies in some biosensors. The choice of sensing material depends on the specific application and the type of analyte to be detected. Metal oxides are a class of materials that have attracted significant attention for their use as sensing materials in various types of gas sensors.

2. Electrodes

   Electrodes play a crucial role in measuring electrical properties during the interaction process. Interdigital electrodes, commonly composed of materials like gold (Au) and platinum (Pt), exhibit a comb-like arrangement with closely spaced finger-like structures. These gaps facilitate analyte interaction, providing a substantial electrical contact area. The preference for Au and Pt in interdigital electrodes is attributed to their chemical stability, corrosion resistance, and low electrical resistance. These properties make them suitable for various sensing applications, especially in microfabricated devices where small feature sizes and low power consumption are essential. Au and Pt can be efficiently deposited onto substrates such as silicon wafers, alumina, and glass using common microfabrication techniques like sputtering [13]. While these materials offer advantages, it's essential to acknowledge their limitations, such as higher material costs compared to other metals. The choice of the metal for interdigital electrodes depends on specific application requirements, including desired electrode properties (such as stability, conductivity, biocompatibility) and budget considerations [14].

3. Insulating substrate

   The insulating substrate serves as the physical support for the electrodes and sensing material. It ensures that the electrical current flows through the desired path and prevents unintended electrical connections. Common insulating substrates include ceramic materials, glass, or polymers. The substrate also provides mechanical stability to the sensor and may be designed to withstand harsh environmental conditions [10].

4. Heater

   Some conductometric sensors, especially those for gas detection, include a heater to regulate the operating temperature of the sensing material. Metal oxide gas sensors often require operating temperatures between 200 and 500 °C for optimal performance, depending on design and target gases. The heater ensures a consistent and elevated temperature, crucial for reliable chemical reactions between target gases and the sensing material. Maintaining a constant temperature helps minimize the impact of environmental factors, such as temperature fluctuations and humidity changes, ensuring the sensor provides stable and repeatable readings over time [15, 16].

1.1.2.1 Gas sensing mechanisms

The gas sensing mechanism of metal oxide sensors relies on two distinct phenomena called chemisorption and physisorption. These processes play a fundamental role in the sensor's ability to detect specific gases in its environment [17, 18].

1. Chemisorption

   Chemisorption is a chemical interaction between gas molecules and the surface of the metal oxide sensing material. In this process, gas molecules form strong chemical bonds with the atoms or sites on the surface of the metal oxide. These bonds often involve the transfer of electrons, resulting in the formation of charged species on the sensor's surface. This interaction causes changes in the electrical properties of the metal oxide, such as its conductivity or resistance. Chemisorption typically requires a certain amount of energy to overcome activation barriers, enabling gas molecules to bond with the metal oxide surface. This energy can be provided by increasing operating temperatures in metal oxide gas sensors. Also, chemisorption is highly specific to the types of gas molecules and the nature of the metal oxide surface. Different metal oxides exhibit various affinities for specific gases, allowing for tailored selectivity in gas sensors. Chemisorption-based reactions are often reversible. When the gas is removed from the

sensor's environment, the chemical bonds break, and the conductivity of sensor returns to its initial state. This reversibility is essential for continuous monitoring applications.

2. Physisorption

   Physisorption, in contrast to chemisorption, involves weaker physical interactions between gas molecules and the metal oxide surface. In physisorption, gas molecules are adsorbed onto the sensor's surface through van der Waals forces interactions. These interactions do not result in significant electron transfer or chemical bonding. Physisorption requires less energy compared to chemisorption, and it can occur at lower temperatures. Some metal oxide sensors may employ this phenomenon for specific gas detection purposes. Physisorption is generally non-specific, meaning that it can occur with a wide range of gas molecules. This can make sensors relying on physisorption less selective, but it can be advantageous in some applications requiring broad-range gas detection. Physisorption-based interactions are also typically reversible, allowing the sensor to return to its original state when the gas concentration decreases.

By incorporating both chemisorption and physisorption mechanisms, metal oxide gas sensors can achieve a balance between sensitivity and selectivity. The sensor's response to different gases is influenced by the interplay between these two mechanisms, making metal oxide sensors versatile and applicable in various gas sensing scenarios.

1.1.2.2 Oxygen adsorption on the surface of semiconductors

Oxygen adsorption on the surface of semiconductors is a critical process that plays a significant role in various technological applications, especially in the development of gas sensors and semiconductor devices. Understanding how oxygen interacts with semiconductor surfaces is essential for optimizing the performance of these materials. The interaction between oxygen present in the atmosphere and the surface of the sensing material, in accordance with Equations 3−8, plays a fundamental role in the process of semiconducting metal oxide gas sensors [19]. When a n-type semiconducting metal oxide such as SnO_2 is exposed to the surrounding air, oxygen is adsorbed on its surface in molecular, atomic, or ionic form by

accepting electrons from the semiconductor (Equations 3−8). This process leads to a reduction in conductivity or an increase in the electrical resistance of the n-type semiconductors.

$$O_2(gas) \leftrightarrow O_2(ads) \quad (3)$$

$$O_2(ads) + e^- \leftrightarrow O_2^-(ads) \quad (4)$$

$$O_2(ads) + e^- \leftrightarrow O_2^{2-}(ads) \quad (5)$$

$$O_2^-(ads) + e^- \leftrightarrow 2O^-(ads) \quad (6)$$

$$O^-(ads) + e^- \leftrightarrow O^{2-}(ads) \quad (7)$$

$$O^{2-}(ads) \leftrightarrow O^{2-}(lat) \quad (8)$$

Depending on the operating temperature of the sensor, different oxygen species can be stable on the surface of SnO_2 (Figure 1.1). The most stable species ion is O^- at temperatures higher than 150 °C. At temperatures below 150 °C, O_2^- is more stable [20, 21].

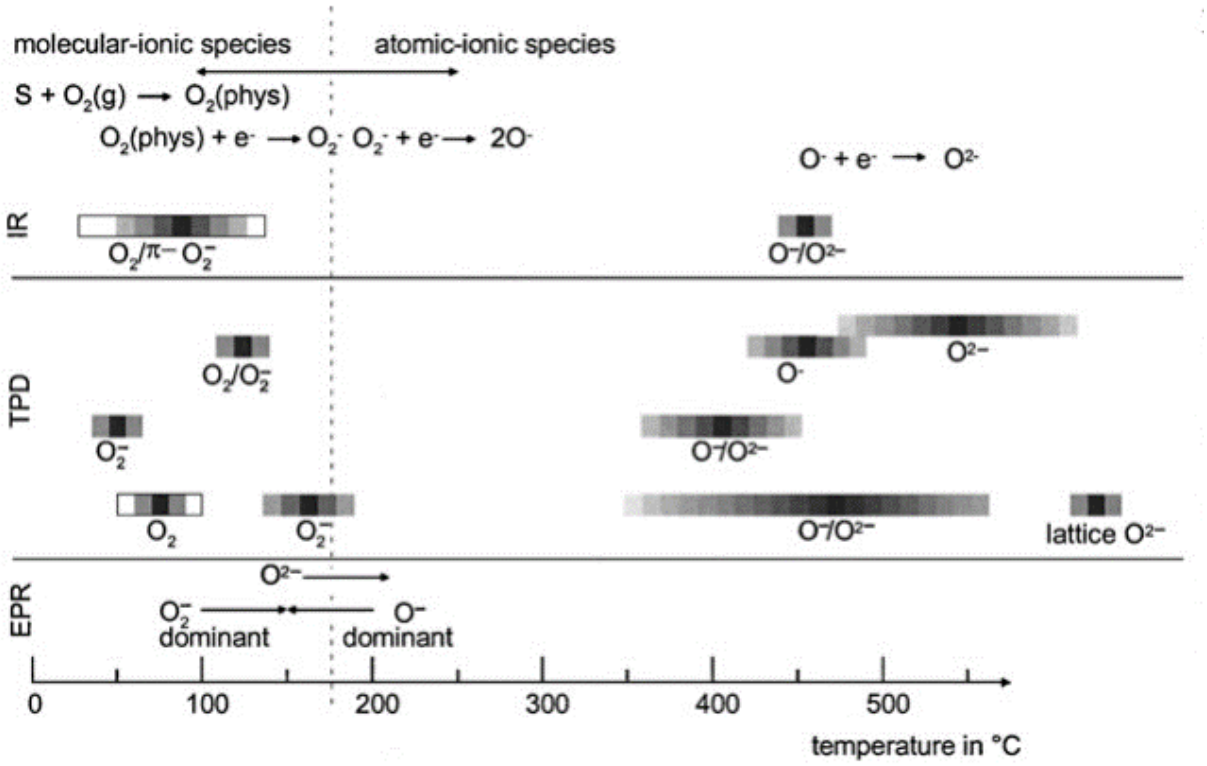

Figure 1.1 Schematic of oxygen species detected at different temperatures at SnO_2 surfaces with IR (infrared analysis), TPD (temperature programmed desorption), EPR (electron paramagnetic resonance) [19].

1.1.2.2.1 Effect of oxygen adsorption on semiconductor surfaces

1. Effects on electronic properties

- Charge transfer: Oxygen adsorption can introduce additional charge carriers (electrons or holes) into the semiconductor material. For n-type semiconductors, where electrons are the predominant carriers, their interaction with oxygen molecules from the surrounding air induces a modification in electrical conductance. This change occurs due to the formation of an electron-depletion layer (EDL) on the semiconductor's surface. This depletion layer arises because electrons move from the conductance band to the adsorbed oxygen molecules, driven by the oxygen's high electron affinity. This results in the formation of an electronic core-shell configuration (as depicted in Figure 1.2a). Specifically, it leads to the formation of an n-type semiconductor region within the core of the particles, while the shells of the particles exhibit resistive behavior (EDL). In contrast, p-type semiconductors primarily contain holes as their majority carriers. When oxygen is adsorbed onto the surface of p-type semiconductors, it leads to an increase in the concentration of holes in the valence band. This phenomenon occurs as electron trapping by oxygen ion adsorption. Thus, an accumulation layer of holes forms, known as the holes accumulation layer (HAL). This accumulation of holes serves to enhance the semiconductor's electrical conductance when exposed to air, resulting in higher overall electrical conductivity. Once again, this establishes the electronic core-shell configuration, where the central regions of the particles act as insulators, while the surface of the particles contains semiconducting HALs (Figure 1.2b) [22].

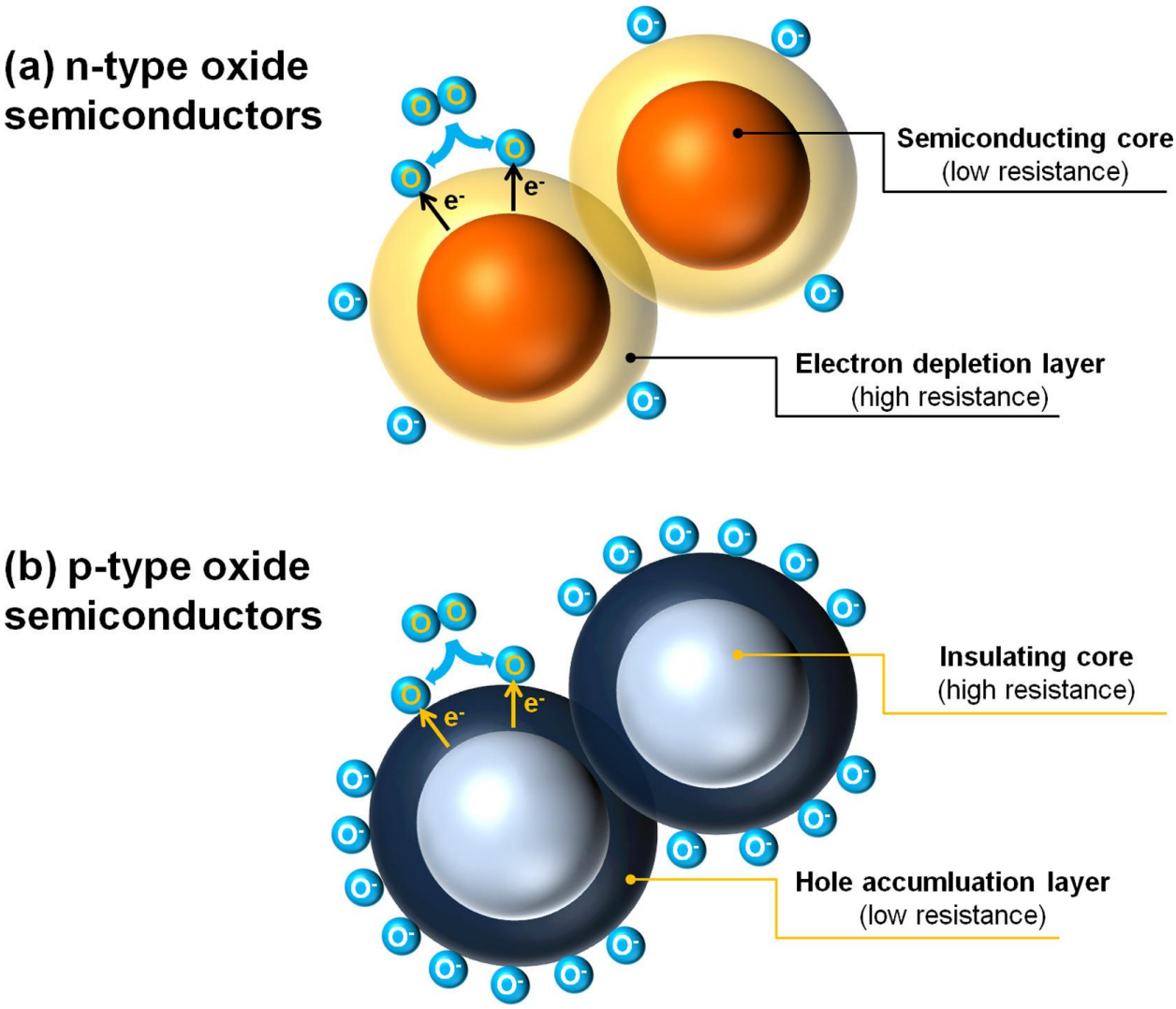

Figure 1.2 Formation of electronic core–shell structures in (a) n-type and (b) p-type oxide semiconductors [20].

- Band structure modification: Oxygen adsorption can modify the band structure of the semiconductor, affecting its electronic properties. For example, it can shift the energy levels of the semiconductor's conduction and valence bands, influencing its conductivity and optical properties [23].

2. Surface reactivity

Oxygen adsorption can also influence the reactivity of the semiconductor surface. For example, the presence of oxygen atoms on the surface can enhance the surface's catalytic activity, making semiconductors valuable materials for catalysis and photocatalysis applications [24].

3. Passivation

Oxygen can also act as a passivating agent on semiconductor surfaces. By adsorbing oxygen, semiconductor surfaces can be protected from contamination and the formation of defects. This passivation is particularly important for maintaining the long-term stability and reliability of semiconductor devices [25].

Oxygen adsorption on semiconductor surfaces is a complex process that can have a profound impact on the electronic, optical, and chemical properties of the material. Understanding the mechanisms and consequences of oxygen adsorption is essential for designing and optimizing semiconductor devices, including gas sensors and photocatalysts.

1.1.2.3 The effect of different parameters on gas sensing performance

The performance of gas sensors is influenced by various parameters and conditions, including temperature, humidity, the addition of dopants, and the preparation of composite materials. These factors play a critical role in determining the sensor's performance like sensitivity, and selectivity. Here is an overview of how each parameter affects gas sensing performance.

1. Temperature

Temperature significantly impacts gas sensor performance. Most gas sensors, especially metal oxide sensors, operate at elevated temperatures (typically 200−500 °C). Increasing the operating temperature can enhance the sensitivity and response time of the sensor by promoting gas-surface interactions [26]. Higher temperatures may increase sensitivity but can also lead to accelerated sensor aging or unwanted side reactions. Operation at lower temperatures saves energy, prolongs operating lifetime, and ensures consistent reproducibility by avoiding sintering-induced grain growth. Optimization of the operating temperature is crucial for achieving the desired balance between sensitivity and sensor longevity [27]. Temperature affects the physical properties of semiconductors (thermal energy excites electrons from the valence band to the conduction band, increasing electrical conductivity). It also influences surface reactions on semiconductors. As previously mentioned, according to Equations 3−8 and Figure 1.1, the

adsorption of oxygen species and their surface reactions are temperature-dependent. Therefore, processes like adsorption and desorption, surface coverage by molecular and ionic species, chemical decomposition, and gas oxidation on the semiconductor surface are highly dependent on the operating temperature of the sensor. Sensor performance, typically assessed in terms of sensitivity and dynamic response (response time and recovery time), is directly related to the mechanisms and kinetics of surface reactions [26, 28]. Therefore, the sensor's performance is a function of its operating temperature.

2. Humidity

Humidity levels in the sensor's environment can influence its performance, especially for humidity-sensitive sensors. High humidity can interfere with the sensor's response to target gases, usually leading to reduced sensitivity. In general, several reasons contribute to this reduction in sensitivity: Firstly, the baseline resistance of the gas sensor decreases due to the reaction between surface oxygen and water molecules. Secondly, the adsorption of water molecules on the sensor's surface hinders the chemisorption of oxygen ions, resulting in a reduction in the active surface area of the sensing layer, consequently affecting the gas sensor's performance. Additionally, the presence of water molecules on the sensor's surface creates a barrier that makes it challenging for gas molecules to adsorb on the sensor's surface, leading to decreased sensitivity and longer response/recovery times. Furthermore, prolonged exposure to humidity leads to the formation of a stable chemisorbed OH^- layer on the sensor's surface, further deteriorating its sensing performance [29]. However, these surface OH^- groups can desorb when the sensor is heated to temperatures exceeding 400 °C, and complete removal occurs at temperatures higher than 400 °C. It is worth mentioning that the interaction of water molecules and other gaseous compounds with the surface of materials is a complex process and can be influenced by various factors, including operating conditions. Also, water may act as a catalyzer for the interaction between the analyte and the surface of the material [30].

An increase in humidity leads to the formation of different surface species, each with its own impact. One of these species contributes to a charge transfer with the conduction band, resulting in a reduction in band bending. Simultaneously, another species forms local dipoles,

causing an increase in electron affinity. It is worth noting that these measurements alone do not provide direct insights into the specific types of surface species present. To address this, various researchers have devised models to elucidate the interaction between water and metal oxide surfaces [31].

3. Additives

The addition of dopants to the sensing material can improve a sensor's response, sensitivity, and selectivity to specific gases. Dopants can create defects or alter the electronic properties of the material, affecting its gas sensing behavior. The selection and concentration of dopants are critical [32]. Dopants can be used to enhance the sensor's affinity for particular gases or improve its performance under specific conditions [33]. Also, combining different materials to form composites can improve gas sensor performance including sensitivity, selectivity, and stability compared to single-component sensors. They may also enable the detection of a broader range of gases. The preparation of composite materials involves choosing compatible components and optimizing their proportions. Composite sensors can be engineered to exhibit synergistic effects, resulting in superior gas sensing properties. The enhancements in the gas sensing performance of composite materials can be ascribed to several factors. These factors include electronic influences, such as band bending caused by Fermi level alignment, separation of charge carriers, manipulation of depletion layers, and the increase in potential barrier energy at interfaces; chemical effects, such as a reduction in activation energy, catalytic activity, and surface reactions; geometrical aspects, such as increased surface area, and improving gas accessibility [34].

Understanding how temperature, humidity, dopants, and composite materials affect gas sensing performance allows the development of sensors tailored to specific applications, ranging from environmental monitoring to industrial safety and medical diagnosis. Proper control of these parameters is critical to ensure accurate and reliable gas measurements.

1.2 Li-ion batteries

1.2.1 State of the art on Li-ion battery

The initial lithium-metal battery, comprising lithium metal and manganese dioxide as electrodes, was developed back in 1962 and later introduced to the commercial battery market by Sanyo in 1972 [35]. Utilizing a metallic lithium electrode offers certain advantages, such as lithium being the lightest metal, boasting a high theoretical capacity of 3860 Ah/g, and having an extremely low electrode potential (-3.04 V vs. the standard hydrogen electrode, SHE). However, there are significant challenges associated with the use of metallic lithium due to its substantial volume changes and high reactivity during the electrochemical process, which can lead to the growth of dendrites. These dendrites can cause short-circuits, thermal runaway, and even pose a fire hazard. Given the inherent instability of metallic lithium, research efforts shifted towards exploring alternative electrode materials. Initially, the focus was on replacing displacement-type cathodes [36]. A pivotal breakthrough in transitioning from lithium-metal batteries to lithium-ion batteries occurred when John B. Goodenough introduced the intercalation/insertion type electrode using TiS_2 at Exxon in 1976 [37]. However, these early lithium-ion batteries had a drawback in their low cut-off voltage, measuring just 2.5 V vs. Li/Li^+, which limited their ability to achieve high energy density.

1.2.1.1 Definition

A lithium-ion battery, often abbreviated as Li-ion battery, is a rechargeable energy storage device that is employed in modern electronics and electric vehicles due to its high energy density and relatively low self-discharge rate. It provides a portable and efficient means of storing electrical energy for various applications. When a lithium-ion battery is charged, lithium ions are released from the anode and move through the electrolyte to the cathode. This process is reversed during discharge when the battery provides electrical power. The movement of lithium ions back and forth between the anode and cathode is what enables the battery to store and release electrical energy. A Li-ion cell comprises four primary components: the negative electrode (anode), electrolyte, separator, and positive electrode (cathode). These terms are

specifically defined in the context of the discharge process, during which the anode undergoes an oxidation reaction, while the reduction reaction takes place on the cathode side [35, 38].

Externally, the electrodes are linked to form an electron circuit that performs tasks within the connected load. A widely used commercial battery configuration involves a cathode made of $LiCoO_2$ and an anode constructed from graphite. Normally, the electrolyte consists of organic liquids like alkyl carbonates, combined with lithium salts such as $LiPF_6$ in an ionically dissociated state [39]. This combination facilitates the transfer of lithium ions between the electrodes. The operating voltage of the cell is determined by both the cathode and anode. Lithium ions move through the electrolyte to incorporate themselves into the cathode, while electrons generate a current through the external circuit, as shown in Figure 1.3. The cathode typically contains a transition metal, which undergoes reduction during discharge, allowing the incorporation of one lithium ion into the structure for each electron accepted by the transition metal ion. In summary, during battery discharge, the anode undergoes oxidation, and the cathode experiences reduction. Reversible chemical reactions occur at both the anode and cathode as lithium is removed/added and electrons are gained/lost, resulting in structural changes. Rechargeable batteries are recharged by applying a controlled over-potential from an external power source [40]. This causes electrons and lithium ions to flow back from the cathode to the anode, where they combine to form lithium metal that intercalates into the porous anode structure (Figure 1.3).

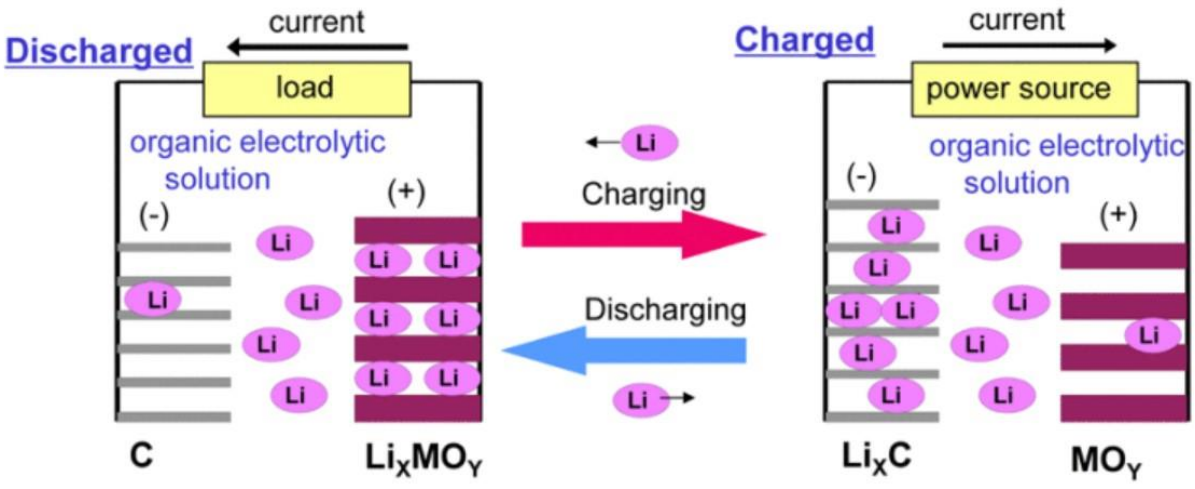

Figure 1.3 Principle of Li-ion batteries [38].

Both the anode and cathode must exhibit excellent electronic conductivity, allowing electrons to move freely throughout the electrodes via external current collectors. The electrolyte should function as an electronic insulator; otherwise, the cell could short-circuit. Furthermore, the cathode, anode, and electrolyte should facilitate the easy diffusion of lithium ions within the materials, with minimal volume and structural changes occurring during lithium (de)intercalation. As the electrolyte contacts the surfaces of both electrodes, it must remain stable to minimize adverse side reactions with the electrodes [41].

1. Anode: The negative electrode, or anode, is typically made of a material that can intercalate or absorb lithium ions when the battery is charging. Common anode materials include graphite and various forms of carbon. During discharge, lithium ions move from the anode to the cathode through the electrolyte. Vanadium oxides (VO_x) have attracted significant attention and found widespread applications in catalysis and energy storage due to their distinctive layered structure, multiple oxidation states (III-V), earth abundance, and low cost. Among the various VO_x materials, Vanadium pentoxide (V_2O_5) has emerged as a promising candidate anode for energy storage [42]. V_2O_5 is a promising material for application in lithium-ion batteries due to its high oxidation state of vanadium, enabling the storage of a greater number of electrons per formula unit, despite facing challenges related to poor conductivity and limited cycling stability [43]. Thus, V_2O_5 can be employed as an anode.

2. Electrolyte: The electrolyte is a crucial component of a Li-ion battery as it facilitates the movement of lithium ions between the anode and cathode during charge and discharge cycles. It is an ion-conductive material, typically a lithium salt dissolved in a solvent. The ideal lithium salt for use in Li-ion battery electrolytes should meet several crucial criteria [44].

(i) The lithium salt should readily dissolve in the chosen solvent to facilitate high mobility of Li^+ ions.

(ii) The anion of the lithium salt should be resistant to oxidative decomposition at the positive electrode while remaining inert to the electrolyte.

(iii) It should exhibit inertness with respect to all other components within the cell, including the separator, current collectors, and packaging materials.

(iv) While being stable at elevated temperatures when combined with the electrolyte, it should also be non-toxic and cost-effective.

Among the available lithium salts for Li-ion batteries, $LiBF_4$, $LiPF_6$, $LiAsF_6$, and $LiClO_4$ are the most employed. However, their ionic conductivity (σ) in the propylene carbonate (PC) solvent is lower when compared to ethylene carbonate/dimethyl carbonate (EC/DMC) mixtures (Table 1.1). Although $LiAsF_6$ exhibits higher conductivity than $LiPF_6$ in EC/DMC, it is not a preferred option due to its toxicity. Another high-conductivity alternative in EC/DMC is $LiClO_4$, which offers high anodic stability, reaching up to 5.1 V vs. Li/Li^+. However, it reacts with organic components from the solvent at elevated temperatures and high current densities, leading to safety concerns [45, 46]. While $LiBF_4$ is less toxic than $LiAsF_6$ and offers better safety characteristics than $LiClO_4$, it has the drawback of lower ionic conductivity in EC/DMC. $LiPF_6$ is known for its chemical and thermal instability, but it has been commercialized with the use of stabilizer additives [47]. Even at room temperature, $LiPF_6$ generates solid LiF and PF_5 gas, which react with organic solvents, compromising the stability of solid-electrolyte interphase (SEI) components, such as Li_2O, LiF, Li_2CO_3, polyolefins, and semi carbonates, on the graphite anode surface [48]. Various stabilizer additives have been employed, including small amounts of LiF, tris(2,2,2-trifluoroethyl)phosphite (TTFP), fluorinated carbamates, and hexamethyl-phosphoramide [49]. Thus, $LiPF_6$ can be preferred electrolyte among other lithium salt for Li ion battery.

Table 1.1 Lithium salts as electrolyte solutes [44].

Salt	**T_m (°C)**	**$T_{decomposition}$ (°C) in solution**	**σ (mS/cm) (1 M, 25 °C)**	
			in PC	in EC/DMC
$LiPF_6$	200	80 (EC/DMC)	5.8	10.7
$LiBF_4$	29F	>100	3.4	4.9
$LiClO_4$	263	>100	5.6	8.4
$LiAsF_6$	340	>100	5.7	11.1

3. Separator: The separator is a thin, porous membrane that physically separates the anode from the cathode inside the battery cell. Its primary role is to prevent direct contact between the two electrodes, which could cause a short circuit. The separator allows the passage of lithium ions while blocking the flow of electrons [35, 50].

4. Cathode: The positive electrode, or cathode, is made of a different material that can also intercalate lithium ions during discharge. During the discharge process, lithium ions migrate from the cathode to the anode through the electrolyte. The field of intercalation chemistry materials has been studied for almost 180 years. Various types of layered materials, including few-layer metal disulfides (MS_2), have been explored for the intercalation of cations such as Li^+, Na^+, and H^+. The initial development of rechargeable Li-ion batteries featured TiS_2 as the cathode material, in a setup demonstrated by Whittingham at Exxon Corporation, utilizing a lithium metal anode and $LiClO_4$ salt dissolved in an organic solvent. This battery exhibited a discharge cell voltage below 2.5 V and demonstrated good reversibility with one lithium insertion per mole of TiS_2. Nevertheless, this battery faced two significant challenges: the low cell voltage resulting in limited energy density, and the vulnerability of the lithium anode to performance degradation due to dendrite formation during charging. Hence, some research focused on alternative intercalation chemistry to replace TiS_2 [51, 52].

5. Solid electrolyte interphase: During the operation of Li-ion batteries, a solid-electrolyte interphase (SEI) layer is formed on the surfaces of the electrodes. This effect is more pronounced at the anode, where lithium ions undergo reduction. The liquid electrolyte's components are reduced at the anode's surface during charging, resulting in the formation of deposits containing lithium salts. These reduced products combine to create a passivating layer known as the interphase. This interphase is between the electrolyte and the electrode surfaces. It allows the diffusion of lithium ions while insulating electrons, simultaneously safeguarding the electrodes from further oxidative damage caused by the electrolyte. This protective layer contributes to extending the battery's lifespan during subsequent charge-discharge cycles [53].

This is especially crucial when considering graphite-based anodes, as their reduction potential lies below the stability threshold of the electrolyte. The SEI layer is composed of two parts: an inner SEI layer in direct contact with the electrode surface, which is typically very thin and compact, primarily consisting of inorganic lithium salts; and an outer SEI layer in direct contact with the electrolyte, which is considerably thicker and mostly comprises organic lithium salts [54]. The formation of these SEI layers leads to the irreversible consumption of lithium ions and a reduction in capacity compared to the initial charge cycle [55]. This effect accumulates over the battery's lifespan, resulting in a gradual loss of capacity [56].

Additionally, the thermal decomposition of the SEI, particularly at a graphitic anode, can occur at temperatures exceeding 120 °C and significantly contribute to the initiation of thermal runaway [57]. To address this issue, certain electrolyte additives are designed to enhance the thermal stability of the lithiated graphite anode and the SEI layer [58].

At the cathode component, there is a potential for the electrolyte to undergo oxidation and create a solid-electrolyte interphase (SEI) on the cathode surfaces. This occurrence is particularly notable in high-voltage Li-ion batteries where charging beyond approximately 4.5 V surpasses the stability limits of traditional non-aqueous liquid electrolytes [59]. To effectively analyze the species involved during battery cycling, it is essential to take into account the surface chemistry of the insertion electrodes compared to the overall processes within the battery.

Safety concerns are evident with all Li-ion batteries, especially those featuring lithium metal oxide cathodes. These concerns arise due to the possibility of gas emission during operation at elevated temperatures, overcharging, or over-discharging. There is also a risk of internal short circuits. For instance, metal oxide cathodes can release oxygen gas during overcharging, the SEI layer may thermally decompose, releasing gases, and the liquid electrolyte can produce gas at the anode during reduction processes [60]. These exothermic reactions can lead to a phenomenon known as thermal runaway, wherein heat and gases accumulate inside the cells. This accumulation can eventually result in cell rupture and explosion, involving the consumption of the flammable liquid electrolyte. Many safety mechanisms are implemented to prevent such

failures, but they are not always foolproof, making them an impractical option for electric vehicles and larger batteries [61].

1.2.2 Measurement technique characteristics

Understanding how a battery works and how to analyze the performance of electrochemical sources is associated with the thermodynamics of electrochemical processes. In a galvanic cell, electrical energy is generated through an electrochemical reaction. This redox reaction involves the transfer of electrons between different species at the interface between the electrodes and electrolyte. The redox reaction is divided into two half-cell reactions: the oxidation reaction (as described in Equation 9), where electrons are released at the anode, and the reduction reaction, where electrons are received by the cathode (as depicted in Equation 10). In these equations, n represents the number of electrons involved in the process [44].

$$aA \rightarrow cC + ne^{-} \tag{9}$$

$$bB + ne^{-} \rightarrow dD \tag{10}$$

The overall reaction is defined as follows:

$$aA + bB \rightarrow cC + dD \tag{11}$$

In the state of equilibrium, you can determine the specific standard electrode potential by using the thermodynamic information of the reaction (Equation 12).

$$E^{0} = \frac{-\Delta G^{0}}{nF} \qquad [V] \tag{12}$$

Here, ΔG^{0} represents the standard Gibbs free energy, n stands for the number of electrons involved, and F denotes the Faraday constant, which signifies the charge quantity per mole of electrons, as outlined in Equation 13 [44].

$$F = e\,N_A \qquad \frac{96485.3C}{mol}\ or\ \frac{26.802Ah}{mol} \tag{13}$$

Under non-standard conditions, you can determine the potential of the full cell reaction using the Nernst Equation (Equation 14). In this equation, E_{cell} represents the cell potential at the given temperature, E^0_{cell} stands for the standard cell potential under equilibrium conditions, R denotes the universal gas constant, T is the absolute temperature, and Q_r represents the reaction quotient [42].

$$E_{cell} = E^0_{cell} - \frac{RT}{nF} \ln Q_r \quad [V] \tag{14}$$

1.2.3 Electrochemical measurement definitions

Different electrochemical measurement are defined below [44, 62]:

1. Open circuit voltage (OCV): This refers to the voltage of a cell when it is not actively discharging or charging, essentially the voltage state of a cell when it is not connected to an external circuit and electrode potentials are at equilibrium.
2. Theoretical capacity: It is denoted as the overall amount of electricity involved in the electrochemical process and is described in coulombs or ampere-hours. The ampere-hour capacity of a battery is linked to the amount of electricity derived from the active materials.
3. Theoretical energy: The cell's capacity can also be viewed from an energy perspective, taking into account both voltage and the amount of electricity involved. This theoretical energy measure represents the maximum energy output achievable by a particular electrochemical system, which can be calculated as:

   Watthour (Wh) = voltage (V) × ampere-hour (Ah) (15)

4. Current rate (C-rate): This indicates the time required for either a complete charge or discharge, where C represents the theoretical or nominal charge capacity, as defined in Equation 16. For instance, 1 C is the complete transfer of all stored energy within one hour, meaning the entire battery will be discharged in 1 hour. Another example, C/10

(0.1 C), indicates that the full transfer of all stored energy takes place over a period of 10 hours.

$$\mathrm{C} = \frac{discharge\ current}{nominal\ capacity} \tag{16}$$

5. Cycle: A single sequence involving a complete process of discharging and then charging. It's crucial for battery evaluation that each parameter is linked to a fundamental understanding of the thermodynamics and kinetics specific to a given system or materials of interest. For instance, the electrode potential (Equation 12) varies depending on the electrochemical potential of a material. At the cell level, the potential difference between the anode and cathode offers insight into the energy capacity of the battery. Conversely, kinetic energy is a parameter reflecting the speed of charging and discharging, exemplified by the simple parameter of power. Another vital factor is cyclic stability, where ideally a battery should maintain a long cycle life with minimal performance deterioration.

Various electrochemical techniques can be employed to assess the electrochemical performance of a battery. Nonetheless, the primary techniques for evaluating battery performance consist of cyclic voltammetry (CV) and Galvanostatic charging/discharging tests [63, 64].

1. Cyclic Voltammetry (CV): Cyclic voltammetry is a method based on the fundamental concept of linear sweep voltammetry, which involves measuring current as the potential varies linearly over time. CV enables the assessment of electrochemical variables that influence reaction voltage and reversibility. Additionally, it facilitates quantitative analysis of factors like Li^+ diffusivity, intercalation, capacitive reactions, and anionic redox reactions.
2. Galvanostatic charging/discharging (GCD): Galvanostatic Charge/Discharge (GCD) tests, sometimes referred to as Constant Current Charging/Discharging, are commonly employed for evaluating energy storage systems and materials. GCD entails applying a consistent flow of positive and negative currents to charge and discharge a material or

system while maintaining a specific potential limit. This procedure is often repeated over multiple cycles.

Conclusion

In this chapter, the comprehensive overview of chemical gas sensors, primarily focusing on semiconductor-based sensors, was presented. It defined chemical sensors, emphasizing the roles of the receptor, transducer, and packaging module in detecting specific chemical compound. The chapter focused on a detailed discussion of semiconductor sensor performance characteristics. Semiconductor metal oxide sensors were favorably compared to other sensing technologies, underlining their attributes such as sensitivity, stability, selectivity, response time, accuracy, durability, low maintenance requirements, cost-effectiveness, and miniaturization potential. The mechanisms of gas sensing, involving chemisorption and physisorption were explored with a focus on the crucial role of oxygen adsorption on semiconductor surfaces. The chapter also considered various parameters like temperature, humidity, additives, and composite materials and how they influence gas sensing performance, emphasizing the importance of controlling and optimizing these parameters for tailoring sensors to specific applications.

Additionally, the chapter provided a comprehensive historical perspective on Li-ion batteries. It underlined the complex nature of Li-ion batteries, emphasizing the roles of key components, such as the anode, cathode, electrolyte, separator, and solid electrolyte interphase layer, in facilitating the movement of lithium ions and electrons for energy storage. The choice of materials for these components was discussed considering factors like conductivity, stability, and safety. The chapter also introduced various measurement techniques and key parameters for battery evaluation, emphasizing the importance of understanding the thermodynamics and kinetics of electrochemical processes.

References

[1] W.H. Brattain, J. Bardeen, Surface properties of germanium, The Bell System Technical Journal, 32 (1953) 1-41.
[2] T. Seiyama, A. Kato, K. Fujiishi, M. Nagatani, A new detector for gaseous components using semiconductive thin films, Analytical Chemistry, 34 (1962) 1502-1503.
[3] D. Briand, J. Courbat, Chapter Thirteen - Micromachined semiconductor gas sensors, in: R. Jaaniso, O.K. Tan (Eds.) Semiconductor Gas Sensors (Second Edition), Woodhead Publishing2020, pp. 413-464.
[4] A. Hulanicki, S. Glab, F. Ingman, Chemical sensors: definitions and classification, Pure and applied chemistry, 63 (1991) 1247-1250.
[5] D.T. McQuade, A.E. Pullen, T.M. Swager, Conjugated polymer-based chemical sensors, Chemical reviews, 100 (2000) 2537-2574.
[6] A. Oprea, U. Weimar, Gas sensors based on mass-sensitive transducers part 1: transducers and receptors—basic understanding, Analytical and bioanalytical chemistry, 411 (2019) 1761-1787.
[7] G. Korotcenkov, Metal oxides for solid-state gas sensors: What determines our choice?, Materials Science and Engineering: B, 139 (2007) 1-23.
[8] N. Kaur, M. Singh, E. Comini, One-dimensional nanostructured oxide chemoresistive sensors, Langmuir, 36 (2020) 6326-6344.
[9] M. Arafat, B. Dinan, S.A. Akbar, A. Haseeb, Gas sensors based on one dimensional nanostructured metal-oxides: a review, Sensors, 12 (2012) 7207-7258.
[10] G. Barandun, L. Gonzalez-Macia, H.S. Lee, C. Dincer, F. Güder, Challenges and opportunities for printed electrical gas sensors, ACS sensors, 7 (2022) 2804-2822.
[11] Y. Zhang, Y. Zhu, Z. Zeng, G. Zeng, R. Xiao, Y. Wang, Y. Hu, L. Tang, C. Feng, Sensors for the environmental pollutant detection: Are we already there?, Coordination Chemistry Reviews, 431 (2021) 213681.
[12] B. Yang, N.V. Myung, T.T. Tran, 1D metal oxide semiconductor materials for chemiresistive gas sensors: a review, Advanced Electronic Materials, 7 (2021) 2100271.
[13] N. Nakano, S. Ogawa, Preparation of thin gold-film electrode for an electrochemical gas sensor for phosphine and arsine, Sensors and Actuators B: Chemical, 21 (1994) 51-55.
[14] S.P. Lee, Electrodes for semiconductor gas sensors, Sensors, 17 (2017) 683.
[15] I.-S. Hwang, E.-B. Lee, S.-J. Kim, J.-K. Choi, J.-H. Cha, H.-J. Lee, B.-K. Ju, J.-H. Lee, Gas sensing properties of SnO_2 nanowires on micro-heater, Sensors and Actuators B: Chemical, 154 (2011) 295-300.
[16] M.-T. Ke, M.-T. Lee, C.-Y. Lee, L.-M. Fu, A MEMS-based benzene gas sensor with a self-heating WO_3 sensing layer, Sensors, 9 (2009) 2895-2906.
[17] V. Lavrenko, I. Podchernyaeva, D. Shchur, A.D. Zolotarenko, A.D. Zolotarenko, Features of physical and chemical adsorption during interaction of polycrystalline and nanocrystalline materials with gases, Powder Metallurgy and Metal Ceramics, 56 (2018) 504-511.
[18] W. Ding, D. Liu, J. Liu, J. Zhang, Oxygen defects in nanostructured metal-oxide gas sensors: recent advances and challenges, Chinese Journal of Chemistry, 38 (2020) 1832-1846.

[19] Y. Yamaguchi, K. Tabata, E. Suzuki, Density functional theory calculations for the interaction of oxygen with reduced M/SnO_2 (110)(M= Pd, Pt) surfaces, Surface Science, 526 (2003) 149-158.
[20] C.-O. Park, S. Akbar, Ceramics for chemical sensing, Journal of materials science, 38 (2003) 4611-4637.
[21] N. Barsan, U. Weimar, Conduction model of metal oxide gas sensors, Journal of electroceramics, 7 (2001) 143-167.
[22] H.-J. Kim, J.-H. Lee, Highly sensitive and selective gas sensors using p-type oxide semiconductors: Overview, Sensors and Actuators B: Chemical, 192 (2014) 607-627.
[23] C.-K. Lu, H.-F. Meng, Hole doping by molecular oxygen in organic semiconductors: Band-structure calculations, Physical Review B, 75 (2007) 235206.
[24] M.A. Fox, M.T. Dulay, Heterogeneous photocatalysis, Chemical reviews, 93 (1993) 341-357.
[25] M.H. Kang, J. Armitage, Z. Andaji-Garmaroudi, H. Sirringhaus, Surface Passivation Treatment to Improve Performance and Stability of Solution-Processed Metal Oxide Transistors for Hybrid Complementary Circuits on Polymer Substrates, Advanced Science, 8 (2021) 2101502.
[26] M. Gardon, J.M. Guilemany, A review on fabrication, sensing mechanisms and performance of metal oxide gas sensors, Journal of Materials Science: Materials in Electronics, 24 (2013) 1410-1421.
[27] R. Vander Wal, G. Hunter, J. Xu, M. Kulis, G. Berger, T. Ticich, Metal-oxide nanostructure and gas-sensing performance, Sensors and Actuators B: Chemical, 138 (2009) 113-119.
[28] C. Wang, L. Yin, L. Zhang, D. Xiang, R. Gao, Metal oxide gas sensors: sensitivity and influencing factors, sensors, 10 (2010) 2088-2106.
[29] V.S. Bhati, M. Kumar, R. Banerjee, Gas sensing performance of 2D nanomaterials/metal oxide nanocomposites: A review, Journal of Materials Chemistry C, 9 (2021) 8776-8808.
[30] J. Boyle, K. Jones, The effects of CO, water vapor and surface temperature on the conductivity of a SnO_2 gas sensor, Journal of Electronic Materials, 6 (1977) 717-733.
[31] T. Sahm, A. Gurlo, N. Barsan, U. Weimar, L. Mädler, Fundamental studies on SnO_2 by means of simultaneous work function change and conduction measurements, Thin Solid Films, 490 (2005) 43-47.
[32] Q. Li, W. Zeng, Y. Li, Metal oxide gas sensors for detecting NO_2 in industrial exhaust gas: Recent developments, Sensors and Actuators B: Chemical, 359 (2022) 131579.
[33] N. Hou, Q. Sun, J. Yang, S. You, Y. Cheng, Q. Xu, W. Li, S. Xing, L. Zhang, J. Zhu, Fabrication of oxygen-doped $MoSe_2$ hierarchical nanosheets for highly sensitive and selective detection of trace trimethylamine at room temperature in air, Nano Research, 13 (2020) 1704-1712.
[34] D.R. Miller, S.A. Akbar, P.A. Morris, Nanoscale metal oxide-based heterojunctions for gas sensing: A review, Sensors and Actuators B: Chemical, 204 (2014) 250-272.
[35] R. Korthauer, Lithium-ion batteries: basics and applications, Springer2018.
[36] J. Xie, Y.-C. Lu, A retrospective on lithium-ion batteries, Nature communications, 11 (2020) 2499.
[37] M.S. Whittingham, Electrical energy storage and intercalation chemistry, Science, 192 (1976) 1126-1127.
[38] T. Horiba, Lithium-ion battery systems, Proceedings of the IEEE, 102 (2014) 939-950.
[39] R. Moshtev, B. Johnson, State of the art of commercial Li ion batteries, Journal of power sources, 91 (2000) 86-91.
[40] J.-M. Tarascon, M. Armand, Issues and challenges facing rechargeable lithium batteries, nature, 414 (2001) 359-367.
[41] Y. Yue, H. Liang, Micro- and Nano-Structured Vanadium Pentoxide (V_2O_5) for Electrodes of Lithium-Ion Batteries, Advanced Energy Materials, 7 (2017) 1602545.
[42] Y. Tang, X. Rui, Y. Zhang, T.M. Lim, Z. Dong, H.H. Hng, X. Chen, Q. Yan, Z. Chen, Vanadium pentoxide cathode materials for high-performance lithium-ion batteries enabled by a hierarchical nanoflower structure via an electrochemical process, Journal of Materials Chemistry A, 1 (2013) 82-88.

[43] J. Zheng, Y. Zhang, T. Hu, T. Lv, C. Meng, New strategy for the morphology-controlled synthesis of V_2O_5 microcrystals with enhanced capacitance as battery-type supercapacitor electrodes, Crystal Growth & Design, 18 (2018) 5365-5376.
[44] D. Linden, T. Reddy, Handbook of batteries, McGraw-Hill Companies Inc, USA, 2002.
[45] J. Tarascon, D. Guyomard, New electrolyte compositions stable over the 0 to 5 V voltage range and compatible with the $Li_{1+x}Mn_2O_4$/carbon Li-ion cells, Solid State Ionics, 69 (1994) 293-305.
[46] G. Newman, R. Francis, L. Gaines, B. Rao, Hazard investigations of $LiClO_4$/dioxolane electrolyte, Journal of The Electrochemical Society, 127 (1980) 2025.
[47] H. Yang, G.V. Zhuang, P.N. Ross Jr, Thermal stability of $LiPF_6$ salt and Li-ion battery electrolytes containing $LiPF_6$, Journal of Power Sources, 161 (2006) 573-579.
[48] S.K. Heiskanen, J. Kim, B.L. Lucht, Generation and evolution of the solid electrolyte interphase of lithium-ion batteries, Joule, 3 (2019) 2322-2333.
[49] S.S. Zhang, A review on electrolyte additives for lithium-ion batteries, Journal of Power Sources, 162 (2006) 1379-1394.
[50] X. Huang, Separator technologies for lithium-ion batteries, Journal of Solid State Electrochemistry, 15 (2011) 649-662.
[51] A. Manthiram, A reflection on lithium-ion battery cathode chemistry, Nature communications, 11 (2020) 1550.
[52] M.S. Whittingham, Chemistry of intercalation compounds: Metal guests in chalcogenide hosts, Progress in Solid State Chemistry, 12 (1978) 41-99.
[53] E. Peled, The electrochemical behavior of alkali and alkaline earth metals in nonaqueous battery systems—the solid electrolyte interphase model, Journal of The Electrochemical Society, 126 (1979) 2047.
[54] P. Verma, P. Maire, P. Novák, A review of the features and analyses of the solid electrolyte interphase in Li-ion batteries, Electrochimica Acta, 55 (2010) 6332-6341.
[55] S. Zhang, M.S. Ding, K. Xu, J. Allen, T.R. Jow, Understanding solid electrolyte interface film formation on graphite electrodes, Electrochemical and Solid-State Letters, 4 (2001) A206.
[56] T. Yoshida, M. Takahashi, S. Morikawa, C. Ihara, H. Katsukawa, T. Shiratsuchi, J.-i. Yamaki, Degradation mechanism and life prediction of lithium-ion batteries, Journal of The Electrochemical Society, 153 (2006) A576.
[57] M.F. Sgroi, Lithium-Ion Batteries Aging Mechanisms, MDPI, 2022, pp. 205.
[58] W. Qu, E. Dorjpalam, R. Rajagopalan, C.A. Randall, Role of Additives in Formation of Solid–Electrolyte Interfaces on Carbon Electrodes and their Effect on High-Voltage Stability, ChemSusChem, 7 (2014) 1162-1169.
[59] N.-S. Choi, J.-G. Han, S.-Y. Ha, I. Park, C.-K. Back, Recent advances in the electrolytes for interfacial stability of high-voltage cathodes in lithium-ion batteries, Rsc Advances, 5 (2015) 2732-2748.
[60] A.W. Golubkov, D. Fuchs, J. Wagner, H. Wiltsche, C. Stangl, G. Fauler, G. Voitic, A. Thaler, V. Hacker, Thermal-runaway experiments on consumer Li-ion batteries with metal-oxide and olivin-type cathodes, Rsc Advances, 4 (2014) 3633-3642.
[61] P. Balakrishnan, R. Ramesh, T.P. Kumar, Safety mechanisms in lithium-ion batteries, Journal of power sources, 155 (2006) 401-414.
[62] C.R. Birkl, E. McTurk, M. Roberts, P.G. Bruce, D.A. Howey, A parametric open circuit voltage model for lithium ion batteries, Journal of The Electrochemical Society, 162 (2015) A2271.
[63] F. Licht, M. Davis, H. Andreas, Charge redistribution and electrode history impact galvanostatic charging/discharging and associated figures of merit, Journal of Power Sources, 446 (2020) 227354.
[64] T. Kim, W. Choi, H.-C. Shin, J.-Y. Choi, J.M. Kim, M.-S. Park, W.-S. Yoon, Applications of voltammetry in lithium ion battery research, Journal of Electrochemical Science and Technology, 11 (2020) 14-25.

Chapter 2: Nanomaterial: Metal oxide structures, their properties and applications

Introduction

This chapter overviews nanomaterials and their applications, particularly in gas sensors and energy storage. It begins with the synthesis method of nanomaterials, discussing the bottom-up and top-down approaches, and the impact of nanoscale dimensions on material properties. Nanomaterials, classified based on their dimensionality, exhibit unique behaviors and are strategically utilized for their unique properties in gas sensors and energy storage applications. The chapter extensively covers the synthesis methods of specific nanomaterials such as tungsten trioxide, zinc oxide, copper oxide, and vanadium pentoxide, exploring their properties such as crystalline structures and their application in gas sensing, battery technology, and various emerging fields.

2.1 Nanomaterial

The growth of nanomaterials encompasses a wide range of techniques that enable the controlled synthesis and fabrication of materials at the nanoscale. These techniques include bottom-up approaches such as chemical vapor deposition, sol-gel methods, and hydrothermal synthesis, as well as top-down methods like lithography, ball milling, and exfoliation [1]. Additionally, hybrid approaches combining multiple techniques have gained attention. These growth methods allow for precise control over their size, shape, and composition, leading to the formation of various classes of nanomaterials [2]. Nanomaterials can be classified based on their dimensionality, which refers to the number of dimensions at the nanoscale (Figure 2.1). Zero-dimensional (0D) nanomaterials, such as nanoparticles and quantum dots, have all dimensions in the nanoscale range. It is widely acknowledged that the nanoparticle grain size strongly influences the conductance of semiconductor sensing materials. The relationship between grain size (D) and the thickness of the space charge layer (L) is crucial. In this context, different scenarios are identified: boundary control for $D >> 2L$, neck control for $D \geq 2L$, and grain control for $D < 2L$ [3]. Additionally, factors such as crystallinity, crystal structure, specific

area, and chemical composition can significantly impact the gas sensing performance of 0D metal oxide semiconductors (MOSs) nanoparticles [1]. One-dimensional (1D) nanomaterials, including nanowires and nanorods, possess one dimension in the nanoscale range. 1D MOSs are extensively investigated as sensing materials, owing to their large surface-to-volume ratio, high porosity and electronic characteristics [4]. Two-dimensional (2D) nanomaterials, like MOSs, graphene, metal dichalcogenides and g-C_3N_4, have two dimensions in the nanoscale range. In recent years, 2D materials have emerged as advanced nanomaterials with outstanding chemical, physical, and electrical properties. Studies have provided a comprehensive overview of the physical characteristics of various 2D materials, such as bandgap, work function, electroconductivity, and thermal conductivity. The unique nanoscale thickness and atomically thin layered structure offer greater flexibility in the design of 2D materials compared to traditional bulk materials [5]. Furthermore, the 2D structure is particularly well-suited for crystal facet engineering, providing a substantial advantage in exposing a large surface area of active facets for MOSs [6]. In contrast, three-dimensional (3D) nanomaterials, such as nanostructured thin films and mesoporous structures, possess all three dimensions in the nanoscale range. In comparison to nanomaterials of other dimensions, 3D MOSs exhibit a broader range of morphologies and controlled pore structures. Over the past decade, various hierarchical sensing materials with unique architectures have been extensively studied. These materials are constructed from building subunits of low-dimensional 0D, 1D, and 2D structures, resembling natural morphological formations like tree branches, sea urchins, and flowers. The resulting hierarchical nanostructures possess exceptionally high specific surface areas and excellent gas permeability, offering opportunities to enhance sensing behavior through adjustments in shape and dimension [1, 7, 8].

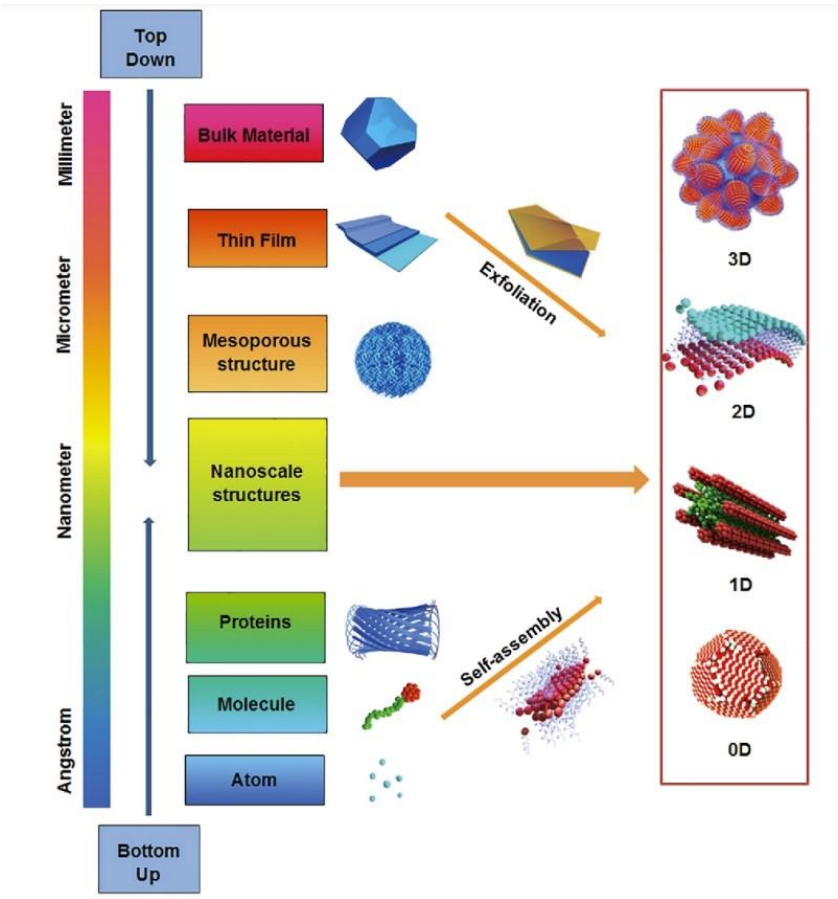

Figure 2.1 Top-down and bottom-up techniques to prepare 0D, 1D, 2D, 3D nanomaterials [1].

Some research on the preparation of metal oxide nanostructures for gas sensor and energy storage applications focuses on the unique properties and advantages offered by nanoscale materials compared to their bulk counterparts. Nano-size matters in gas sensing due to several factors. First, the increased surface-to-volume ratio in nanomaterials provides a larger active surface area for gas interaction, leading to enhanced sensitivity [9]. Second, the quantum size effects observed at the nanoscale can significantly influence the electronic and optical properties of the materials, resulting in improved gas sensing performance [10]. Lastly, the nanostructured morphology allows for tailored design and manipulation of the material's properties, enabling better control over gas sensing selectivity, response time, and recovery time [11]. Therefore, by utilizing metal oxide nanostructures, researchers aim to develop gas sensors with superior performance, higher sensitivity, selectivity, and faster response times,

contributing to advancements in environmental monitoring, industrial safety, medical diagnosis, and other fields requiring precise gas detection and analysis.

Furthermore, when applied to battery technology, nanomaterials offer a range of advantages aimed at significantly enhancing energy storage and battery performance. By reducing electrode particle size to the nanoscale, electrochemical performances are enhanced due to a shorter diffusion pathway for lithium ions within the electrode and higher electrode-electrolyte contact due to the larger surface area of nanoparticles [12]. Reducing electrode particle size to nanometer range results in decreasing mechanical stresses caused by volumetric expansion and contraction during charge-discharge cycles [13]. Nanomaterials, whether in the form of nanopowders or structured films exhibiting various shapes like wires, rods, or columns, are actively under exploration to extend the lifespan of batteries and increase electrochemical performances [14]. Furthermore, these materials could facilitate the development of ultrathin and flexible battery geometries, enabling the fabrication of high-rate, low-profile battery formats for diverse applications in electronics and medical devices, offering a promising path for the future of energy storage and portable technology [15].

2.1.1 Synthesis of Nanomaterials: Top-down and Bottom-up Approaches

Nanomaterials can be synthesized using two main approaches: top-down and bottom-up. These approaches offer distinct methods for fabricating nanoscale structures with precise control over their size, shape, and composition. Understanding these synthesis methods is crucial for tailoring nanomaterials with desired properties for various applications.

2.1.1.1 Top-down Approach

The top-down approach involves starting with a bulk material and reducing its size to the nanoscale through various fabrication techniques. This method relies on mechanical or chemical processes to break down the larger material into smaller structures. Some common top-down

techniques include lithography, grinding, milling, and etching [1]. Lithography uses patterning and masking techniques to selectively deposit material on a substrate, allowing precise control over the nanoscale features [16]. While top-down approaches are useful for synthesizing nanoscale structures with predefined shapes and patterns, limitations such as potential damage to the material and difficulties in achieving uniformity at the nanoscale exist [17, 18].

2.1.1.2 Bottom-up Approach

The bottom-up approach begins building nanoscale structures from smaller components, such as atoms, molecules, or nanoparticles, through self-assembly or chemical reactions. This method is based on the principles of molecular self-organization, where components arrange themselves into larger structures with specific properties. Bottom-up techniques include chemical vapor deposition, sol-gel methods, hydrothermal synthesis, and molecular beam epitaxy [17, 18]. In chemical vapor deposition, the desired material is deposited layer by layer onto a substrate by introducing precursor gases into a reaction chamber [19].

Both top-down and bottom-up approaches have their advantages and limitations. Top-down approaches are advantageous for creating well-defined nanoscale patterns and structures, but may not be suitable for all materials, potentially resulting in damage or defects. On the other hand, bottom-up approaches offer better control over the properties and composition of nanomaterials but may be more challenging to scale up for large-scale production (Figure 2.2) [20].

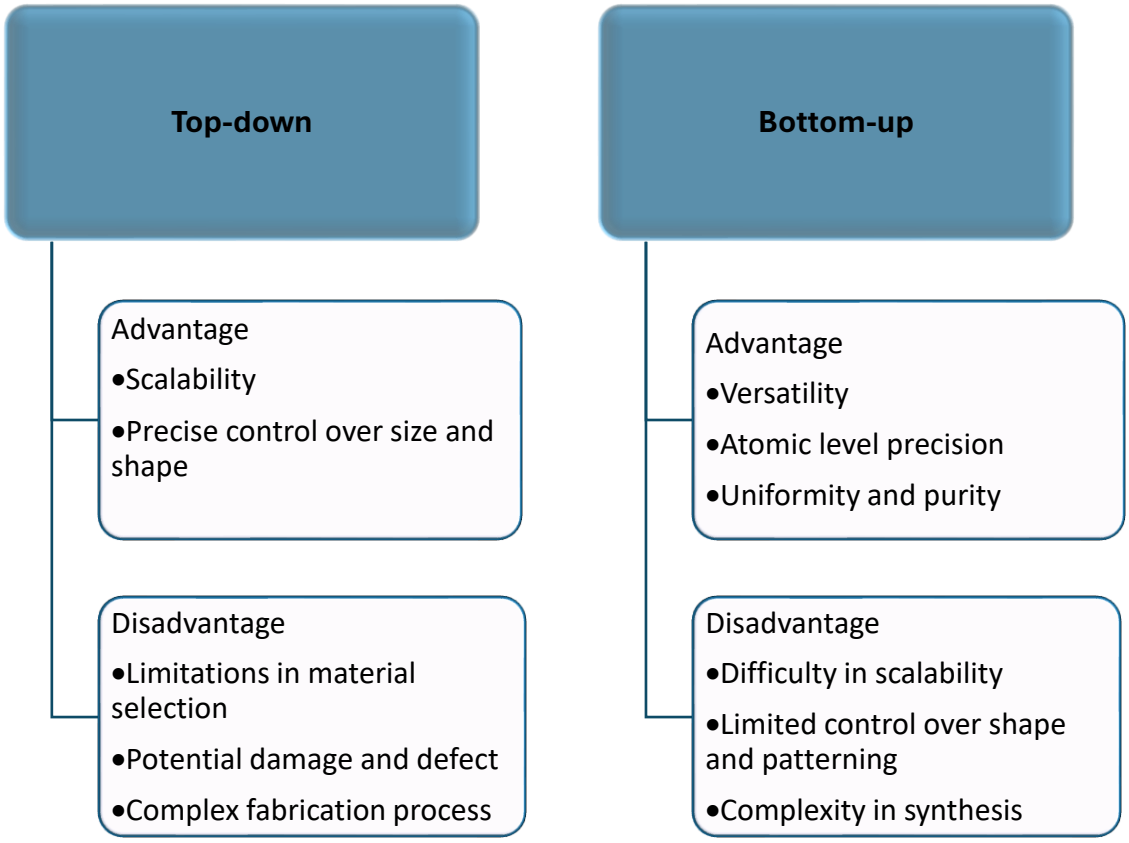

Figure 2.2 Top-down and bottom-up techniques advantages and disadvantages.

2.2 Materials properties and their applications in this thesis

2.2.1 Tungsten trioxide (WO_3)

WO_3 can exhibit different crystalline structures depending on various factors, including synthesis methods, temperature, and pressure conditions. The crystal structures of stoichiometric WO_3 can be described as distorted ABO_3 perovskites, where ion A's position remains unoccupied and ion B is replaced by W. The WO_3 crystal structure consists of a network of WO_6 octahedra that share corners in three dimensions [21]. Within a unit cell, each W atom is surrounded by six octahedrally coordinated O atoms, with four lying in a plane containing the W atoms and the other two positioned above and below the W atom [22, 23]. This symmetry differs from the ideal cubic ReO_3 structure due to the tilting of oxygen octahedra and the off-center shifting of W atoms in the WO_6 octahedral environment (Figure 2.3). As a result, the bond angles between W-

O-W alternate between 165° and 179°, leading to various phases of WO_3, such as monoclinic II (ε-WO_3), triclinic (δ-WO_3), monoclinic I (γ-WO_3), orthorhombic (β-WO_3), tetragonal (α-WO_3), and cubic WO_3 (c-WO_3) [23, 24]. Yang et al. conducted first principle calculations to investigate the structural and electronic properties of different crystal structures of WO_3. Table 2.1 provides information on the space groups, band gaps and thermal stability of these crystal structures. The increase in band gaps from cubic to tetragonal structures is attributed to the reduction in valence band width caused by the expansion of the octahedral volume. The significantly enlarged band gaps of β-, γ-, and δ-WO_3 result from the upward shift of the 5dxy states at the bottom of the conduction band. Furthermore, WO_3 undergoes temperature-dependent following phase transitions (ε-WO_3, <−43 °C →*δ*-WO_3, −43 °C to 17 °C → *γ*-WO_3, 17 °C to 330 °C →β -WO_3, 330 °C to 740 °C → *α*-WO_3, >740 °C) [25]. γ-WO_3 is the most stable phase under ambient conditions and often coexisting with the δ-WO_3 phase [26]. The hexagonal WO_3 phase (hex-WO_3), first reported in 1979, is another common phase, characterized by corner-sharing WO_6 octahedra arranged in a manner that forms three- and six-membered rings in the ab-planes. These structures stack in the c-axis, creating trigonal and hexagonal tunnels due to the presence of the three- and six-membered rings. Notably, hex-WO_3 is a metastable phase and is usually challenging to obtain through crystal-phase transition, tending to transform into the monoclinic phase when annealed at temperatures exceeding 400 °C [22, 27, 28]. It is important to note that the crystalline structure of WO_3 can significantly influence its physical, chemical, and electrical properties, including its bandgap, conductivity and surface reactivity. Researchers often explore different synthesis methods and conditions to control and engineer the crystalline structure of WO_3, aiming to enhance specific properties for various applications [23].

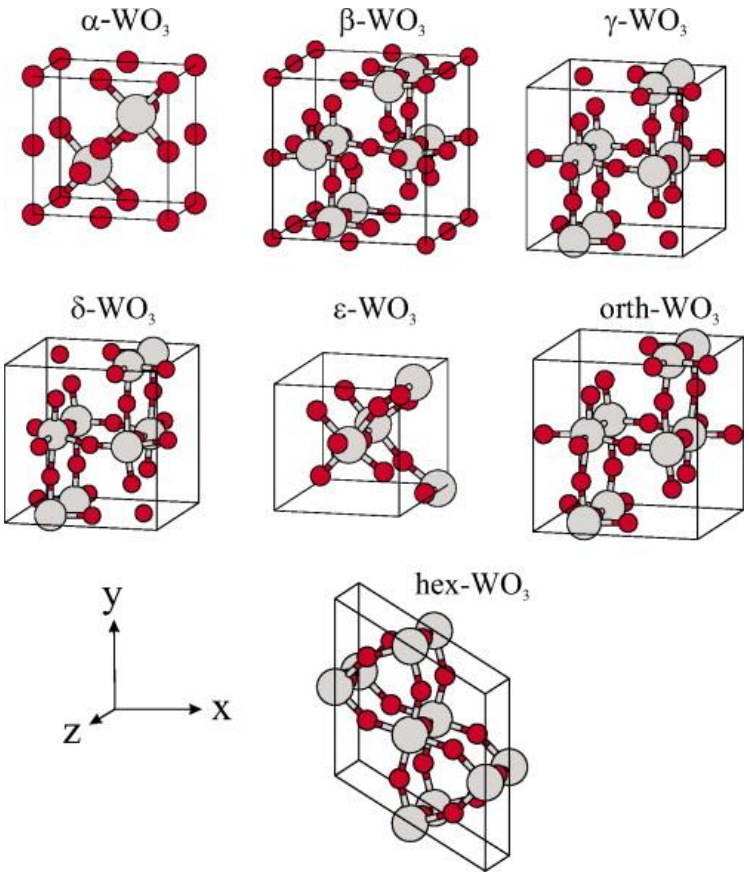

Figure 2.3 Unit cells of different phases of WO_3 [21].

Table 2.1 Different crystal structure, space groups and thermal stability of WO_3 .

Crystal structure	Space group	Band gap	Thermal stability
Triclinic	P1	2.813	-43 to 17 °C
Monoclinic	P21/C	2.881	17 to 330 °C
Orthorhombic	Pmnb	2.974	330 to 740 °C
Tetragonal	P4/ncc	2.244	>740 °C
Hexagonal	P6/mmm	1.943	Metastable
Cubic	Pm3̄m	1.562	Metastable

WO_3 is a well-known n-type semiconductor that possesses a wide and stable tunable bandgap, making it highly suitable for various applications. This bandgap represents the difference

between the energy levels of the valence band (comprising filled O 2p orbitals) and the conduction band (comprising empty W 5d orbitals). As previously mentioned, the crystal phase of WO_3 transitions in a sequence determined by the degree of deviation from the ideal cubic phase. This transition fundamentally entails a change in E_g since it results in alterations in the occupied levels of the W 5d states. Amorphous WO_3, which is the most distorted structure, typically has a relatively large E_g, approximately around 3.25 eV. Conversely, bulk monoclinic WO_3 is known to exhibit a typical E_g of approximately 2.62 eV at room temperature [29, 30].

Another important property is electrical conductivity and n-type metal oxide conductivity depends on a concentration of free electrons in its conduction band. The concentration of stoichiometric defects like oxygen vacancies can determine the concentration of free electrons [31]. The electrical conductivity of single-crystal WO_3 varies between 10 and 10^{-4} S cm^{-1}, depending on factors like stoichiometry [32]. Furthermore, structural properties such as grain size, grain boundaries, film thickness, the specific phase and the presence of dopants have significant impact on the material's electrical conductivity. Hence, the electrical characteristics of WO_3 are influenced by the synthesis methods and growth conditions [33].

Tungsten oxides have gained significant interest in photocatalysis applications owing to their versatile adjustability in stoichiometry and structure, favorable band gaps, chemical stability and earth-abundance. Nevertheless, this material exhibits relatively low efficiency due to the rapid recombination of photo-generated electrons and holes. Several methods have been employed to improve the photocatalytic properties of tungsten oxides. These approaches include the control of crystal phases, stoichiometry or oxygen vacancies, active facets and morphological features, doping and the preparation of composite through the coupling with other semiconductor materials [22].

Most investigations into WO_3 electrochromic (EC) devices have focused on amorphous films. These films offer high coloration efficiency (around 55 cm^2 m C^{-1} for H^+ intercalation) and exhibit rapid coloration and bleaching [34, 35]. However, amorphous WO_3 exhibits limited structural and chemical stability, leading to poor EC stability. In contrast, crystalline WO_3 is more stable due to its denser structure and slower dissolution rate in acidic electrolytes [36].

Nevertheless, crystalline bulk WO_3 has a relatively lower charge density of 3 mC cm^{-2} mg^{-1} compared to approximately 9 mC cm^{-2} mg^{-1} in the amorphous form [35], as well as lower coloration efficiency (approximately 25 cm^2 m C^{-1} for H^+ intercalation) [37] and slower switching times. A recent solution to these issues involves the utilization of a nanostructured WO_3 film with high porosity, addressing the limitations of crystalline WO_3 in EC applications [35, 38].

Research has highlighted good gas sensing properties of WO_3. Despite significant progress in designing and fabricating WO_3 with different dimensional structures, achieving high-performance gas sensing remains a challenge. To address this, various synthesis methods have been employed to synthesize WO_3 with diverse morphologies in different dimensions (0D, 1D, 2D, and 3D) [23]. To enhance gas sensing properties, effective strategies such as exposing crystal facets, elemental doping, noble metal functionalization and forming heterojunctions have been investigated [11]. The crystalline structure of WO_3 also influences its gas sensing properties [33]. The crystal structure of WO_3 can be further modified through doping or polymorphism by using various synthesis methods to tailor its properties for specific applications such as photocatalysis and gas sensors. As discussed previously, WO_3 with different crystalline phases possesses a different band gap. A phase junction could be fabricated between different crystal phases using one step synthesis method, resulting in improving photocatalysis performance [39]. Therefore, in this thesis, a simple and one step sol-gel method is used to fabricate WO_3 phase junction to evaluate its gas sensing performance. However, the relationship between the created phase junction in WO_3 and its influence on gas sensing properties remains unclear and requires further investigation.

2.2.2 Zinc oxide (ZnO)

ZnO has a unique crystalline structure and a wide range of applications in various fields. ZnO can exist in three distinct crystalline structures, each with its own unique arrangement of Zn and O atoms. These structures significantly affect the material's properties and its suitability for

various applications. The three primary crystalline structures of ZnO are the hexagonal wurtzite structure, cubic zinc blend structure, and cubic rocksalt structure [40].

The hexagonal wurtzite structure is the most common and thermodynamically stable crystalline form of ZnO. In this structure, the Zn and O atoms are arranged in a hexagonal lattice, belonging to the space group P63mc. Each zinc ion is tetrahedrally coordinated with four oxygen ions and each oxygen ion is bonded to two zinc ions (Figure 2.4a). The noncentral symmetric structure of ZnO arises from its tetrahedral coordination, leading to the manifestation of piezoelectric and pyroelectric properties. Additionally, the wurtzite structure exhibits strong covalent bonds between the Zn and O atoms, resulting in excellent electronic and optical properties [41]. Its piezoelectric properties make it suitable for sensors and acoustic devices [42].

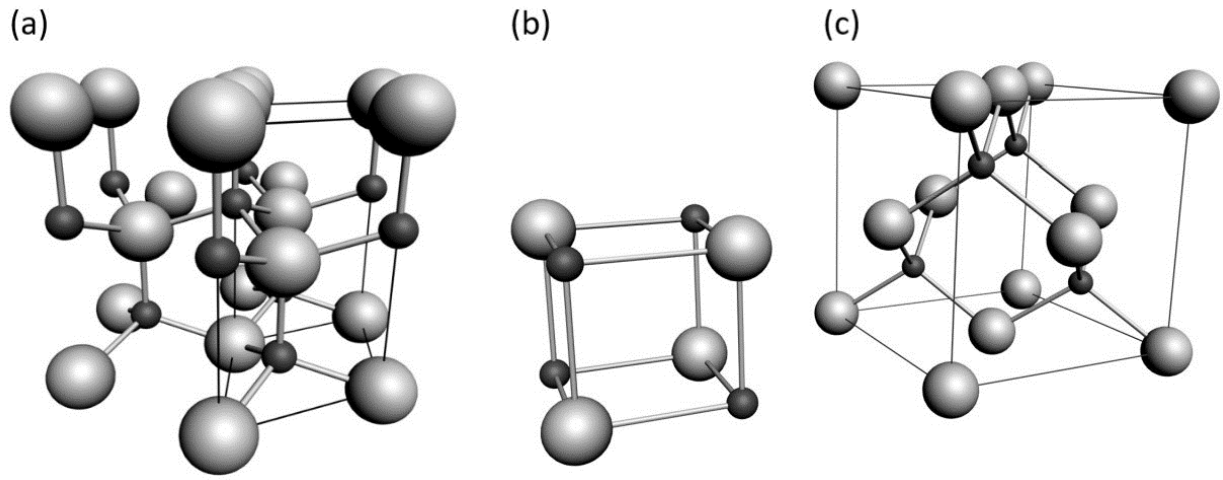

Figure 2.4 a) The hexagonal wurtzite structure of ZnO, b) The rock salt phase of ZnO and c) zincblende phases of ZnO. O atoms are shown as large grey spheres, Zn atoms as smaller black spheres. One unit cell is outlined for clarity [43].

The cubic zinc blend structure is less common than the wurtzite structure (Figure 2.4c). The cubic zinc blend structure is metastable and can be achieved through specific growth techniques [44]. The cubic rocksalt structure is another metastable crystalline form of ZnO (Figure 2.4b). The rocksalt structure is typically formed under specific high-pressure conditions

like 9.5 GPa [45]. The stability of this phase can be increased using doping metal like Mg [46]. The cubic rocksalt ZnO can find applications in high-pressure physics and certain areas of materials research where extreme conditions are involved. The Grüneisen parameter and heat capacity of hexagonal wurtzite ZnO exhibit similar behavior to cubic zinc blend structure, while cubic rocksalt ZnO demonstrates notably different physical properties. Therefore, it can be concluded that the cubic zinc blend structure phase could be replaced with the hexagonal wurtzite phase in case of growing on closely cubic lattice-matched substrates [40].

ZnO is a versatile semiconductor material with a direct wide band gap of 3.37 eV and a large excitation binding energy (60 meV) [42]. The unique crystalline structure of ZnO, combined with its wide bandgap and versatile properties, makes it highly regarded as one of the most promising semiconductors for a wide array of applications from electronics and optoelectronics to energy, healthcare, and environmental monitoring. These remarkable properties have attracted considerable interest, particularly in the advancement of optoelectronic devices. ZnO's distinct characteristics can be attributed to the fact that, among all elements in the sixth group of the periodic table, oxygen possesses the highest ionization energy, resulting in a strong interaction between Zn 3d and O 2p orbitals [47].

ZnO is utilized in UV absorption, antibacterial treatments, catalysts, photocatalysis, and various biological applications, owing to its remarkable biocompatibility, low toxicity, and cost-effectiveness [48]. Furthermore, ZnO nanostructures are of particular interest for a front contact with solar cells, which can avoid the shadow effect connected with metal finger contacts [49]. Furthermore, ZnO's wurtzite structure, which lacks a center of symmetry, along with its significant electromechanical coupling effects, makes it useful for piezoelectric sensors and nanogenerator [50, 51].

ZnO is employed as a gas sensor due to its high sensitivity to volatile and other gases, its high chemical stability, suitability to doping, non-toxicity, and low cost [52]. Studies have shown that factors like surface morphology, grain size, and defects in metal oxide semiconductors play crucial roles in their gas sensing performance. Recent developments involve the use of novel techniques to fabricate metal oxides with different morphologies, which can improve their gas

sensing properties [53, 54]. However, the metal oxides gas sensing devices show poor chemical selectivity due to resistance changes when exposed to other gaseous species. Thus, by combining sensing materials through doping, composite preparation, and surface modification, researchers have enhanced gas sensing performance factors such as selectivity, gas sensing response, recovery, and response time [55]. Also, different techniques have been used to synthesize heterostructures, which can form an electron accumulation layer and enhance the adsorption of oxygen ions [56].

2.2.3 Copper oxide (CuO)

CuO is a semiconducting material with a monoclinic structure. Figure 2.5 illustrates the process of monoclinic crystal formation in CuO. Initially, in Figure 2.5a, the Cu lattice adopts a face-centered cubic structure (FCC). Upon interaction with oxygen molecules, CuO molecules are produced. During CuO lattice formation, each copper atom becomes surrounded by four oxygen atoms, resulting in a coordination number of 4, as depicted in Figure 2.5b. This arrangement forms dominant (111) planes that align and stack along the growth direction of (010), as shown in Figure 2.5c. However, as oxygen atoms are incorporated into the Cu lattice, the face-centered cubic unit cell of copper no longer exists, leading to various atom rearrangements and lattice/unit cell reconstruction. Finally, the monoclinic unit cell of CuO is generated. Despite significant energy differences between the high-symmetry FCC lattice of copper and the low-symmetry monoclinic unit cell of CuO, the structure is stabilized due to the highly stable Cu^{2+} valence state [57]. Also, the CuO crystalline structure belongs to C2/c space group with four CuO formula units per unit cell.

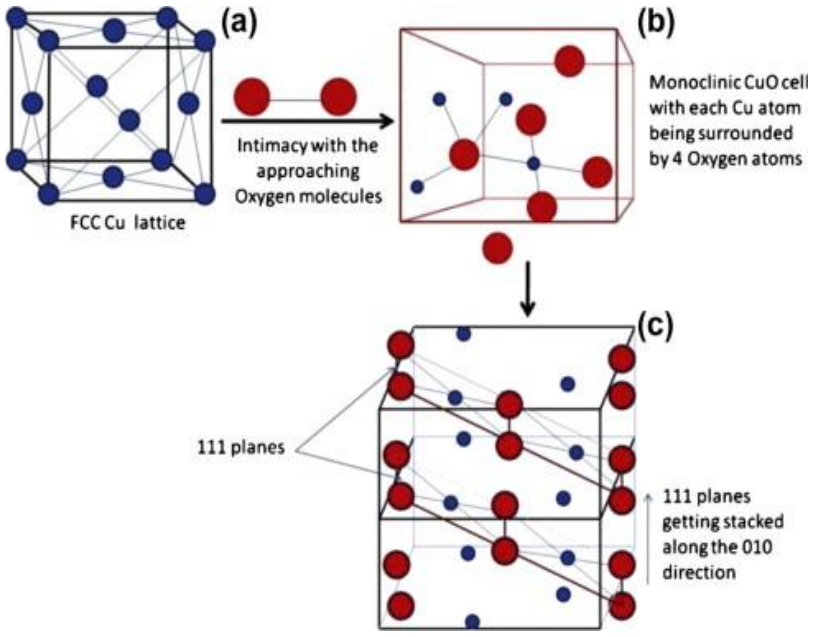

Figure 2.5 Schematic representation of CuO formation at the molecular level from a crystallographic perspective. The blue balls represent Cu atoms, and the red balls represent O atoms. (a) FCC lattice of Cu, (b) Monoclinic cell of CuO and (c) Two unit cells joined by a common face, showing the stacking of the (111) planes.

CuO has a narrow band gap (E_g = 1.2 eV) and exhibits a range of useful physical characteristics, making it highly potential for some applications requiring superconductivity, large magnetoresistance, and piezoelectric properties [58]. Due to its exceptional physical and electronic properties, CuO has found applications in gas sensing, lithium-copper oxide electrochemical cells, and magnetic data storage [59]. Also, it can be used for fabricating solar cells due to its photoconductive and photochemical properties [60]. Furthermore, CuO nanostructures are essential p-type semiconductors with several advantageous properties, including conductivity, a direct bandgap, thermal stability, low toxicity, excellent semiconducting characteristics, cost-effective synthesis, and high electrical conductivity among p-type semiconductor materials. CuO is particularly promising as a photocatalyst due to its optical properties, stability, and the presence of both Cu^{1+} and Cu^{2+} in different crystal systems [61, 62]. However, it suffers from limitations like a limited surface area, wide bandgap, and poor conductivity, resulting in poor photocatalysis performance [63]. To overcome these challenges, CuO nanoarchitecture formation can enhance its surface area and improvements in intrinsic and extrinsic conductivity can be achieved through doping and composite formation. Doping with

suitable metal cations is a constructive approach that not only reduces the bandgap but also enhances electrical properties [64].

In this thesis, gas sensing properties of CuO-based material have been studied because p-type oxides exhibit better selectivity compared to n-type oxides [65, 66]. Moreover, p-type oxides tend to exchange lattice oxygen with the surrounding air. Therefore, this characteristic helps in maintaining the stoichiometry of the oxides for a long time, enhancing the stability of the sensor [67]. Then, CuO-ZnO composite has been fabricated to improve gas sensing performance and electrical properties due to its excellent tunable catalytic, electrical, optical, and magnetic properties as well as its environmentally friendly nature. Also, composite formation can provide more active sites that promote mass and electron transfer, resulting in improvement in gas sensing properties [68]. Therefore, the gas sensing performance of CuO and CuO-ZnO composite have been studied in this thesis.

2.2.4 Vanadium pentoxide (V_2O_5)

Several polymorphic phases of V_2O_5 have been identified, including α-V_2O_5 (orthorhombic), β-V_2O_5 (monoclinic or tetragonal), and δ-V_2O_5 (a modification of β-V_2O_5 and easily reverts to α-V_2O_5 upon heating at a temperature higher than 340 °C) [69]. The α-V_2O_5 is considered the most stable, with the Pmmn space group and lattice parameters a = 11.512, b = 3.564, and c = 4.368 Å. The crystal structure consists of VO_5 square pyramids sharing edges and corners (Figure 2.6), with weak V–O interactions (van der Waals type) facilitating easy cleavage along the (001) planes. The layered structure of α-V_2O_5 is held together by these interactions [70, 71]. Computational thermodynamics indicates that V_2O_5 remains stable up to its melting point under oxygen partial pressures exceeding 100 Pa. The application of external pressure results in a notable 25-fold increase in electric conductivity. While no confirmed insulator-to-metal transition occurs in bulk, a reversible transition is reported for the (001) surface at 350–400 K, attributed to the anisotropic growth of vanadyl oxygen vacancies [72]. Metastable phases (β, γ, and δ) can be obtained through transitions from α-V_2O_5 at high temperatures or pressures [69].

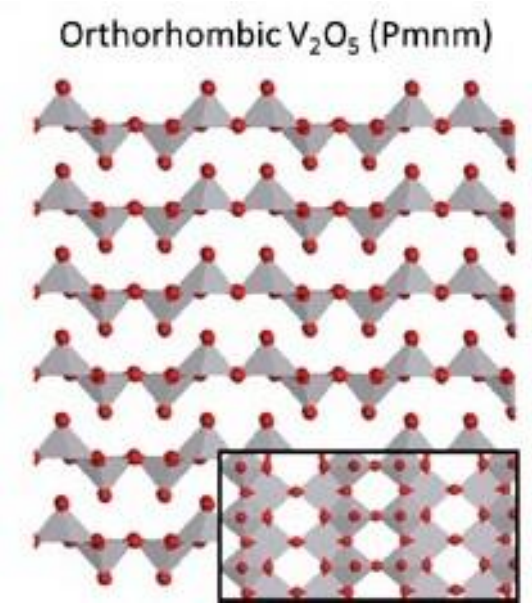

Figure 2.6 View along the a-axis of the lattice of V_2O_5 (view along the c-axis is provided as an inset) [72].

Vanadium, the 23rd element in the periodic table, belongs to the fifth group [73]. Vanadium oxides (VO_x) exhibit varying oxidation states ranging from +II to +V, such as VO, VO_2, V_2O_3, V_2O_4, and V_2O_5 due to their external configuration ($3d^3$ $4s^2$). These oxides differ in terms of chemical stability, electrical properties and toxicity [72, 74]. Vanadium pentoxide, as a transition metal oxide, is a well-known n-type semiconductor with an approximate band gap of 2.3 eV [75, 76]. Although the conductivity of vanadium pentoxide films, commonly utilized in gas sensing applications, is relatively low, it exhibits high sensitivity to temperature [75]. Furthermore, the material undergoes a reversible and swift transition from a semiconductor to a metal around 257 °C, known as the metal-to-insulator transition (MIT). While this property facilitates the development of thermally activated electrical and optical switches [77], it limits its applicability in gas sensing under harsh conditions or at temperatures exceeding the MIT threshold. Furthermore, the electrical conductivity of vanadium pentoxide is the result of electron hopping between $V_2(+IV)O_4$ and $V_2(+V)O_5$. Among metal oxides, vanadium pentoxide (V_2O_5) possesses a unique electrical property that allows it to be the sole metal oxide capable of detecting helium gas, an inert gas. Thus, gas sensing mechanisms are not based on electron exchange phenomena. These small atoms can intercalate the crystal matrix of V_2O_5, creating new sites for

electron hopping and enhancing electron mobility within the semiconductor's core. Therefore, variations in material conductivity directly correlate with the concentration of helium in the surrounding environment [78].

VO_x have attracted significant attention in energy storage due to their layered structure, multiple oxidation states (III-V), earth abundance, and low cost. Among the various VO_x materials, V_2O_5 has emerged as a promising candidate for energy storage. It possesses the highest oxidation state of vanadium, which enables it to store a greater number of electrons per formula unit, providing better stability [79-81]. However, the electrochemical performance of V_2O_5 such as poor rate capacity and cycling stability is hindered by issues including poor conductivity, low ion diffusion coefficient and irreversible structural changes during cycling [82]. To fully exploit the potential of V_2O_5 as an electrode in Li-ion batteries, various nanostructures with different morphologies, such as one-dimensional nanowires, nanobelts, two-dimensional nanosheets, and three-dimensional aerogels and porous spheres, have been developed. These different morphologies offer improved rate capability, cycle stability, shorter ion diffusion pathway, increased diffusion coefficient, and enhanced structural stability [82, 83]. Furthermore, the porous structure can effectively absorb the substantial stress and strain resulting from volume changes during the intercalation and deintercalation of Li^+ ions. Additionally, increased porosity plays a crucial role in improving charge transport [83]. Thus, the aim of this thesis is to fabricate V_2O_5 with a specific microstructure and high porosity for anodes which is expected to enhance electrochemical performance.

Conclusion

The chapter has discussed the advantages of utilizing nanomaterials, emphasizing their enhanced performance in gas sensors due to increased surface-to-volume ratios and unique structural effects at the nanoscale. Additionally, it has explained the benefits of nanomaterials in battery technologies, including improved electrochemical performances and the potential for ultrathin, flexible battery designs. Finally, it has provided insights into the crystalline structures,

properties and possible application of tungsten trioxide, zinc oxide, copper oxide, and vanadium pentoxide, which are studied in this thesis.

References

[1] Z. Sun, T. Liao, L. Kou, Strategies for designing metal oxide nanostructures, (2017).
[2] A. Kaushik, R. Kumar, S.K. Arya, M. Nair, B. Malhotra, S. Bhansali, Organic–inorganic hybrid nanocomposite-based gas sensors for environmental monitoring, Chemical reviews, 115 (2015) 4571-4606.
[3] C. Xu, J. Tamaki, N. Miura, N. Yamazoe, Grain size effects on gas sensitivity of porous SnO_2-based elements, Sensors and Actuators B: Chemical, 3 (1991) 147-155.
[4] Y.G. Song, Y.S. Shim, J.M. Suh, M.S. Noh, G.S. Kim, K.S. Choi, B. Jeong, S. Kim, H.W. Jang, B.K. Ju, Ionic-activated chemiresistive gas sensors for room-temperature operation, Small, 15 (2019) 1902065.
[5] G.H. Jeong, S.P. Sasikala, T. Yun, G.Y. Lee, W.J. Lee, S.O. Kim, Nanoscale assembly of 2D materials for energy and environmental applications, Advanced Materials, 32 (2020) 1907006.
[6] Y. Liang, Y. Yang, C. Zou, K. Xu, X. Luo, T. Luo, J. Li, Q. Yang, P. Shi, C. Yuan, 2D ultra-thin WO_3 nanosheets with dominant {002} crystal facets for high-performance xylene sensing and methyl orange photocatalytic degradation, Journal of Alloys and Compounds, 783 (2019) 848-854.
[7] H. Hashtroudi, I.D. Mackinnon, M. Shafiei, Emerging 2D hybrid nanomaterials: Towards enhanced sensitive and selective conductometric gas sensors at room temperature, Journal of Materials Chemistry C, 8 (2020) 13108-13126.
[8] T. Zhao, P. Qiu, Y. Fan, J. Yang, W. Jiang, L. Wang, Y. Deng, W. Luo, Hierarchical branched mesoporous TiO_2–SnO_2 nanocomposites with well-defined n–n heterojunctions for highly efficient ethanol sensing, Advanced Science, 6 (2019) 1902008.
[9] E. Llobet, Gas sensors using carbon nanomaterials: A review, Sensors and Actuators B: Chemical, 179 (2013) 32-45.
[10] V. Galstyan, “Quantum dots: Perspectives in next-generation chemical gas sensors”–A review, Analytica Chimica Acta, 1152 (2021) 238192.
[11] C. Dong, R. Zhao, L. Yao, Y. Ran, X. Zhang, Y. Wang, A review on WO_3 based gas sensors: Morphology control and enhanced sensing properties, Journal of Alloys and Compounds, 820 (2020) 153194.
[12] A. Manthiram, A.V. Murugan, A. Sarkar, T. Muraliganth, Nanostructured electrode materials for electrochemical energy storage and conversion, Energy & Environmental Science, 1 (2008) 621-638.
[13] R. Huggins, W. Nix, Decrepitation model for capacity loss during cycling of alloys in rechargeable electrochemical systems, Ionics, 6 (2000) 57-63.
[14] R. Teki, M.K. Datta, R. Krishnan, T.C. Parker, T.M. Lu, P.N. Kumta, N. Koratkar, Nanostructured silicon anodes for lithium ion rechargeable batteries, small, 5 (2009) 2236-2242.
[15] Y. Zhao, G. Liu, L. Liu, Z. Jiang, High-performance thin-film Li_4 Ti_5 O_{12} electrodes fabricated by using ink-jet printing technique and their electrochemical properties, Journal of Solid State Electrochemistry, 13 (2009) 705-711.
[16] M. Ahmed, Chapter 16 - Nanomaterial synthesis, in: R. Narain (Ed.) Polymer Science and Nanotechnology, Elsevier2020, pp. 361-399.
[17] G. Salas, R. Costo, M. del Puerto Morales, Synthesis of inorganic nanoparticles, Frontiers of Nanoscience, Elsevier2012, pp. 35-79.
[18] G. Romero, S.E. Moya, Synthesis of organic nanoparticles, Frontiers of nanoscience, Elsevier2012, pp. 115-141.

[19] S. Bhaviripudi, E. Mile, S.A. Steiner, A.T. Zare, M.S. Dresselhaus, A.M. Belcher, J. Kong, CVD synthesis of single-walled carbon nanotubes from gold nanoparticle catalysts, Journal of the American Chemical Society, 129 (2007) 1516-1517.
[20] N. Abid, A.M. Khan, S. Shujait, K. Chaudhary, M. Ikram, M. Imran, J. Haider, M. Khan, Q. Khan, M. Maqbool, Synthesis of nanomaterials using various top-down and bottom-up approaches, influencing factors, advantages, and disadvantages: A review, Advances in Colloid and Interface Science, 300 (2022) 102597.
[21] D. Migas, V. Shaposhnikov, V. Rodin, V. Borisenko, Tungsten oxides. I. Effects of oxygen vacancies and doping on electronic and optical properties of different phases of WO_3, Journal of Applied Physics, 108 (2010).
[22] H. Quan, Y. Gao, W. Wang, Tungsten oxide-based visible light-driven photocatalysts: crystal and electronic structures and strategies for photocatalytic efficiency enhancement, Inorganic Chemistry Frontiers, 7 (2020) 817-838.
[23] H. Zheng, J.Z. Ou, M.S. Strano, R.B. Kaner, A. Mitchell, K. Kalantar-zadeh, Nanostructured tungsten oxide–properties, synthesis, and applications, Advanced Functional Materials, 21 (2011) 2175-2196.
[24] H.A. Evans, Y. Wu, R. Seshadri, A.K. Cheetham, Perovskite-related ReO_3-type structures, Nature Reviews Materials, 5 (2020) 196-213.
[25] H. Yang, H. Sun, Q. Li, P. Li, K. Song, B. Song, L. Wang, Structural, electronic, optical and lattice dynamic properties of the different WO_3 phases: First-principle calculation, Vacuum, 164 (2019) 411-420.
[26] E.K. Salje, S. Rehmann, F. Pobell, D. Morris, K.S. Knight, T. Herrmannsdörfer, M.T. Dove, Crystal structure and paramagnetic behaviour of, Journal of Physics: Condensed Matter, 9 (1997) 6563.
[27] S. Balaji, Y. Djaoued, A.-S. Albert, R.Z. Ferguson, R. Brüning, Hexagonal tungsten oxide based electrochromic devices: spectroscopic evidence for the Li ion occupancy of four-coordinated square windows, Chemistry of Materials, 21 (2009) 1381-1389.
[28] B. Gerand, G. Nowogrocki, J. Guenot, M. Figlarz, Structural study of a new hexagonal form of tungsten trioxide, Journal of Solid State Chemistry, 29 (1979) 429-434.
[29] M. Gillet, K. Aguir, C. Lemire, E. Gillet, K. Schierbaum, The structure and electrical conductivity of vacuum-annealed WO_3 thin films, Thin Solid Films, 467 (2004) 239-246.
[30] S. Gullapalli, R. Vemuri, C. Ramana, Structural transformation induced changes in the optical properties of nanocrystalline tungsten oxide thin films, Applied physics letters, 96 (2010).
[31] K. Aguir, C. Lemire, D. Lollman, Electrical properties of reactively sputtered WO_3 thin films as ozone gas sensor, Sensors and actuators B: Chemical, 84 (2002) 1-5.
[32] V. Makarov, M. Trontelj, Sintering and electrical conductivity of doped WO_3, Journal of the European Ceramic Society, 16 (1996) 791-794.
[33] R. Vemuri, K.K. Bharathi, S. Gullapalli, C. Ramana, Effect of structure and size on the electrical properties of nanocrystalline WO_3 films, ACS applied materials & interfaces, 2 (2010) 2623-2628.
[34] M. Deepa, A. Joshi, A. Srivastava, S. Shivaprasad, S. Agnihotry, Electrochromic nanostructured tungsten oxide films by sol-gel: Structure and intercalation properties, Journal of The Electrochemical Society, 153 (2006) C365.
[35] S.H. Lee, R. Deshpande, P.A. Parilla, K.M. Jones, B. To, A.H. Mahan, A.C. Dillon, Crystalline WO_3 nanoparticles for highly improved electrochromic applications, Advanced Materials, 18 (2006) 763-766.
[36] J. Wang, E. Khoo, P.S. Lee, J. Ma, Controlled synthesis of WO_3 nanorods and their electrochromic properties in H_2SO_4 electrolyte, The Journal of Physical Chemistry C, 113 (2009) 9655-9658.
[37] M. Yang, N.K. Shrestha, P. Schmuki, Thick porous tungsten trioxide films by anodization of tungsten in fluoride containing phosphoric acid electrolyte, Electrochemistry Communications, 11 (2009) 1908-1911.
[38] Y. Djaoued, S. Balaji, R. Brüning, Electrochromic Devices Based on Porous Tungsten Oxide Thin Films, Journal of Nanomaterials, 2012 (2012) 674168.

[39] Y. Lu, G. Liu, J. Zhang, Z. Feng, C. Li, Z. Li, Fabrication of a monoclinic/hexagonal junction in WO_3 and its enhanced photocatalytic degradation of rhodamine B, Chinese Journal of Catalysis, 37 (2016) 349-358.
[40] F.-G. Kuang, X.-Y. Kuang, S.-Y. Kang, M.-M. Zhong, X.-W. Sun, Ab initio study on physical properties of wurtzite, zincblende, and rocksalt structures of zinc oxide using revised functionals, Materials Science in Semiconductor Processing, 31 (2015) 700-708.
[41] O. Dulub, L.A. Boatner, U. Diebold, STM study of the geometric and electronic structure of ZnO (0001)-Zn,(0001)-O,(1010), and (1120) surfaces, Surface Science, 519 (2002) 201-217.
[42] Z.L. Wang, Nanostructures of zinc oxide, Materials today, 7 (2004) 26-33.
[43] V.A. Coleman, C. Jagadish, Basic properties and applications of ZnO, Zinc oxide bulk, thin films and nanostructures, Elsevier2006, pp. 1-20.
[44] A. Ashrafi, C. Jagadish, Review of zincblende ZnO: Stability of metastable ZnO phases, Journal of Applied Physics, 102 (2007).
[45] J. Jaffe, R. Pandey, A. Kunz, Electronic structure of the rocksalt-structure semiconductors ZnO and CdO, Physical Review B, 43 (1991) 14030.
[46] R.S. Koster, C.M. Fang, M. Dijkstra, A. Van Blaaderen, M.A. Van Huis, Stabilization of rock salt ZnO nanocrystals by low-energy surfaces and Mg additions: A first-principles study, The Journal of Physical Chemistry C, 119 (2015) 5648-5656.
[47] K. Ellmer, A. Klein, B. Rech, Transparent conductive zinc oxide: basics and applications in thin film solar cells, (2007).
[48] M. Vaseem, A. Umar, Y.-B. Hahn, ZnO nanoparticles: growth, properties, and applications, Metal oxide nanostructures and their applications, 5 (2010) 10-20.
[49] C. Klingshirn, ZnO: From basics towards applications, physica status solidi (b), 244 (2007) 3027-3073.
[50] Z.L. Wang, J. Song, Piezoelectric nanogenerators based on zinc oxide nanowire arrays, Science, 312 (2006) 242-246.
[51] Z.L. Wang, Nanopiezotronics, Advanced Materials, 19 (2007) 889-892.
[52] M. Suchea, S. Christoulakis, K. Moschovis, N. Katsarakis, G. Kiriakidis, ZnO transparent thin films for gas sensor applications, Thin solid films, 515 (2006) 551-554.
[53] M. Ahmad, J. Zhu, ZnO based advanced functional nanostructures: synthesis, properties and applications, Journal of Materials chemistry, 21 (2011) 599-614.
[54] X. Zhou, A. Wang, Y. Wang, L. Bian, Z. Yang, Y. Bian, Y. Gong, X. Wu, N. Han, Y. Chen, Crystal-defect-dependent gas-sensing mechanism of the single ZnO nanowire sensors, ACS sensors, 3 (2018) 2385-2393.
[55] G. Korotcenkov, B. Cho, Metal oxide composites in conductometric gas sensors: Achievements and challenges, Sensors and Actuators B: Chemical, 244 (2017) 182-210.
[56] M. Shajahani, H.R. Dizaji, Mechanism of CO and acetone adsorption on ZnO and Pt-doped ZnO surfaces for gas sensing applications: A DFT investigation, Chemical Physics Letters, 832 (2023) 140884.
[57] K.K. Dey, A. Kumar, R. Shanker, A. Dhawan, M. Wan, R.R. Yadav, A.K. Srivastava, Growth morphologies, phase formation, optical & biological responses of nanostructures of CuO and their application as cooling fluid in high energy density devices, RSC advances, 2 (2012) 1387-1403.
[58] M. Dar, Q. Ahsanulhaq, Y. Kim, J. Sohn, W. Kim, H. Shin, Versatile synthesis of rectangular shaped nanobat-like CuO nanostructures by hydrothermal method; structural properties and growth mechanism, Applied Surface Science, 255 (2009) 6279-6284.
[59] F. Bayansal, S. Kahraman, G. Çankaya, H.A. Çetinkara, H.S. Güder, H.M. Çakmak, Growth of homogenous CuO nano-structured thin films by a simple solution method, Journal of Alloys and Compounds, 509 (2011) 2094-2098.
[60] Y. Xu, D. Chen, X. Jiao, Fabrication of CuO Pricky Microspheres with Tunable Size by a Simple Solution Route, The Journal of Physical Chemistry B, 109 (2005) 13561-13566.

[61] A. El-Trass, H. ElShamy, I. El-Mehasseb, M. El-Kemary, CuO nanoparticles: Synthesis, characterization, optical properties and interaction with amino acids, Applied Surface Science, 258 (2012) 2997-3001.
[62] M. Tariq, M.D. Koch, J.W. Andrews, K.E. Knowles, Correlation between Surface Chemistry and Optical Properties in Colloidal Cu_2O Nanoparticles, The Journal of Physical Chemistry C, 124 (2020) 4810-4819.
[63] H. Wang, J.-Z. Xu, J.-J. Zhu, H.-Y. Chen, Preparation of CuO nanoparticles by microwave irradiation, Journal of Crystal Growth, 244 (2002) 88-94.
[64] A. ur Rehman, M. Aadil, S. Zulfiqar, P.O. Agboola, I. Shakir, M.F. Aly Aboud, S. Haider, M.F. Warsi, Fabrication of binary metal doped CuO nanocatalyst and their application for the industrial effluents treatment, Ceramics International, 47 (2021) 5929-5937.
[65] M. Hübner, C.E. Simion, A. Tomescu-Stănoiu, S. Pokhrel, N. Bârsan, U. Weimar, Influence of humidity on CO sensing with p-type CuO thick film gas sensors, Sensors and Actuators B: Chemical, 153 (2011) 347-353.
[66] H.-J. Kim, J.-H. Lee, Highly sensitive and selective gas sensors using p-type oxide semiconductors: Overview, Sensors and Actuators B: Chemical, 192 (2014) 607-627.
[67] D.M. Chethana, T.C. Thanuja, H.M. Mahesh, M.S. Kiruba, A.S. Jose, H.C. Barshilia, J. Manjanna, Synthesis, structural, magnetic and NO_2 gas sensing property of CuO nanoparticles, Ceramics International, 47 (2021) 10381-10387.
[68] S. Das, V.C. Srivastava, An overview of the synthesis of CuO-ZnO nanocomposite for environmental and other applications, Nanotechnology Reviews, 7 (2018) 267-282.
[69] P. Balog, D. Orosel, Z. Cancarevic, C. Schön, M. Jansen, V_2O_5 phase diagram revisited at high pressures and high temperatures, Journal of Alloys and Compounds, 429 (2007) 87-98.
[70] N. Fateh, G. Fontalvo, C. Mitterer, Structural and mechanical properties of dc and pulsed dc reactive magnetron sputtered V_2O_5 films, Journal of Physics D: Applied Physics, 40 (2007) 7716.
[71] R.R. Kumar, B. Karunagaran, V.S. Kumar, Y. Jeyachandran, D. Mangalaraj, S.K. Narayandass, Structural properties of V_2O_5 thin films prepared by vacuum evaporation, Materials Science in semiconductor processing, 6 (2003) 543-546.
[72] N. Bahlawane, D. Lenoble, Vanadium Oxide Compounds: Structure, Properties, and Growth from the Gas Phase, Chemical Vapor Deposition, 20 (2014) 299-311.
[73] M. Gasik, Technology of Vanadium Ferroalloys, Handbook of Ferroalloys, Elsevier2013, pp. 397-409.
[74] J. Leuschner, H. Haschke, G. Sturm, New investigations on acute toxicities of vanadium oxides, Monatshefte fur Chemie, 125 (1994) 623-646.
[75] X. Sheng, Z. Li, Y. Cheng, Electronic and thermoelectric properties of V_2O_5, MgV_2O_5, and CaV_2O_5, Coatings, 10 (2020) 453.
[76] M. Benmoussa, E. Ibnouelghazi, A. Bennouna, E. Ameziane, Structural, electrical and optical properties of sputtered vanadium pentoxide thin films, Thin solid films, 265 (1995) 22-28.
[77] A. Chakrabarti, K. Hermann, R. Druzinic, M. Witko, F. Wagner, M. Petersen, Geometric and electronic structure of vanadium pentoxide: A density functional bulk and surface study, Physical review B, 59 (1999) 10583.
[78] P.S. Chauhan, A. Mishra, G. Bhatt, S. Bhattacharya, Enhanced He gas detection by V_2O_5-noble metal (Au, Ag, and Pd) nanocomposite with temperature dependent n-to p-type transition, Materials Science in Semiconductor Processing, 123 (2021) 105528.
[79] J. Zheng, Y. Zhang, T. Hu, T. Lv, C. Meng, New strategy for the morphology-controlled synthesis of V_2O_5 microcrystals with enhanced capacitance as battery-type supercapacitor electrodes, Crystal Growth & Design, 18 (2018) 5365-5376.
[80] Y. Yue, H. Liang, Micro- and Nano-Structured Vanadium Pentoxide (V_2O_5) for Electrodes of Lithium-Ion Batteries, Advanced Energy Materials, 7 (2017) 1602545.

[81] M. Sahana, C. Sudakar, C. Thapa, G. Lawes, V. Naik, R. Baird, G. Auner, R. Naik, K. Padmanabhan, Electrochemical properties of V_2O_5 thin films deposited by spin coating, Materials Science and Engineering: B, 143 (2007) 42-50.
[82] X. Liang, G. Gao, G. Wu, H. Yang, Synthesis and characterization of novel hierarchical starfish-like vanadium oxide and their electrochemical performance, Electrochimica Acta, 188 (2016) 625-635.
[83] X. Huang, X. Rui, H.H. Hng, Q. Yan, Vanadium Pentoxide-Based Cathode Materials for Lithium-Ion Batteries: Morphology Control, Carbon Hybridization, and Cation Doping, Particle & Particle Systems Characterization, 32 (2015) 276-294.

Chapter 3: Nanomaterial Synthesis Methods, Characterization and Device Fabrication

Introduction

This chapter introduces two synthesis methods for the preparation of metal oxide nanoparticles: the sol-gel method and the polyol method. The chapter also covers instruments, Li-ion batteries and sensor device fabrication. Furthermore, it provides insights into gas sensing and electrochemical measurements and the fabrication process of gas sensing devices and anode of Li-ion batteries.

3.1 Synthesis method

3.1.1 Sol-gel method

The sol-gel method is a well-established synthetic approach for preparing metal oxide nanoparticles and mixed oxide composites, offering excellent control over material texture and surface properties. This method involves five key steps: hydrolysis, polycondensation, aging, drying, and thermal decomposition [1].

In the initial stage, hydrolysis of precursors, such as metal alkoxides, takes place in water or alcohol. The presence of oxygen, supplied by water or organic solvents (such as alcohols), is crucial for the formation of metal oxides. The choice of reaction medium distinguishes between the aqueous sol-gel method (using water) and the nonaqueous sol-gel route (employing organic solvents). The hydrolysis process involves the following reaction:

$$M - OR + H_2O \rightarrow MOH + ROH\ (Hydrolysis) \quad (1)$$

Where M=metal, R=alkyl group (C_nH_{2n+1})

The quantity of water significantly influences gel formation. The higher water content promotes the formation of polymerized and branched structures during condensation [2]. Similar to the non-hydrolytic fabrication of larger-scale metal oxide gels, the oxygen necessary for nanoparticle generation is supplied either by the solvent (such as ethers, alcohols, ketones, or aldehydes) or by the organic component of the precursor (alkoxides or acetylacetonates).

The condensation step involves the condensation of adjacent molecules, where water or alcohol is eliminated, forming metal oxide linkages. Two processes, olation and oxolation, drive condensation. Olation forms hydroxyl (–OH–) bridges between metal centers, while oxolation creates oxo (–O–) bridges. The general condensation reaction is as follows:

$$M - OH + XO - M \rightarrow M - O - M + XOH\ (Condensation) \quad (2)$$

Where M=metal, X=H or alkyl group (C_nH_{2n+1})

The condensation process in the nonaqueous method is explained through four equations. Equation 3 illustrates the condensation between metal halides and metal alkoxides, formed by the reaction of metal halides with alcohols, resulting in the release of an alkyl halide. Ether elimination (Equation 4) leads to the formation of M–O–M bond when two metal alkoxides condense, eliminating an organic ether. The ester elimination process (Equation 5) involves the interaction between metal carboxylates and metal alkoxides. Similar to ester eliminations, amide eliminations also occur. In cases where ketones serve as solvents, the release of oxygen typically entails aldol condensation, where two carbonyl compounds react, formally eliminating water. Water molecules act as the oxygen-supplying agent for metal oxide formation (Equation 6) [3].

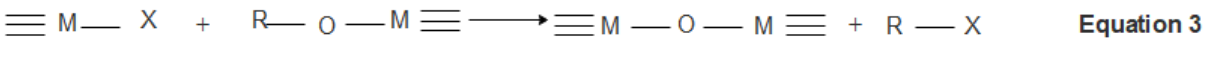

Equation 3

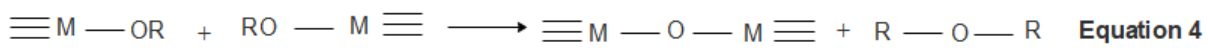

Equation 4

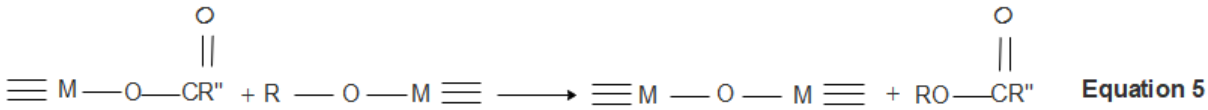

Equation 5

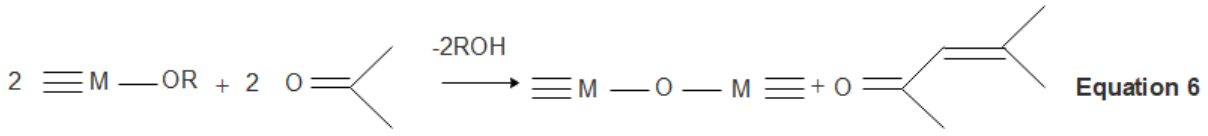

Equation 6

Condensation increases the solvent viscosity, leading to gel formation characterized by a porous structure in the liquid phase. The size and cross-linking of colloidal particles depend on the alkoxide precursor and pH of the solution.

The aging process induces changes in the gel's structure and properties. Continuous polycondensation and reprecipitation of the gel network occur during aging, reducing porosity and increasing thickness between colloidal particles.

Drying is a complex process involving the detachment of water and organic components to form a gel. Different drying methods, such as atmospheric/thermal drying, supercritical drying and freeze-drying, impact the gel network's structure (Figure 3.1). Heating the porous gel at high temperatures causes densification, resulting in xerogel formation with low surface area and pore volume. Supercritical drying forms aerogels with high pore volume, while freezing solvents produce cryogels with lower gel network shrinkage. Relative humidity during drying directly affects the stability and performance of nanomaterials.

The final step involves thermal treatment or calcination to eliminate residues and water molecules from the sample. The calcination temperature is crucial for controlling pore size, crystallization and material density.

The parameters that can be controlled in the sol-gel method include the concentration of precursor, nature of the solvent, pH of the solution, type of additives added and their concentrations, pre- and post-heat treatment of the materials, aging of the solution and nature of polymer used for condensation.

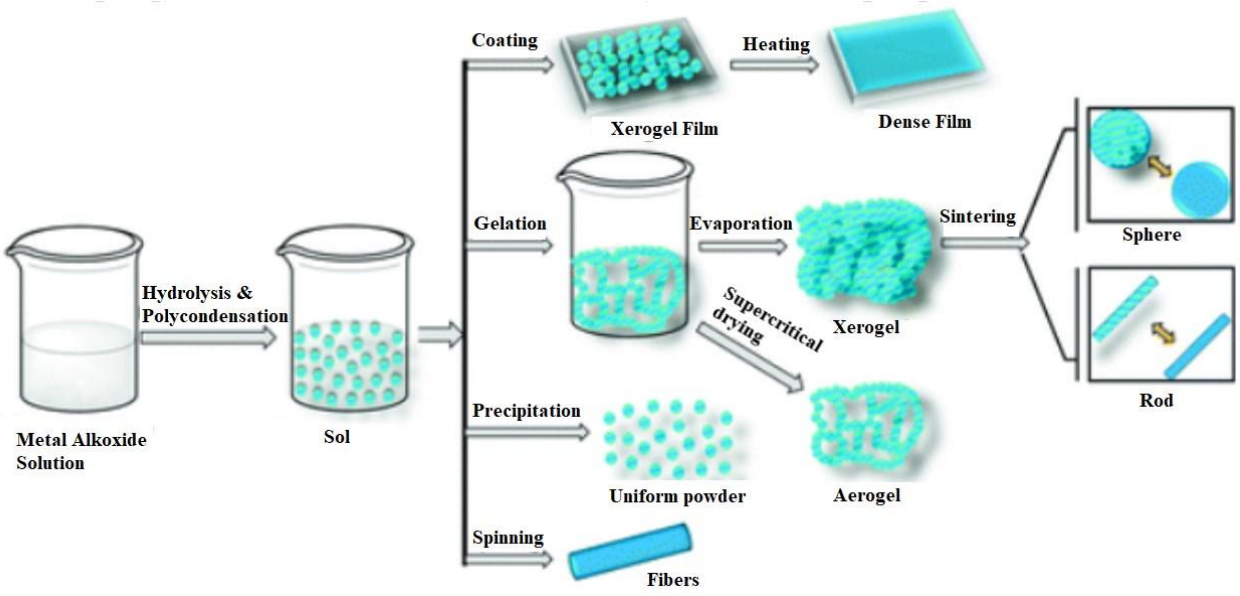

Figure 3.1 Schematic of sol-gel method [4].

3.1.2 Polyol method

The polyol method is a versatile and widely employed technique for synthesizing metal oxides. The methodology involves reducing metal precursors in a polyfunctional alcohol solvent, such as ethylene glycol or diethylene glycol. The process typically begins with the dissolution of metal salts in the chosen polyol solvent, forming a homogeneous precursor solution. Various properties of polyols, including high boiling points, dissolving capabilities, complex-forming abilities, reducing characteristics, protective features, and their amphiprotic nature, facilitate potential chemical reactions such as reduction, hydrolysis, and polymerization in the polyol method [5].

The research indicates that the formation of an inorganic compound in this medium is influenced by the precursor salt's anion. Nitrate is excluded from some studies due to its oxidizing nature, which can interfere with the polyol's reducing properties. In the case of chloride and sulfate salts, the solution remains clear after the precursor's dissolution, with no precipitation upon heating. Conversely, under identical conditions, when acetate is used, an inorganic compound precipitate. The nature of precipitate (metal, oxide, hydroxide) is

determined by two key factors: the hydrolysis ratio (defined by the water-to-metal molar ratio) and the reaction temperature [5].

Upon heating, the polyol undergoes thermal decomposition, acting as a capping agent and leading to the nucleation and growth of metal oxide nanoparticles. The reaction conditions, including temperature, reaction time, and precursor concentrations, play crucial roles in determining the size, morphology and crystallinity of the resulting metal oxide nanoparticles.

3.2 Instruments

3.2.1 Magnetron sputtering

Figure 3.2 presents the schematic diagram of the Kenotec sputtering plant. The sputtering plant comprises two distinct vacuum chambers, each serving a specific purpose within the system. The first is a large circular chamber, maintained at high vacuum levels and primarily designated for the deposition process. On the other hand, the second small tubular chamber, also known as the load-lock chamber, operates at low vacuum levels. The load-lock chamber facilitates the insertion and placement of samples without disrupting the vacuum in the deposition chamber. The connection between the two chambers is allowed by a gate valve.

The vacuum in the load-lock chamber is generated by a turbomolecular drag pumping station (TMH 064 DE), which employs an electronic drive unit. The deposition chamber obtains the required vacuum through the use of a rotary and turbomolecular pump. Also, the pump can reach an ultimate total pressure of approximately 10^{-3} mbar. Furthermore, the vacuum requirements within the deposition chamber are sustained by an Edwards nEXT 400 model rotationary turbomolecular pump. By incorporating these components, the sputtering plant can effectively maintain the desired vacuum conditions within each chamber, facilitating the deposition process in the high-vacuum circular chamber while preserving the integrity of the environment in the low-vacuum tubular chamber.

Four target positions and home positions are present in the deposition chamber for depositing various metal and metal oxide thin films. Two of these positions are connected to a DC power supply, while the remaining positions are connected to the RF power supply. The positioning of the sample holder is controlled by a computer-operated step-by-step motor.

The sputtering process operates on the principle of creating a plasma discharge from a gaseous discharge to bombard a target material. This bombardment results in the removal of target atoms, which can condense on a substrate, forming a thin film [6]. The deposition of the coating film can be precisely controlled by adjusting various parameters, including temperature (ranging from room temperature to 600 °C), plasma composition (argon and oxygen sourced from two controlled lines, with flux and pressure regulated by two mass flow controllers), chamber pressure, and the electrical power applied. To manage and monitor the system, a custom software program developed using Microsoft Access/Visual Basic, assumes full control.

In this thesis, magnetron sputtering has been employed for the deposition of the platinum (Pt) electrodes and heater of the gas sensing device.

Figure 3.2 Kenotec Sputtering system in Sensor Lab.

3.2.2 Gas test Chamber

Gas sensing measurements were conducted utilizing the flow-through technique within a thermostatic test chamber (Figure 3.3a). In this method, a steady flow of synthetic air (0.3 l/min) was mixed with the desired concentration of gases through a sealed chamber, which was maintained at 20 °C, atmospheric pressure, and a specific humidity level. Electrical data were continuously recorded by applying voltage (power supply) and measuring the generated current (using a picoammeter)**.** The conductance was determined as the ratio of the measured current (sampling time=30 s) to the applied voltage. The humidity level was determined using a humidity sensor in the test chamber. To generate air saturated with water, synthetic dry air initially passed through a water tank maintained at a constant temperature and then through a condenser that kept at the same temperature as the test chamber. The relative humidity was generated by mixing it with dry air. To obtain the desired analyte concentrations, synthetic air was mixed with gas compounds from certified bottles. This test system can measure the gas sensing performance of materials from room temperature to 600 °C. The sensing response of the fabricated n-type metal oxide structures toward reducing and oxidizing gases is calculated using the following equations, respectively:

$$\frac{(G_{f-}\, G_0)}{G_0} = \frac{\Delta G}{G_0} \tag{7}$$

$$\frac{(\mathrm{G_{0-}\, G_f})}{G_f} = \frac{\Delta \mathrm{G}}{\mathrm{G_f}} \tag{8}$$

Also, the p-type metal oxide gas sensing response toward reducing (Equation 9) and oxidizing (Equation 10) is displayed below:

$$\frac{(G_{0-}\, G_f)}{G_f} = \frac{\Delta G}{G_0} \tag{9}$$

$$\frac{(G_{f-}\, G_0)}{G_0} = \frac{\Delta G}{G_0} \tag{10}$$

In Equations 7−10, G_0 represents the initial conductance of the metal oxide sensor when exposed to air, while G_f denotes the stable conductance level of the sensor when the analyte

compound is present. The time required to achieve a conductance value of 90% of (G_f-G_0) after the gas injection defines the sensor response time (t_{res}). The recovery time (t_{rec}) is the interval needed to attain a conductance value of 70% of (G_f-G_0) upon restoring the airflow (as explained in chapter 1). The Mathworks MATLAB analysis program was employed to calculate response, t_{res}, and t_{rec} using the equations mentioned above.

Figure 3.3 a) Gas sensor test system image with all other instruments including computer, picoammeter, power supply and humidity chamber in sensor lab, b) Schematic of stainless-steel gas sensing chamber, c) Holder of sensors.

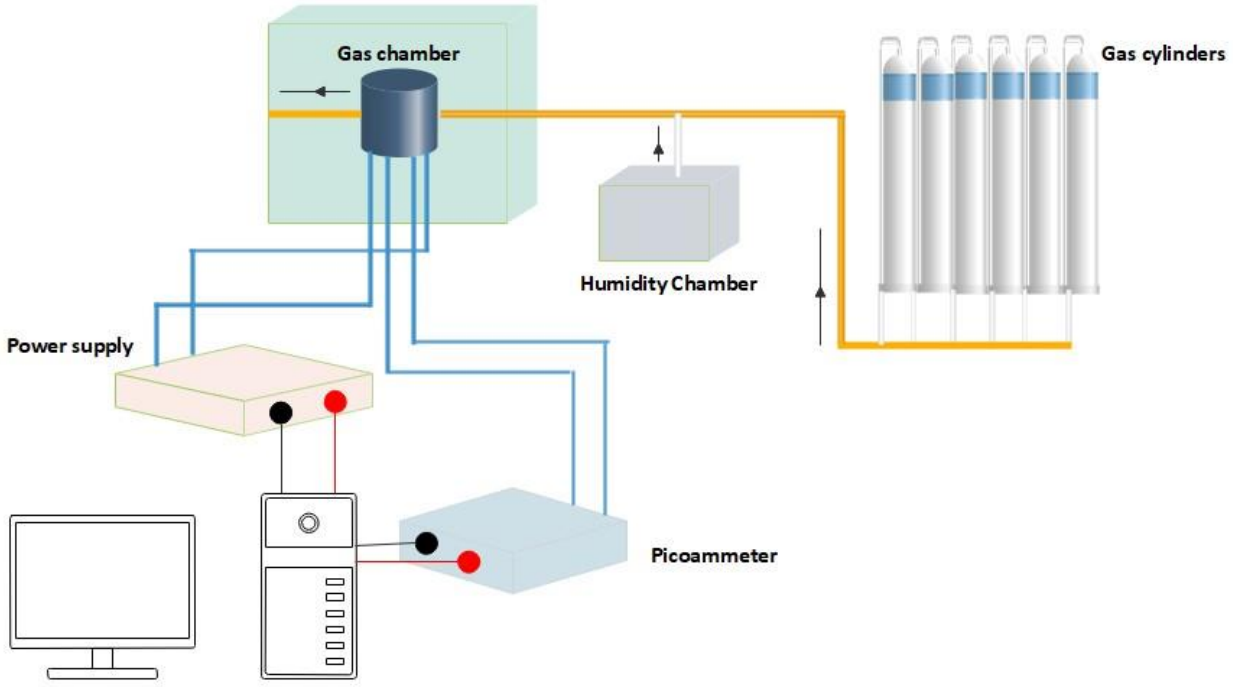

Figure 3.4 Schematic representation of gas measurement set up.

3.2.3 Electrochemical measurement for Li ion batteries

A CT2001 battery testing system (Landt Instruments, shown in Figure 3.5) was employed to conduct galvanostatic charge-discharge cycles at room temperature. The charge-discharge

curves illustrate the capacities during charging and discharging with voltage. To assess the long-term cycling stability of a battery, coin cells undergo multiple charge and discharge cycles, and the capacity is observed throughout these cycles. Increasing the current density during battery cycling provides insights into the capacity available for rapid charging or discharging. This thesis includes rate capability measurements where the current density is systematically increased over multiple cycles to evaluate overall capacity extraction. The performance at higher rates serves as an indicator of whether the electrochemical performance of the anode is constrained by lithium-ion or electronic conduction kinetics. The capacity retention, commonly referred to as cyclability, is typically expressed as a percentage of the initial capacity over a specified

number of cycles. Cyclic voltammetry (CV) was conducted at different scan rates using a Bio-Logic VMP3 potentiostat/galvanostat with a built-in electrochemical impedance spectroscopy (EIS) analyzer. The open circuit voltage (OCV) can check the possibility of short-circuiting.

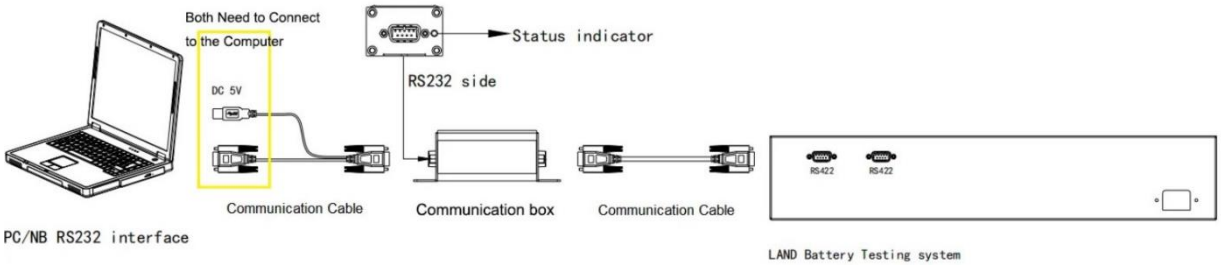

Figure 3.5 a) Overview of a CT2001 battery testing system and b) Schematic of Land system setup [7].

3.4 Device fabrication

3.3.1 Gas sensing device fabrication

First, alumina substrates (99.9% purity, 2 × 2 mm, Kyocera, Japan) were cleaned by sonication in acetone, ethanol, and H_2O. Subsequently, TiW adhesion films, Pt pad and Pt interdigitated electrodes were deposited on the alumina substrates using DC magnetron sputtering at specific conditions (Table 3.1) in the sputtering chamber. A Pt heater was deposited on the backside of the substrates (see Figure 3.6) to control the operating temperature of the sensing structure. Then, the substrates were mounted on top of the TO packages using electro-soldered gold wire. Sensor devices based on the prepared nanomaterials were fabricated using the drop-casting method. Metal oxide powders were added to various solvents with different concentrations to find optimal conditions, and then were sonicated from 10 to 60 minutes. The resulting dispersions were drop-casted onto the substrates with a different number of droplets using a

dispenser (micro pipet) (Gilson Company, France). To stabilize the electrical properties of the sensing structures, they were treated at 450 °C for a few days.

Table 3.1 Experimental parameters used in magnetron sputtering system for TiW pads, Pt pads, Pt interdigitated electrode and Pt heater.

Deposition sample	Magnetron power (W)	Pressure (mbar)	Ar flow (sccm)	Deposition time (min.)
TiW pads	70	5.1×10^{-3}	7	3
Pt pads	70	5.1×10^{-3}	7	3
Pt interdigitated electrode	70	5.1×10^{-3}	7	20
Pt heater	70	5.1×10^{-3}	7	20

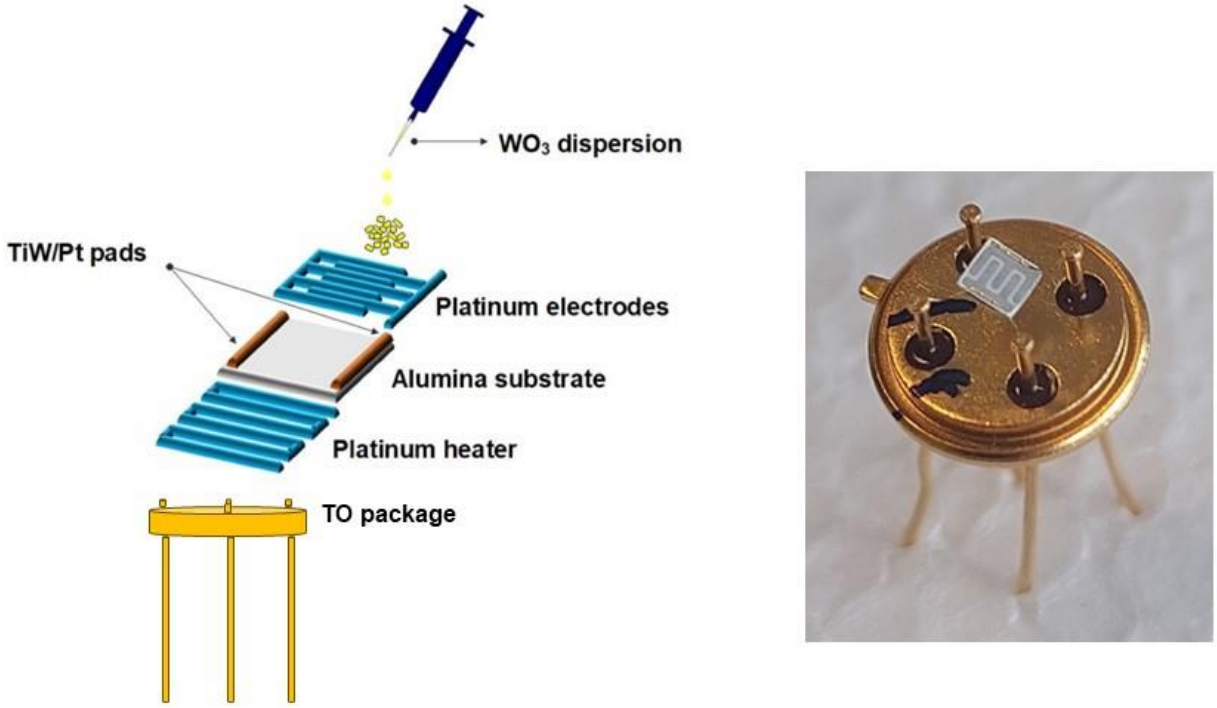

Figure 3.6 Schematic of gas sensor device.

3.3.2 Li ion batteries configuration and electrochemical measurement

Electrochemical measurements of materials as a Li-ion battery anode were conducted in Prof. Nicola Pinna's laboratory (Institut für Chemie & IRIS Adlershof at Humboldt-Universität zu Berlin). The preparation of the working electrodes involved a thorough mixture of active components, including anode material, conductive carbon black (Super P), and polyvinylidene fluoride (PVDF) acting as a binder. This mixture was combined in a specific weight ratio of 7:2:1 and dissolved in N-methyl-2-pyrrolidone (NMP) as the solvent. Subsequently, the resulting mixture was cast onto copper foil (coated with carbon) obtained from Goodfellow, UK, using a doctor blade apparatus. The cast slurry was dried in a vacuum oven at a temperature of 60 °C for 2 h. Following a cold-laminating treatment, the electrodes were precisely punched into circular shapes measuring 18 mm in diameter. These punched electrodes were further dried overnight under vacuum conditions at 120 °C using a Büchi glass oven. The mass loadings of active material at the anodes ranged between 1.0 and 1.2 mg/cm².

For the electrochemical investigations, CR2032-type coin cells were assembled within an argon-filled glovebox. Lithium metal foil was utilized as both counter and reference electrodes. The electrolyte consisted of 1 M lithium hexafluorophosphate ($LiPF_6$) solution prepared by combining ethylene carbonate, diethyl carbonate (DEC), and dimethyl carbonate (DMC) in equal volumes (1:1:1 ratio). The separation between the electrodes was achieved by employing a glass microfiber separator (Whatman).

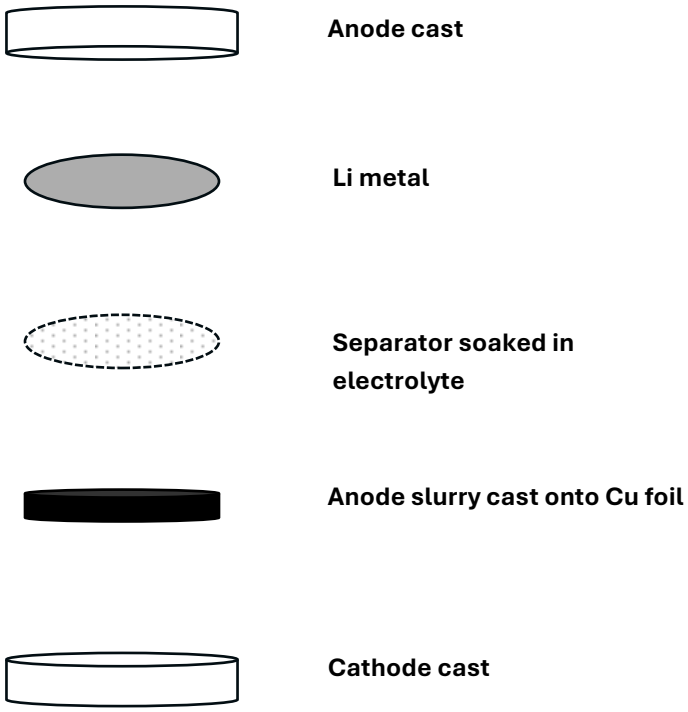

Figure 3.7 Schematic diagram of coin cell assembly for anode testing.

3.3 Green synthesis of WO_3 and their characterization

3.3.1 Synthesis method

WO_3 nanopowders were produced by precipitation method using various solutions, with tungsten (VI) chloride (WCl_6, Sigma-Aldrich) as the precursor material. Vitamin C from Sigma-Aldrich, and potassium sulfate from Fluka were used in the synthesis, with solutions prepared in distilled water (Carlo Erba Reagents) in three different compositions.

In the first solution, 1 g of WCl_6 was dissolved in 50 ml of distilled water (H_2O) and stirred for 5 h at room temperature. The second involved preparing an aqueous vitamin C solution, stirred for 20 min at room temperature, followed by dissolving WCl_6 in 50 ml of H_2O and stirring for 30 min. 1 M vitamin C solution was then added dropwise to the WCl_6/H_2O precursor solution until the pH reached 2, stirred for 5 and 24 h. Vitamin C acted as the green capping, reducing, and pH control agent. The third solution followed the second solution process, incorporating 0.8 M potassium sulfate instead of 1 M vitamin C as a structure-directing agent. Following preparation, the solutions settled for 2 h at room temperature, and the resulting precipitates were collected

through centrifugation. Subsequent washing with H_2O and ethanol removed salt ions and other side-products from the precipitates. The final powders were dried at room temperature for 24 h and then annealed at 450 °C for 2 h.

3.3.2 Characterization

The morphological characteristics of materials were investigated through high-resolution field-emission scanning electron microscopy (FESEM) using the MIRA3 FEG-SEM from TESCAN. Structural analysis was conducted via X-ray diffraction (XRD) using the Empyrean model from PANalytical, operating at 40 kV and 40 mA with a Cu-LFF source (λ=1.54 Å). The 2θ measurements covered Bragg's diffraction angles from 15° to 90°, employing a scan speed of 100 s and a step size of 0.013°.

Raman spectra were measured using a Jasco NRS-5100 confocal Raman microscope, featuring a diode laser with a wavelength of 785 nm and a grating of 600 l/mm, operating at a nominal power of 20 mW. An MPLFLN 100x objective focused the laser beam onto the sample with a 1 µm spot, and the backscattered signal was collected by a cooled (-69 °C) CCD camera. Measurements covered the range of 50−1800 cm^{-1}, with an effective power of 6.0 mW, 50 accumulations, an exposure value of 7 s, and a resolution of 2 cm^{-1}. Four spectral measurements were conducted for each synthesized material, and the spectra underwent processing (baseline correction and data smoothing) using the Spectra Manager™ software from Jasco.

ATR-IR spectra were obtained using the FTIR Vertex 70 interferometer (Bruker Optics, Ettlingen, Germany), equipped with an ATR crystal module (Bruker-Diamond single reflection crystal) featuring a single reflection diamond crystal at 45°, a thermal source (Globar), and a wide-range RT-DLaTGS detector. Measurements were performed under vacuum conditions. The ATR-IR spectra of WO_3 powder were acquired with an acquisition rate of 7.5 kHz in the spectral region of 50−6000 cm^{-1}, averaging 128 scans with a spectral resolution of 4 cm^{-1}. Second-derivative analyses were applied to both Raman and ATR-IR spectra using a 13-point smoothing filter [152]. Post-processing data analysis and visualization were carried out using OPUSTM 8.2 software (Bruker) and OriginPro™ 9.0, respectively.

3.3.3 Gas sensing measurement

The synthesized WO_3 powder was dispersed in water (H_2O) and sonicated for 10 minutes. The resulting dispersion was drop cast on alumina substrates using a dispenser. A substrate cut was made to reveal the thickness of the WO_3 nanostructure after the aqueous nanoparticle dispersion drop-casting (Figures 3.8a and b). The initially prepared materials underwent annealing at 450 °C to enhance their crystalline and electrical properties for high operating temperatures. Consequently, we selected 400 °C as the maximum temperature for the subsequent gas sensing studies.

Gas sensing measurements were carried out at 40% relative humidity (RH), with a flow rate of 300 sccm. These sensors were tested at different operating temperatures (250−400 °C) toward various concentrations of acetone, carbon monoxide (CO), carbon dioxide (CO_2), ammonia (NH_3), methane (CH_4), ethanol, and hydrogen (H_2). Each gas was injected into the chamber and maintained for 30 minutes, followed by a recovery period where the baseline was restored by flowing air for 85 minutes. Furthermore, the effect of humidity on gas sensing properties of materials was studied varying the concentration of RH in the test chamber from 40−90%.

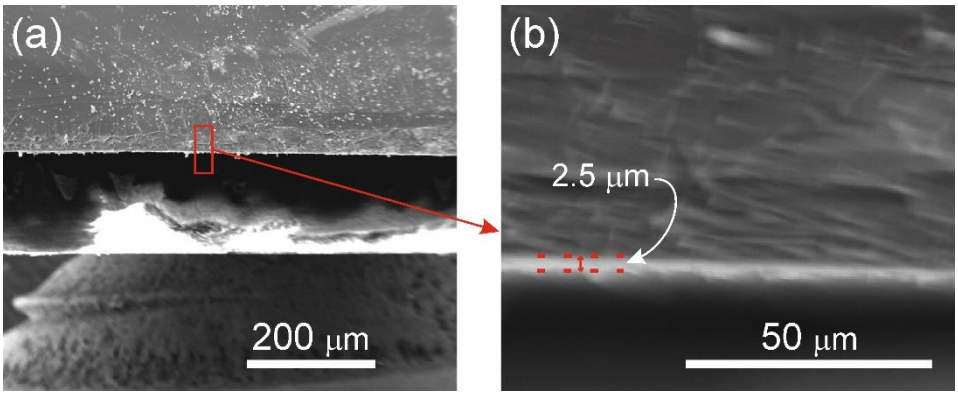

Figure 3.8 (a and b) Cross-section FESEM images of WO_3 nanostructure (after the drop-casing on the substrate) with different magnifications.

3.4 Chemical synthesis of WO_3 and their characterization

3.4.1 Synthesis method

WCl_6 (Sigma-Aldrich), benzyl alcohol (Sigma-Aldrich), and polyethylene glycol 200 (PEG 200, Sigma-Aldrich) were employed as reagents in the synthesis of materials. The preparation of WO_3 nanostructures involved two solutions: (i) Dissolving 1 g of WCl_6 in 50 ml of benzyl alcohol through 30 minutes of stirring at room temperature. (ii) Forming the second solution similarly, with the addition of 0.2 g of PEG 200 dropwise to the WCl_6 solution. Both solutions were then heated at 80 °C for 13 h. The resulting powders underwent multiple ethanol (Sigma-Aldrich) washes through centrifugation and were dried at room temperature. Finally, the precipitates were calcined at 450 °C for 2 h. The powder material prepared in the benzyl alcohol solution containing WCl_6 was designated as WO_3_P_1, while the one synthesized in the benzyl alcohol solution containing WCl_6 and PEG 200 was denoted as WO_3_P_2.

3.4.2 Characterization

Morphological analysis of the materials was conducted using field-emission scanning electron microscopy (FESEM, MIRA3 FEG-SEM, TESCAN) and transmission electron microscopy (TEM). Crystalline structure analysis was carried out through X-ray diffraction spectroscopy (XRD) and Raman spectroscopy.

Raman spectra were recorded on a Jasco NRS-5100 Confocal Raman Microscope, featuring a diode laser at 785 nm and a grating of 600 l/mm, operating at a nominal power of 20 mW. The laser beam is directed onto the sample with a spot size of 1 µm using an MPLFLN 100x objective. The backscattered signal is gathered using a CCD camera cooled to -69 °C. The measurements covered the range of 159–1890 nm, with an effective power of 6.0 mW. The number of accumulations was 50, the exposure value was 7 s, and the resolution was 3 cm^{-1}.

Four spectral measurements were performed for each material, and spectra were processed (baseline correction and data smoothing) with the Spectra Manager™ operating system

associated with the Jasco Raman instrument. The second derivative was calculated for identifying spectrum maxima positions.

Attenuated total reflectance (ATR) Fourier-transform infrared (IR) spectra were obtained using an FTIR Vertex70 interferometer (Bruker Optics, Ettlingen, Germany) equipped with a thermal source (Globar), an ATR crystal module (Bruker-Germanium Multiple reflection crystal) with a single reflection diamond crystal at 45°, and an RT-DLaTGS wide-range detector. The measurements were conducted under vacuum conditions. The infrared spectra of WO_3 nanomaterials were acquired with an acquisition rate of 7 kHz in the spectral region of 50–6000 cm^{-1}, averaging 128 scans collected with a spectral resolution of 4 cm^{-1}. Second-derivative analysis was performed using a 9-point smoothing filter [8]. ATR-IR data pre- and post-processing were carried out using OPUS^{TM} 8.2.

3.4.3 Gas sensing measurement

Gas sensing characterization of materials was conducted by drop-casting sensing materials on alumina substrates. First, Pt interdigitated electrical contacts and a Pt heater were deposited on substrates by DC magnetron sputtering technique (as mentioned the conditions in 3.2 gas sensing device fabrication section). Then, the fabricated WO_3 was dispersed in distilled water (H_2O) and dispersion was drop cast on the alumina substrates, followed by annealing at 450 °C for 72 h.

The gas sensing performance of WO_3_P_1 and WO_3_P_2 was analyzed at 250 to 400 °C and 40% RH. The gas sensing response of samples was studied toward different analytes including acetone, CO, CO_2, NH_3, CH_4, ethanol, and H_2. The RH level varied from 40−95% to investigate its influence on gas sensing performance. Sensors were exposed to gas flowing inside the chamber for 30 min and then, to recover the baseline, the airflow was restored for 85 min.

3.5 CuO-ZnO Composites preparation and their characterization

3.5.1 Preparation of CuO and ZnO structures

The CuO and ZnO powders were synthesized through the polyol method employing two distinct solutions:

(i) 0.05 g of copper acetate ($Cu(CH_3COO)_2$, Sigma-Aldrich) dissolved in 25 ml of ethylene glycol ($C_2H_6O_2$, Sigma-Aldrich) was stirred for 30 minutes at room temperature, followed by heating the solution at 150 °C for 40 minutes. The clear solution became cloudy after 20 minutes due to the formation of an organocopper precursor.

(ii) 2 g of zinc acetate ($Zn(CH_3COO)_2$, Sigma-Aldrich) was combined with 25 ml of ethylene glycol and stirred, and then the mixture was heated at 150 °C for 6 h.

The resulting powders were collected and washed with ethanol using centrifugation to eliminate side products. Subsequently, the particles were dried at 75 °C for 24 h and annealed at 500 °C for 2 h to obtain crystalline copper oxide and zinc oxide powders.

3.5.2 Synthesis of CuO-ZnO composite

For the preparation of the CuO-ZnO composite, 0.017 g of the acquired organocopper precursor was dissolved in 5 ml of isopropanol (C_3H_8O, Sigma Aldrich) and stirred at room temperature for 15 minutes. Then, 0.153 g of the previously prepared zinc oxide precursor was added to the mixture and stirred for additional 15 minutes to dissolve the ZnO precursor powder. The resulting solution underwent heating at 100 °C for 30 minutes, followed by three times centrifugation with ethanol at 3500 rpm to obtain the precipitate. The material was then dried at 75 °C for 24 h and calcined at 500 °C for 2 h.

To compare the gas sensingperformance of the composite with bare CuO and ZnO powders, two composite ratios were synthesized. These are denoted as CuO-ZnO_95 (Zn:Cu=0.95:0.05) and CuO-ZnO_90 (Zn:Cu=0.9:0.1).

3.5.3 Characterization

The high-resolution FESEM (MIRA3 FEG-SEM, TESCAN) was employed to observe the morphologies of the samples. Powder X-ray diffraction intensities were obtained using an X-ray diffractometer (Empyrean model, PANalytical, The Netherlands) operating at 40 kV and 40 mA, with a Cu-LFF (λ=1.54 Å) source. The 2θ (Bragg's diffraction angles) measurements covered a range from 20° to 90°, employing a scan speed of 100 s and a step size of 0.013° for comprehensive structural analysis. The optical properties of the material were determined by UV-vis spectrometer (UV-2600, Shimadzu, Kyoto, Japan). The absorption spectra were recorded with wavelength range starting from 800 to 250 nm and a sampling interval of 0.05 nm. The direct detector unit was used with slit width of 2 nm.

3.5.4 Gas sensing measurement

The synthesized CuO, ZnO and their composite were dispersed in isopropyl alcohol and drop cast onto alumina substrates by a Gilson dispenser (Figure 3.6). To investigate gas sensing properties of CuO, ZnO, CuO-ZnO_95 and CuO-ZnO_90, the fabricated sensors were tested toward different gases such as NO_2, acetone, CO_2, NH_3, CH_4, ethanol, and H_2 at operating temperature of 250 to 400 °C and 40% RH. Furthermore, the humidity effect was studied toward NO_2 at optimum operating temperature.

3.6 Synthesis of V_2O_5 and their characterization

3.6.1 Synthesis of V_2O_5 micro sheet

0.35 g of ammonium metavanadate (NH_4VO_3, Sigma-Aldrich) was dissolved into 50 ml of pure water (Carlo Erba Reagents), and 2 M nitric acid (HNO_3, Sigma-Aldrich) was added dropwise to the precursor solution until the pH reached 3. The solution was then heated at 60 °C for 5 h. The

resulting orangish solution was centrifuged and washed with distilled water and ethanol. The final powder was dried at room temperature for 24 h and annealed at 500 °C for 3 h to obtain crystalline V_2O_5 powders. During this process, different reaction temperatures (60, 80 °C) were investigated. The powder material prepared at a reaction temperature of 60 °C was labeled as V_2O_5_60, while the one synthesized at 80 °C was denoted as V_2O_5_80 in this study.

3.6.2 Characterization

High-resolution field-emission scanning electron microscopy (FESEM) with a MIRA3 FEG-SEM (TESCAN) was utilized to investigate the morphological characteristics of the fabricated materials. Structural properties were examined through X-ray diffraction (XRD) using an Empyrean model (PANalytical, The Netherlands) with a Cu-LFF (λ=1.54 Å) source operating at 40 kV and 40 mA. The 2θ (Bragg's diffraction angles) measurements covered a range from 15° to 90°, employing a scan speed of 100 s and a step size of 0.013° for comprehensive structural analysis. Images using transmission electron microscopy (TEM) and high-resolution TEM (HRTEM) were obtained utilizing a Philips CM 200 and an FEI Talos 200S microscope, operating at 200 kV.

3.6.3 Electrochemical measurement

To perform galvanostatic charge-discharge cycles, a CT2001 battery testing system was operated at room temperature. The potential range for these cycles was set at 0.01 to 3.0 V versus Li/Li^+ with specific currents ranging from 0.1 to 2 A/g. The CV was conducted in the potential range of 0.01 to 3.0 V versus Li/Li^+ at various scan rates (0.1 to 1 mV/s). Electrochemical impedance spectroscopy (EIS) was carried out at open circuit potential (OCP) in a half-cell configuration, sweeping frequencies from 100 kHz to 10 MHz with an amplitude of 10 mV.

Conclusion

In conclusion, this chapter reports the synthesis methods employed for metal oxide nanoparticles, with a particular focus on the sol-gel and polyol techniques. The intricate processes involved in sol-gel, from hydrolysis and condensation to aging, drying, and calcination, underscore its versatility in tailoring material properties. Additionally, the chapter described the instrumental setups for gas sensor fabrication, employing magnetron sputtering, and presented the gas sensing measurement procedures and parameters. It provided a comprehensive foundation for the subsequent chapters' exploration of specific metal oxide structures and their applications, detailing synthesis methods, device fabrication and characterization techniques.

References

[1] S.M. Gupta, M. Tripathi, A review on the synthesis of TiO_2 nanoparticles by solution route, Central European Journal of Chemistry, 10 (2012) 279-294.
[2] B.E. Yoldas, Monolithic glass formation by chemical polymerization, Journal of Materials Science, 14 (1979) 1843-1849.
[3] M. Niederberger, Nonaqueous Sol–Gel Routes to Metal Oxide Nanoparticles, Accounts of Chemical Research, 40 (2007) 793-800.
[4] H. Abdullah, A. Al-Amiery, S. Al-Baghdadi, The using of nanomaterials as catalysts for photodegradations, Journal of Physics: Conference Series, 1853 (2021) 012052.
[5] L. Poul, S. Ammar, N. Jouini, F. Fievet, F. Villain, Synthesis of Inorganic Compounds (Metal, Oxide and Hydroxide) in Polyol Medium: A Versatile Route Related to the Sol-Gel Process, Journal of Sol-Gel Science and Technology, 26 (2003) 261-265.
[6] P.J. Kelly, R.D. Arnell, Magnetron sputtering: a review of recent developments and applications, Vacuum, 56 (2000) 159-172.
[7] L.I. Company, Set up the battery test systems, 2020.
[8] F. Piccirilli, F. Tardani, A. D'Arco, G. Birarda, L. Vaccari, S. Sennato, S. Casciardi, S. Lupi, Infrared Nanospectroscopy Reveals DNA Structural Modifications upon Immobilization onto Clay Nanotubes, Nanomaterials, 11 (2021) 1103.
[9] V. Milman, B. Winkler, J. White, C. Pickard, M. Payne, E. Akhmatskaya, R. Nobes, Electronic structure, properties, and phase stability of inorganic crystals: A pseudopotential plane-wave study, International Journal of Quantum Chemistry, 77 (2000) 895-910.
[10] C. Adamo, V. Barone, Accurate excitation energies from time-dependent density functional theory: assessing the PBE0 model for organic free radicals, Chemical physics letters, 314 (1999) 152-157.
[11] J.P. Perdew, Y. Wang, Accurate and simple analytic representation of the electron-gas correlation energy, Physical review B, 45 (1992) 13244.
[12] H.J. Monkhorst, J.D. Pack, Special points for Brillouin-zone integrations, Physical review B, 13 (1976) 5188.

Chapter 4: Green Synthesis of WO_3 nanoparticle and their gas sensing performances

Introduction

Addressing the increasing need for green chemistry approaches, herein, a simple environmentally friendly and cost-effective method for the fabrication of WO_3 nanopowder using vitamin C as a surfactant was studied. The motivation behind this approach lies in addressing the challenges of minimizing hazardous substances and enhancing the efficiency of chemical processes, in line with the principles of green chemistry. The research explores the potential applications of the synthesized WO_3 in gas sensors, particularly demonstrating a high and selective response toward acetone molecules. It highlights its significance in eco-friendly technologies for nanomaterial synthesis and gas sensor fabrication.

4.1 Morphological properties

Figures 4.1 and 4.2 depict the FESEM images of WO_3 materials fabricated under different conditions: in H_2O, in aqueous solutions of vitamin C, and in potassium sulfate. In Figures 4.1a and b, the morphology of the WO_3 structure, prepared in a surfactant-free aqueous solution with a 5-hour reaction time, reveals particle agglomeration. Conversely, Figures 4.1c−e and Figure 4.2a display WO_3 nanoparticles with an average dimension of 52 nm when synthesized in a vitamin C-containing aqueous solution with the same reaction time. Figures 4.1f and g show the morphology of the material prepared in the aqueous solution of potassium sulfate, indicating particle agglomeration.

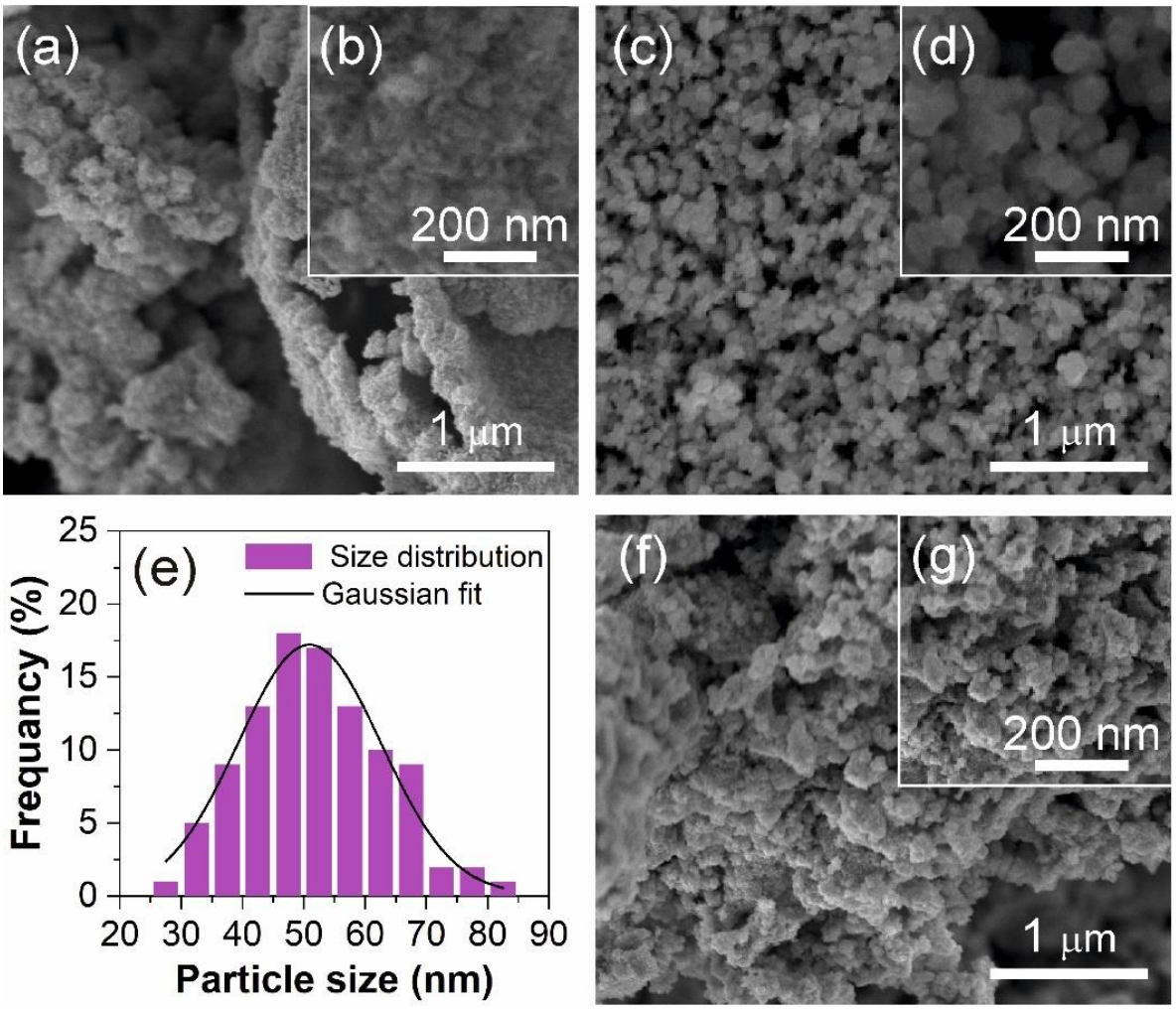

Figure 4.1 FESEM images of fabricated WO_3 powders: a) and b) Material synthesized in H_2O with a reaction time of 5 h, c) and d) WO_3 nanoparticles prepared in vitamin C-containing aqueous solution with a reaction time of 5 h, e) Particle size distribution histogram of WO_3 powder prepared in the aqueous solution of vitamin C with a reaction time of 5 h, f) and g) WO_3 material obtained in potassium sulfate-containing aqueous solutions with a reaction time of 5 h.

The agglomeration of WO_3 nanoparticles, prepared in H_2O, (Figures 4.1a and b) can be ascribed to the high reactivity of the tungsten precursor (WCl_6) and its rapid hydrolysis [1]. The morphological properties of the WO_3 structure, synthesized in an aqueous solution containing vitamin C, suggest that vitamin C acts as a mild reducing and capping agent, promoting uniform WO_3 particle growth without agglomeration [2, 3]. In this scenario, organic molecules attach to the growth surface, preventing nanoparticle agglomeration due to electrostatic or steric stabilization effects. Vitamin C significantly influences the formation and size of nanoparticles by

occupying available growth sites [4-8]. Moreover, the use of potassium sulfate as a capping agent has a partial impact on particle separation (Figures 4.1f and g), indicating the superior efficiency of the vitamin C-containing aqueous solution in WO_3 nanoparticle synthesis. The experiments are conducted at room temperature, reducing power consumption. The insufficient separation of particles in the potassium sulfate solution is attributed to weak capping interactions at low temperatures, enabling primary WO_3 nucleus formation without effective control of the growth mechanism by the capping agent (potassium sulfate) [9]. However, nanoparticle agglomeration occurs when the reaction time in the vitamin C solution is extended to 24 h (Figures 4.2b and c), which can be attributed to the self-assembly effect of the Ostwald ripening mechanism. This mechanism involves small particles dissolving in the solution and subsequently forming larger ones [10, 11]. Therefore, further analysis explores the crystalline, compositional, and gas sensing properties of WO_3 nanopowder synthesized in the aqueous solutions of vitamin C with a 5-hour reaction time (Figures 4.1c and d and Figure 4.2a). Additionally, vitamin C is considered a green agent, making the preparation of WO_3 nanopowder in its aqueous solution an environmentally friendly or green synthesis procedure, unlike previous methods that used less eco-friendly reagents such as hydrochloric acid, urea, oxalic acid, and sodium sulfate [12-14].

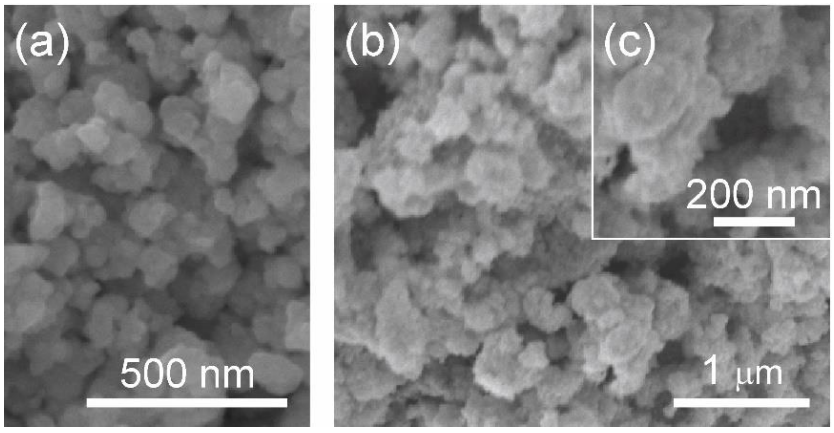

Figure 4.2 a) WO_3 nanoparticles prepared in the aqueous solution of vitamin C with a reaction time of 5 h, b) and c) WO_3 powder fabricated in vitamin C-containing aqueous solution with a reaction time of 24 h.

4.2 Structural properties

Figure 4.3a displays the XRD pattern of the WO_3 powder. The result indicates that the diffraction pattern of the material matches with the monoclinic phase (JCPDS no. 98-007-1692, space group: P 121/c 1, and space group number: 14). No other phases are evident in this pattern. The main peaks observed at 23.175, 23.653, 24.418, 28.843, 33.353, 34.277, 41.707, 50.088, 50.650, and 55.881 correspond to the (100), (020), (002), (11−1), (120), (02−2), (122), (210), (12−3), and (14−1) planes of monoclinic WO_3, respectively.

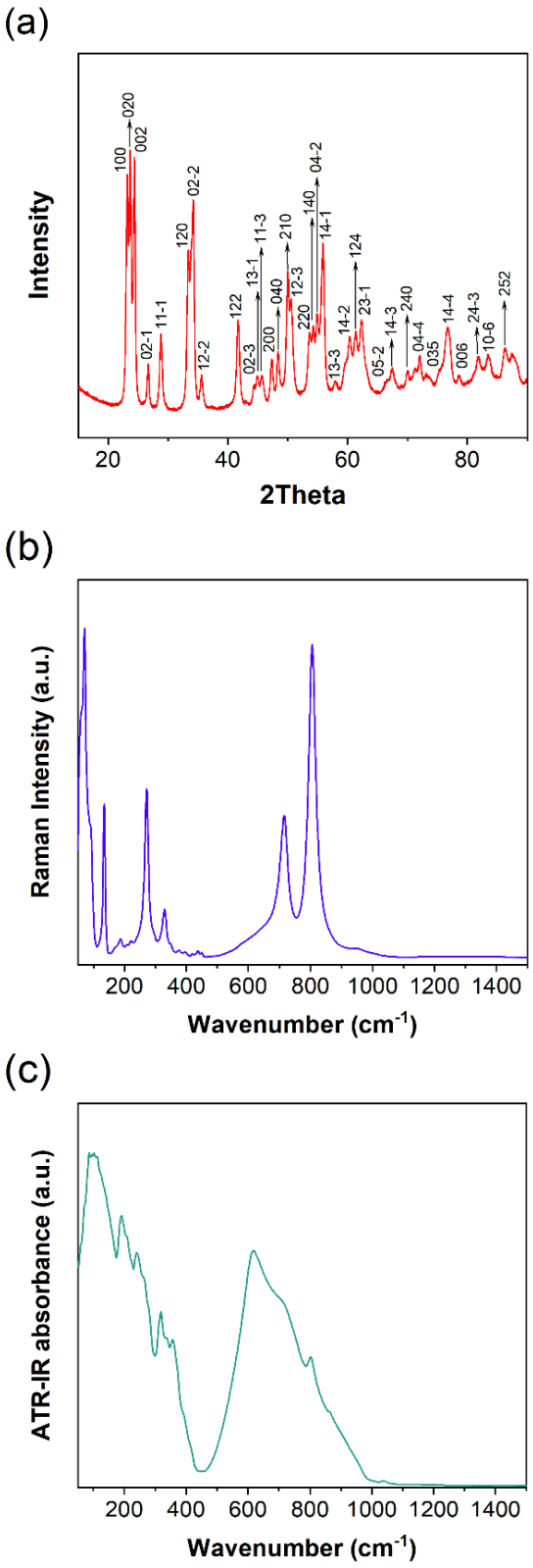

Figure 4.3 a) XRD pattern of the WO_3 nanopowder synthesized in the aqueous solution of vitamin C with a reaction time of 5 h, b) The Raman spectrum of WO_3 powder in the 50−1500

cm^{-1} spectral region. The whole Raman spectrum is reported in Figure 4.4a and c) ATR-IR spectrum of WO_3 in the spectral region between 50 and 1500 cm^{-1}. The whole ATR-IR spectrum is reported in Figure 4.4b.

The Raman spectrum for the WO_3 powder is presented in Figure 4.3b, and the corresponding peak positions and assignments can be found in Table 4.1 [15-18]. Each mode identified in the spectrum can be linked to either a crystalline phase or a hydration state. Our analysis primarily relies on comparisons with the comprehensive studies conducted by Pecquenard et al. [16] and Daniel et al. [15]. Generally, the Raman spectrum of WO_3 exhibits deformation lattice modes in the range of 200 to 400 cm^{-1}, stretching modes between 600 and 900 cm^{-1}, and the characteristic contribution of external terminal oxygen bonds W=O at approximately 950 cm^{-1} [15-18].

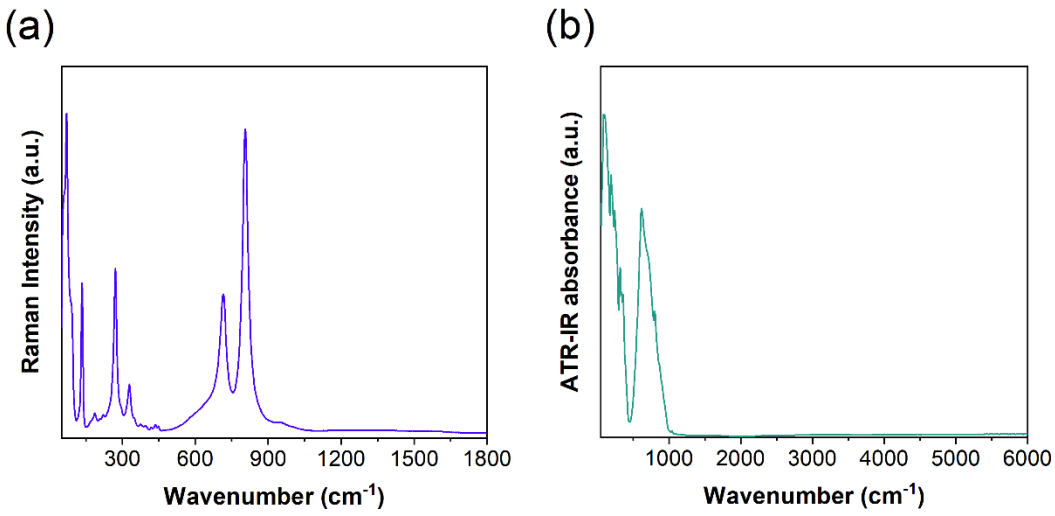

Figure 4.4 a) Raman spectrum of WO_3 powder in the spectral region of 50−1800 cm^{-1} and b) ATR-IR spectrum of WO_3 in the spectral region between 50 and 6000 cm^{-1}.

In the Raman spectrum of the WO_3 powder, intense resonances are evident at 59, 71, 92, 134, 271, 329, 714, and 805 cm^{-1}. The peak at 71 cm^{-1} and the intense shoulders at 59 and 92 cm^{-1} are attributed to vibrations of $(W_2O_2)_n$ chains within the WO_3 lattice, indicative of the monoclinic structure [16, 17]. The peak at around 270 cm^{-1} is associated with O–W–O bending modes, representing the binding oxygen in WO_3 [18]. The weak peak at 188 cm^{-1} is linked to lattice modes characteristic of the monoclinic structure [15]. The sharp bands at 805 cm^{-1} and

714 cm^{-1} correspond to the stretching vibration of O–W–O and match with the mode of monoclinic WO_3 [15]. The WO_3 powder is synthesized using vitamin C ($C_6H_8O_6$) as a capping agent and H_2O as a solvent. However, no residual vitamin C content is observed in its Raman spectrum. Considering the Raman peak assignments, the presence of bands at 59, 71, 92, 133, 188, 221, 270, 329, 436, 714, and 805 cm^{-1} indicates that the fabricated powder is predominantly crystallized in the monoclinic phase of WO_3. However, weak shoulders are observed at high frequencies (between 940 cm^{-1} and 960 cm^{-1}) and at low frequencies (at 207 and 375 cm^{-1}), suggesting the potential presence of a small amount of hydrates.

Table 4.1 Raman peak/band positions and chemical group assignment of the fabricated WO_3 powder [15, 19, 20].

Frequency position cm^{-1}	**Assignment**
59	ν (W_2O_2)
71	ν(W_2O_2)
92	ν (W_2O_2) Lattice mode
133	Lattice mode
170	–
188	Lattice mode
207	ν (W–O–W)
221	ν (W–O–W)
270	δ (O–W–O)
329	δ (O–W–O) ν (W–OH_2)
375	ν (W–OH_2)

395	//weak shoulder
436	ν ($W–OH_2$)
714	ν (O–W–O)
805	ν (O–W–O)
954	ν (W=O)

Figure 4.3c displays the ATR-IR spectrum of the synthesized WO_3 powder, with detailed peak positions and assignments provided in Table 4.2. In the far-IR region, the spectrum exhibits intense and visible broad bands at approximately 100 and 189 cm^{-1}, attributed to the lattice modes of W-oxides. Additionally, main IR bands in the very low-frequency range (around 160, 140, 130, and 110 cm^{-1}) are associated with lattice modes of WO_3. Three bands at 242, 317, and around 338 cm^{-1} correspond to the vibration modes of W−O−W [15, 20-22]. The IR bands within the 318–360 cm^{-1} range correspond to the W–O–W vibration of WO_3. A shoulder is evident at 394 cm^{-1}, attributed to the bending modes of water molecules ($W–OH_2$) [20, 22]. In the mid-IR spectral region, there is a noticeable and intense broad band. Its primary sharp peak at 616 cm^{-1} and two shoulders around 730 and 757 cm^{-1} can be related to (W−O) vibrational stretching modes [20, 22]. Two additional shoulders, identified through 2^{nd} derivative analysis, appear around 867 and 954 cm^{-1} and are designated as stretching modes of (O−W−O) and (W=O), respectively [21, 23].

Moreover, the ATR-IR spectrum of the WO_3 powder revealed a very weak band at approximately 1617 cm^{-1} within the bending region associated with H_2O molecules, suggesting a potential connection to the water content in the material [20].

The existence of main bands at 282, 338, 638, 736, 757, and 867 cm^{-1} are attributed to the monoclinic WO_3 phase [15, 19, 20], consistent with the findings from Raman measurements.

Table 4.2 Infrared peak/band positions and assignments of WO_3 powder [15, 20-24].

Frequency position (cm^{-1})	Assignment
50	lattice modes
85	lattice modes
100	lattice modes
110	lattice modes
131	–
140	lattice modes
160	lattice modes
189	lattice modes
211	lattice modes
242	ν(W–O–W)
265	ν(W–O–W)
282	δ(O–W–O)
317	ν(W–O–W)
338	ν(W–O–W)
358	ν(W–OH_2)
394	δ(W–OH_2)
417	δ(W–O)
614	–
638	ν(W–O)
726	ν(W–O)
757	ν(O–W–O)
804	
867	ν(O–W–O)
954	ν(W=O)
1012	–
1039	δ(W–OH)
1617	δ (OH)

4.3 Gas sensing results

Figure 4.5a illustrates the sensing response of the WO_3 nanostructure toward 10 ppm of acetone at various working temperatures (ranging from 200 to 400 °C) and 40% relative humidity (RH). Notably, the material's response shows an upward trend with increasing operating temperature, reaching its peak at 400 °C. In Figure 4.5b, the dynamic gas sensing characteristics of the WO_3 sensor at its optimal operating temperature (400 °C) are exhibited. The sensor's electrical conductance increases with the injection of each concentration of acetone into the test chamber and returns to baseline after purifying the chamber with synthetic airflow. Upon exposure to air, environmental oxygen adsorbs on the material's surface, trapping electrons from the conduction band and leading to the formation of oxygen ions (Equations 1–4) [25, 26].

$$O_2(gas) \leftrightarrow O_2(ads) \quad (1)$$

$$O_2(ads) + e^- \leftrightarrow O_2^-(ads) \quad (2)$$

$$O_2^-(ads) + e^- \leftrightarrow 2O^-(ads) \quad (3)$$

$$O^-(ads) + e^- \leftrightarrow 2O^{2-}(ads) \quad (4)$$

When the sensing material is exposed to a reducing volatile organic compound like acetone, the oxygen species adsorbed on its surface interact with the acetone molecules (Equation 5). Consequently, the electrons previously trapped are released back to the material's conduction band [27-29]. Therefore, the adsorbed acetone acts as an electron donor, leading to an increase in the sensor's conductance.

$$CH_3COCH_3(gas) + 8O^- \rightarrow 3CO_2 + 3H_2O + 8e^- \quad (5)$$

Moreover, the observed changes in sensor conductance resulting from exposure to acetone and subsequent purification of the test chamber explain the reversible interaction between acetone and the nanostructure, confirming the n-type behavior of WO_3 [30]. The efficiency of environmental oxygen adsorption on the WO_3 surface is diminished at lower operating temperatures, potentially affecting the interaction and charge carrier exchange between

acetone molecules and the material surface [31, 32]. Additionally, the chemisorption of complex organic molecules of acetone on oxide material involves high activation energy and multi-step reactions with the sensing structure [33, 34]. Hence, the response of the prepared WO_3 sensor toward acetone is notably influenced by its operating temperature, with the optimal response observed at 400 °C (Figure 4.5a).

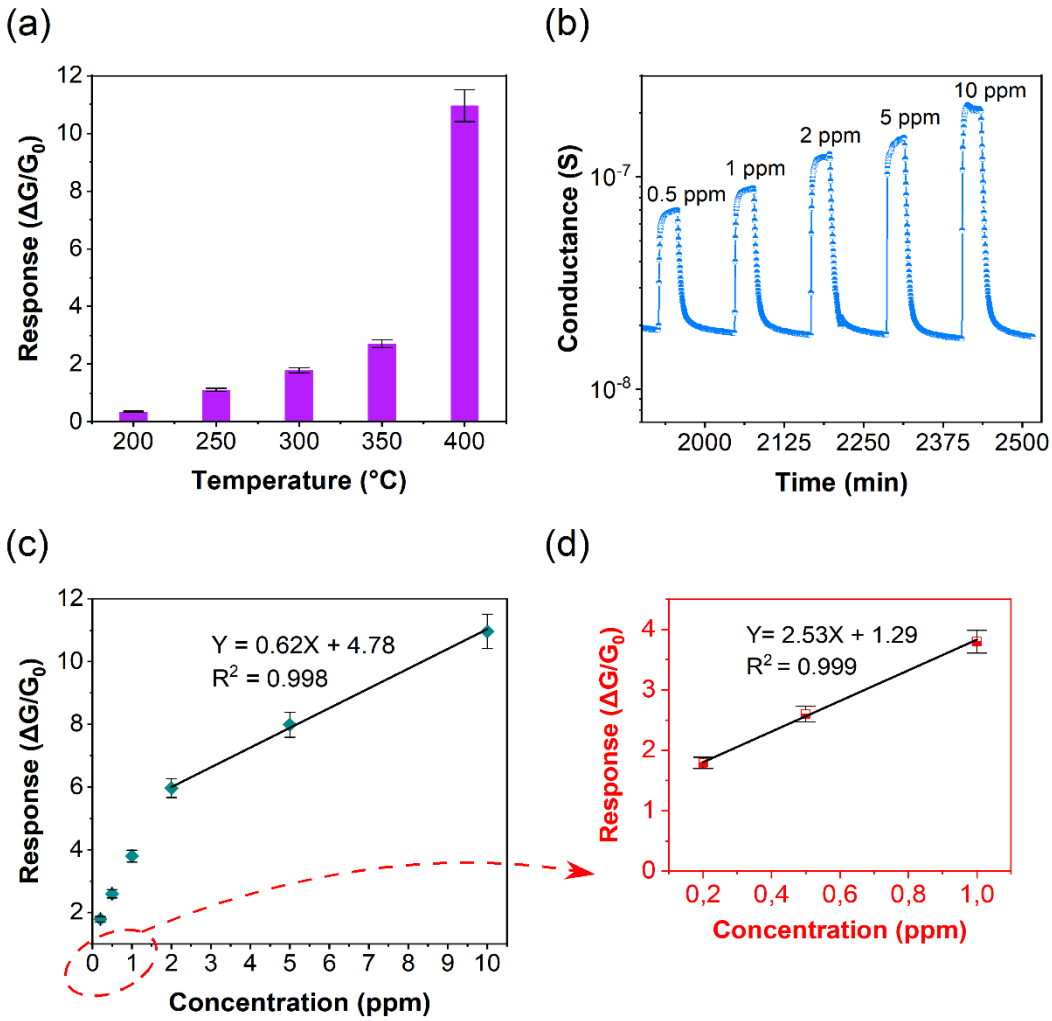

Figure 4.5 a) Acetone sensing response of WO_3 nanomaterial at different temperatures, b) Dynamic response of the WO_3 gas sensor toward acetone (0.5, 1, 2, 5, and 10 ppm) at 400 °C (RH, 40 %), c) Response of WO_3 toward different concentrations of acetone (0.2−10 ppm) at an operating temperature of 400 °C and d) A magnified section from Figure c where the response of the material toward low concentrations of acetone (from 200 ppb to 1 ppm) can be seen.

The concentration of acetone (0.2−10 ppm) affects the response of WO_3, as shown in Figures 4.5c and d. The results are summarized in Table 4.3. Two linear regions can be observed, with a

higher sensitivity at low concentrations (0.2−1 ppm) compared to higher concentrations (2−10 ppm). By applying curve-fitting analysis using linear regression, it can be observed that the slope in the lower concentration range (0.2−1 ppm) is 2.53, exceeding the slope of 0.62 found in the higher concentration range (2−10 ppm). The high response toward low concentrations of acetone is a significant achievement because breath acetone levels for healthy individuals are below 1.8 ppm, while diabetics have higher concentrations [35, 36]. Therefore, the fabricated material shows its promising applications for medical diagnostics and environmental monitoring.

Table 4.3 Sensing properties of prepared WO_3 nanoparticles toward different concentrations of acetone at an operating temperature of 400 °C.

Acetone concentration (ppm)	Response
0.2	1.8
0.5	2.6
1	3.8
2	6
5	8
10	11

To assess their practical application, it is important to examine the properties of chemiresistive sensing structures under varying humidity levels. Therefore, we investigated the performance of the WO_3 nanostructure by increasing the concentration of RH in the test chamber. In Figure 4.6a, the electrical conductance and sensing response of the material with increasing RH concentration are displayed. From 40% to 60% RH, there is minimal change in the conductance of WO_3. However, a slight increase of 14% is observed at 80% and 90% RH. The structure exhibits good stability in electrical conductance at different RH levels, which can be attributed to the improved desorption of water molecules at a temperature of 400 °C [25, 26]. The sensor's response decreases by 17% as the relative humidity (RH) gradually increases from 40% to 90% in the test chamber. Consequently, the presence of water adsorption on WO_3 and the

hydroxylation of its surface partially impact the electrical conductance of the sensor and its interaction with analyte molecules. However, the interaction between water and acetone adsorption on the WO_3 surface is a complex process. In this scenario, the adsorbed water molecules may influence the formation and number of oxidized species involved in the adsorption of acetone [26, 27]. Meanwhile, the response of the sensor may also be partially affected by the ionization of water molecules on the material's surface [37]. Therefore, the small change observed in the sensing response of WO_3 with the RH concentration can be ascribed to the processes mentioned above.

The ability of a sensing material to detect specific gases is a crucial characteristic. Thus, we examined the selectivity of the WO_3 sensor towards various compounds such as carbon monoxide (CO), carbon dioxide (CO_2), ammonia (NH_3), methane (CH_4), ethanol, and hydrogen (H_2). The results (shown in Figure 4.6b) indicate that the structure has low sensitivity to CO, CO_2, CH_4, and H_2. Additionally, its response toward 20 ppm NH_3 (response value: 1.5) and 10 ppm ethanol (response value: 2.1) is significantly lower compared to 10 ppm acetone (response value: 11). Hence, the prepared WO_3 material demonstrates excellent selectivity toward acetone. The monoclinic WO_3 nanostructure (Figure 4.3) exhibits a strong interaction with the polar molecules of acetone due to its surface acidity and large dipole moment [38-40]. The improved response of the sensor toward acetone can potentially be attributed to this factor. On the other hand, the hexagonal WO_3 structure displays a higher affinity for adsorbing CO and CH_4 gases [41, 42]. CO_2 is a linear molecule with a dipole moment of zero [43]. The weak interaction between monoclinic WO_3 and CO_2 can be related to this characteristic [44]. NH_3 and ethanol possess smaller dipole moments [45, 46]. Studies have indicated that monoclinic WO_3 exhibits a more favorable interaction with acetone compared to ethanol, primarily due to its surface acidity [47]. Moreover, the superior response of monoclinic WO_3 to acetone, in comparison to ethanol, NH_3, and H_2, may be related to variations in the adsorption and desorption rates between the material and these analyte molecules [48, 49].

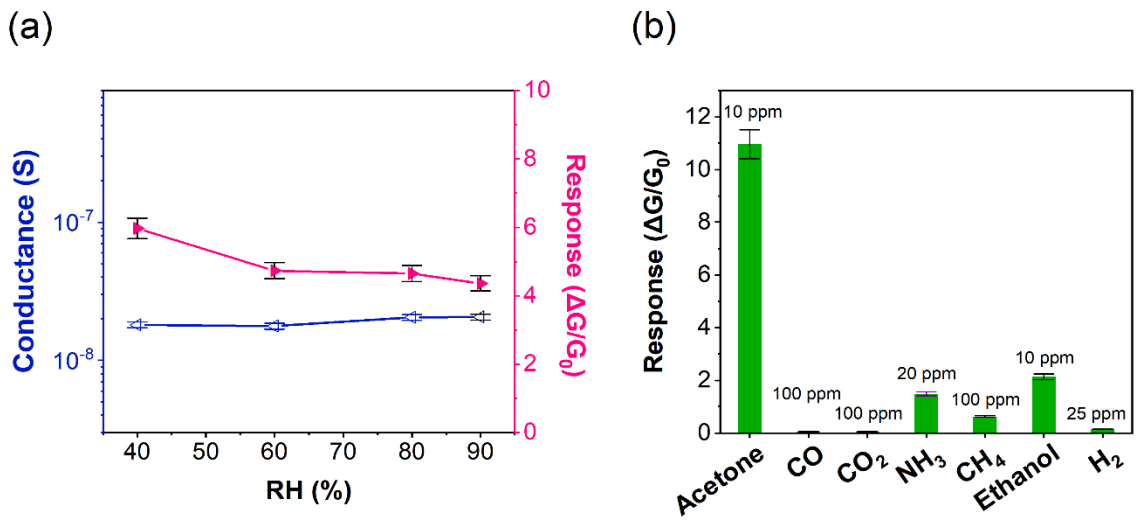

Figure 4.6 a) The variation of the conductance and response values (toward 2 ppm of acetone) of WO_3 depending on the concentration of RH (40–90%) in the test chamber and b) Response of WO_3 to acetone, CO, CO_2, NH_3, CH_4, ethanol, and H_2 at 400 °C.

Table 4.4 provides a comparison of acetone sensing parameters for the fabricated WO_3 nanoparticles with other metal oxide-based nanostructures. Comparing sensing structures is challenging due to variations in experimental setups and test protocols. Nevertheless, it is noteworthy that the developed WO_3 nanostructure exhibits a favorable and selective response to acetone without the need for dopants, noble metal catalytic layers, or other surface additives (Table 4.4). Therefore, our results and the comparison with other metal oxide-based acetone sensors suggest that monoclinic WO_3 particles, with their surface acidity and nano dimensions, are well-suited for efficient acetone molecule detection. Furthermore, sensing tests conducted after 2 months indicate that the WO_3 material maintains stable functional performance for acetone detection (Figures 4.7a and b). Hence, these findings are significant for the environmentally friendly synthesis of WO_3 nanomaterials and their application in acetone sensing devices.

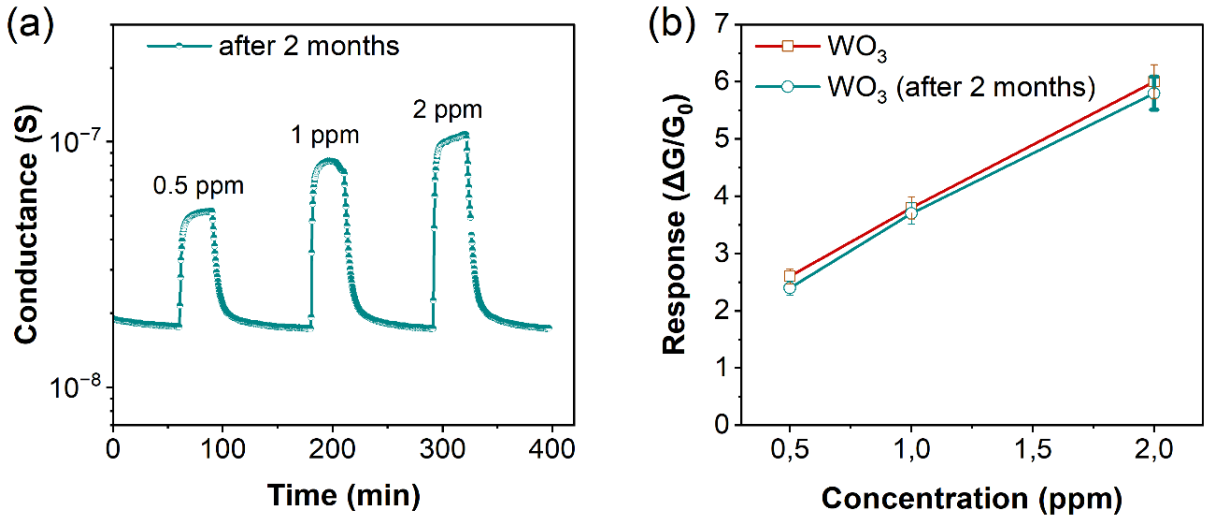

Figure 4.7 a) Dynamic response of the WO_3 gas sensor toward acetone (0.5, 1, and 2 ppm) at 400 °C (RH, 40%) obtained two months after the first-time measurements and b) The response of WO_3 toward 0.5, 1, and 2 ppm of acetone at 400 °C. The results were obtained after the first-time measurements and two months later.

Table 4.4 Acetone sensing properties of metal oxide structures.

Sensing materials	Synthesis method	Operating temperature (°C)	Concentration (ppm)	Response	Ref.
Co_2O_3 microsphere	Precipitation	180	100	7.6 (R_f/R_0)	[50]
Ag-WO_3 nanosheets	Precipitation	340	50	8 (R_0/R_f)	[51]
ZnO nanoflower	Precipitation	219	100	12.3 (R_0/R_f)	[52]
WO_3 nanoplate	Precipitation	260	100	30 (R_0/R_f)	[53]
$ZnFe_2O_4$/ZnO microflowers	Precipitation	250	50	8.3 (R_0/R_f)	[54]
ZnO/Co_3O_4 hollow polyhedrons	Precipitation	300	100	30 (R_0/R_f)	[55]
2.2 mol% Mn–ZnO nanoparticles	Precipitation	340	20	17 (R_0/R_f)	[56]
$BiFeO_3$ nanoparticles	Precipitation	350	1	1.8 (R_f/R_0)	[57]
ZnO nanorods	Precipitation	17	100	12.9 (R_0/R_f)	[58]
Co_3O_4 nanorods	Precipitation	240	100	5.6 (R_f/R_0)	[59]
Fe doped rGO decorated WO_3	Sol-gel	130	10	4.678 (R_0/R_f)	[60]
GO-WO_3 nanofibers	Electrospinning	375	100	35.9 (R_0/R_f)	[61]
Cactus-like WO_3-SnO_2	Hydrothermal	360	100	12.1 (R_0/R_f)	[62]
Au@ZnO yolk-shell nanospheres	Hydrothermal	300	100	37 (R_0/R_f)	[63]
WO_3 nanoparticles	Precipitation	400	10	11 (G_f-G_0)/G_0	This work

WO_3 nanoparticles	Precipitation	350	10	2.7 $(G_f-G_0)/G_0$	This work
WO_3 nanoparticles	Precipitation	300	10	1.8 $(G_f-G_0)/G_0$	This work
WO_3 nanoparticles	Precipitation	250	10	1.1 $(G_f-G_0)/G_0$	This work

Conclusion

WO_3 nanoparticles were successfully synthesized using an environmentally friendly and low-cost precipitation method with H_2O as the solvent and vitamin C as a surfactant. Vitamin C acted as a mild reducing and capping agent, preventing agglomeration and resulting in WO_3 nanoparticles. The synthesized monoclinic WO_3 demonstrated high sensitivity toward acetone, making it promising for applications in gas sensors, particularly for medical diagnostics and environmental monitoring. The study highlights the significance of green synthesis methods in the synthesis of WO_3 nanomaterials with enhanced sensing properties.

Reference

[1] X.-L. Li, T.-J. Lou, X.-M. Sun, Y.-D. Li, Highly Sensitive WO_3 Hollow-Sphere Gas Sensors, Inorganic Chemistry, 43 (2004) 5442-5449.
[2] J. Xiong, Y. Wang, Q. Xue, X. Wu, Synthesis of highly stable dispersions of nanosized copper particles using l-ascorbic acid, Green Chemistry, 13 (2011) 900-904.
[3] N.D. Meeks, V. Smuleac, C. Stevens, D. Bhattacharyya, Iron-Based Nanoparticles for Toxic Organic Degradation: Silica Platform and Green Synthesis, Industrial & Engineering Chemistry Research, 51 (2012) 9581-9590.
[4] F. Ahangaran, A.H. Navarchian, Recent advances in chemical surface modification of metal oxide nanoparticles with silane coupling agents: A review, Adv Colloid Interface Sci, 286 (2020) 102298.
[5] C. Gutiérrez-Wing, J.J. Velázquez-Salazar, M. José-Yacamán, Procedures for the Synthesis and Capping of Metal Nanoparticles, in: M. Soloviev (Ed.) Nanoparticles in Biology and Medicine: Methods and Protocols, Humana Press, Totowa, NJ, 2012, pp. 3-19.
[6] R. Javed, M. Zia, S. Naz, S.O. Aisida, N.u. Ain, Q. Ao, Role of capping agents in the application of nanoparticles in biomedicine and environmental remediation: recent trends and future prospects, Journal of Nanobiotechnology, 18 (2020) 172.
[7] R.B. Grubbs, Roles of Polymer Ligands in Nanoparticle Stabilization, Polymer Reviews, 47 (2007) 197-215.

[8] B. Faure, G. Salazar-Alvarez, A. Ahniyaz, I. Villaluenga, G. Berriozabal, Y.R. De Miguel, L. Bergström, Dispersion and surface functionalization of oxide nanoparticles for transparent photocatalytic and UV-protecting coatings and sunscreens, Sci Technol Adv Mater, 14 (2013) 023001.
[9] Y. Zhang, W. Zeng, Y. Li, NO_2 and H_2 sensing properties for urchin-like hexagonal WO_3 based on experimental and first-principle investigations, Ceramics International, 45 (2019) 6043-6050.
[10] A. Yan, C. Xie, D. Zeng, S. Cai, M. Hu, Synthesis, formation mechanism and sensing properties of WO_3 hydrate nanowire netted-spheres, Materials Research Bulletin, 45 (2010) 1541-1547.
[11] F. Wang, V.N. Richards, S.P. Shields, W.E. Buhro, Kinetics and Mechanisms of Aggregative Nanocrystal Growth, Chemistry of Materials, 26 (2014) 5-21.
[12] W. Li, P. Da, Y. Zhang, Y. Wang, X. Lin, X. Gong, G. Zheng, WO_3 Nanoflakes for Enhanced Photoelectrochemical Conversion, ACS Nano, 8 (2014) 11770-11777.
[13] Y. Zhang, Y. Wang, L. Zhu, R. Zhang, J. Cao, Enhanced CO sensing performance of WO_3 nanorods with PtAg nanoparticles modification: A combined experimental and first-principle study, Vacuum, 193 (2021) 110526.
[14] S. Ansari, M.S. Ansari, S.P. Satsangee, R. Jain, WO_3 decorated graphene nanocomposite based electrochemical sensor: A prospect for the detection of anti-anginal drug, Analytica Chimica Acta, 1046 (2019) 99-109.
[15] M. Daniel, B. Desbat, J. Lassegues, B. Gerand, M. Figlarz, Infrared and Raman study of WO_3 tungsten trioxides and WO_3, xH_2O tungsten trioxide tydrates, Journal of solid state chemistry, 67 (1987) 235-247.
[16] B. Pecquenard, H. Lecacheux, J. Livage, C. Julien, Orthorhombic WO_3 Formed via a Ti-Stabilized $WO_3{\cdot}13H_2O$ Phase, Journal of Solid State Chemistry, 135 (1998) 159-168.
[17] Y. Djaoued, S. Balaji, R. Brüning, Electrochromic Devices Based on Porous Tungsten Oxide Thin Films, Journal of Nanomaterials, 2012 (2012) 674168.
[18] M.H. Mirfasih, C. Li, A. Tayyebi, Q. Cao, J. Yu, J.-J. Delaunay, Oxygen-vacancy-induced photoelectrochemical water oxidation by platelike tungsten oxide photoanodes prepared under acid-mediated hydrothermal treatment conditions, RSC Advances, 7 (2017) 26992-27000.
[19] G. Fulton, A. Lunev, Probing the correlation between phase evolution and growth kinetics in the oxide layers of tungsten using Raman spectroscopy and EBSD, Corrosion Science, 162 (2020) 108221.
[20] G.N. Kustova, Y.A. Chesalov, L.M. Plyasova, I.Y. Molina, A.I. Nizovskii, Vibrational spectra of $WO_3{\cdot}nH_2O$ and WO_3 polymorphs, Vibrational Spectroscopy, 55 (2011) 235-240.
[21] C. Balázsi, M. Farkas-Jahnke, I. Kotsis, L. Petrás, J. Pfeifer, The observation of cubic tungsten trioxide at high-temperature dehydration of tungstic acid hydrate, Solid State Ionics, 141-142 (2001) 411-416.
[22] M. Gotić, M. Ivanda, S. Popović, S. Musić, Synthesis of tungsten trioxide hydrates and their structural properties, Materials Science and Engineering: B, 77 (2000) 193-201.
[23] F.S. Tehrani, Hydrothermal synthesis and characterization of WO_3 nanostructures: Effect of reaction time, Materials Research Express, 7 (2020).
[24] J.D.-G. DIAZ-REYES, V. PEREZ-BENITEZ, A. y BALDERAS-LOPEZ, J. A., Obtaining films of tungsten trioxide (WO_3) by resistive heating of a tungsten filament, Superf. vacío, 21 (2008) 12-17.
[25] M.J. Madou, S.R. Morrison, 10 - Thin-Film Gas Sensors, in: M.J. Madou, S.R. Morrison (Eds.) Chemical Sensing with Solid State Devices, Academic Press, San Diego, 1989, pp. 419-435.
[26] M.J. Madou, S.R. Morrison, 3 - Solid/Gas Interfaces, in: M.J. Madou, S.R. Morrison (Eds.) Chemical Sensing with Solid State Devices, Academic Press, San Diego, 1989, pp. 67-104.
[27] M. Karmakar, B. Mondal, M. Pal, K. Mukherjee, Acetone and ethanol sensing of barium hexaferrite particles: A case study considering the possibilities of non-conventional hexaferrite sensor, Sensors and Actuators B: Chemical, 190 (2014) 627-633.
[28] Q. Wang, X. Cheng, Y. Wang, Y. Yang, Q. Su, J. Li, B. An, Y. Luo, Z. Wu, E. Xie, Sea urchins-like WO_3 as a material for resistive acetone gas sensors, Sensors and Actuators B: Chemical, 355 (2022) 131262.

[29] X. Zhang, B. Dong, W. Liu, X. Zhou, M. Liu, X. Sun, J. Lv, L. Zhang, W. Xu, X. Bai, L. Xu, S. Mintova, H. Song, Highly sensitive and selective acetone sensor based on three-dimensional ordered WO_3/Au nanocomposite with enhanced performance, Sensors and Actuators B: Chemical, 320 (2020) 128405.
[30] W. Zhang, Y. Fan, T. Yuan, B. Lu, Y. Liu, Z. Li, G. Li, Z. Cheng, J. Xu, Ultrafine Tungsten Oxide Nanowires: Synthesis and Highly Selective Acetone Sensing and Mechanism Analysis, ACS Applied Materials & Interfaces, 12 (2020) 3755-3763.
[31] X. Chang, S. Xu, S. Liu, N. Wang, S. Sun, X. Zhu, J. Li, O. Ola, Y. Zhu, Highly sensitive acetone sensor based on WO_3 nanosheets derived from WS_2 nanoparticles with inorganic fullerene-like structures, Sensors and Actuators B: Chemical, 343 (2021) 130135.
[32] M.R. Adib, V.V. Kondalkar, K. Lee, Development of Highly Sensitive Ethane Gas Sensor Based on 3D WO_3 Nanocone Structure Integrated with Low-Powered In-Plane Microheater and Temperature Sensor, Advanced Materials Technologies, 5 (2020) 2000009.
[33] S. Americo, E. Pargoletti, R. Soave, F. Cargnoni, M.I. Trioni, G.L. Chiarello, G. Cerrato, G. Cappelletti, Unveiling the acetone sensing mechanism by WO_3 chemiresistors through a joint theory-experiment approach, Electrochimica Acta, 371 (2021) 137611.
[34] S. Zeb, G. Sun, Y. Nie, Y. Cui, X. Jiang, Synthesis of highly oriented WO_3 nanowire bundles decorated with Au for gas sensing application, Sensors and Actuators B: Chemical, 321 (2020) 128439.
[35] R.I. Guzman-Avilan, S.N. González- Diaz, A.A. Cruz, A. Macias-Weinmann, B.E. Villarreal, C. Macouzet-Sanchez, R.V. Villarreal-Gonzalez, C.E.d. Lira-Quezada, K.G. Avilan, D. Sanchez-Guerra, Comparison Of Exhaled Breath Fraction Temperature (frEBT) In Patients With Respiratory Allergy, Journal of Allergy and Clinical Immunology, 141 (2018) AB98.
[36] H. Schwoebel, R. Schubert, M. Sklorz, S. Kischkel, R. Zimmermann, J.K. Schubert, W. Miekisch, Phase-resolved real-time breath analysis during exercise by means of smart processing of PTR-MS data, Analytical and Bioanalytical Chemistry, 401 (2011) 2079.
[37] N. Agmon, The Grotthuss mechanism, Chemical Physics Letters, 244 (1995) 456-462.
[38] H. Yang, H. Sun, Q. Li, P. Li, K. Song, B. Song, L. Wang, Structural, electronic, optical and lattice dynamic properties of the different WO_3 phases: First-principle calculation, Vacuum, 164 (2019) 411-420.
[39] P.M. Woodward, A.W. Sleight, T. Vogt, Ferroelectric Tungsten Trioxide, Journal of Solid State Chemistry, 131 (1997) 9-17.
[40] G.M. Maksimov, G.S. Litvak, A.A. Budneva, E.A. Paukshtis, A.N. Salanov, V.A. Likholobov, WO_3/MO_2 (M = Zr, Sn, Ti) heterogeneous acid catalysts: Synthesis, study, and use in cumene hydroperoxide decomposition, Kinetics and Catalysis, 47 (2006) 564-571.
[41] R. Wu, F. Tian, Z. Liu, X. Xue, J. Zhang, J. Zu, CH_4 activation and sensing on hexagonal WO_3 (001) and (110) surfaces, Applied Surface Science, 481 (2019) 1154-1159.
[42] F. Tian, L. Zhao, X.-Y. Xue, Y. Shen, X. Jia, S. Chen, Z. Wang, DFT study of CO sensing mechanism on hexagonal WO_3 (001) surface: The role of oxygen vacancy, Applied Surface Science, 311 (2014) 362-368.
[43] J.S. Muenter, R. Bhattacharjee, The Electric Dipole Moment of the CO_2–CO van der Waals Complex, Journal of Molecular Spectroscopy, 190 (1998) 290-293.
[44] Y. Lin, G. Huang, L. Chen, J. Zhang, L. Liu, Enhanced CO_2 Photoreduction by $Ni(OH)_2$-x/WO_3 Nanofibers with Efficient CO_2 Activation and Charge Separation, Advanced Sustainable Systems, 7 (2023) 2200364.
[45] P. Pracna, V. Špirko, W.P. Kraemer, Electric dipole moment function of ammonia, Journal of Molecular Spectroscopy, 136 (1989) 317-332.
[46] B. Li, G. Sauvé, M.C. Iovu, M. Jeffries-El, R. Zhang, J. Cooper, S. Santhanam, L. Schultz, J.C. Revelli, A.G. Kusne, T. Kowalewski, J.L. Snyder, L.E. Weiss, G.K. Fedder, R.D. McCullough, D.N. Lambeth, Volatile Organic Compound Detection Using Nanostructured Copolymers, Nano Letters, 6 (2006) 1598-1602.

[47] J. Kaur, K. Anand, A. Kaur, R.C. Singh, Sensitive and selective acetone sensor based on Gd doped WO_3/reduced graphene oxide nanocomposite, Sensors and Actuators B: Chemical, 258 (2018) 1022-1035.
[48] T.K. Takeo Hyodo, Taro Ueda, Kuniyuki Izawa, and Yasuhiro Shimizu, Acetone-Sensing Properties of WO_3-Based Gas Sensors Operated in Dynamic Temperature Modulation Mode —Effects of Loading of Noble Metal and/or NiO onto WO_3, Sensors and materials, 28 (2016) 1179-1189.
[49] A.K. Nayak, R. Ghosh, S. Santra, P.K. Guha, D. Pradhan, Hierarchical nanostructured WO_3–SnO_2 for selective sensing of volatile organic compounds, Nanoscale, 7 (2015) 12460-12473.
[50] J. Cao, S. Wang, H. Zhang, T. Zhang, Facile construction of Co_3O_4 porous microspheres with enhanced acetone gas sensing performances, Materials Science in Semiconductor Processing, 101 (2019) 10-15.
[51] M. Yin, L. Yu, S. Liu, Synthesis of Ag quantum dots sensitized WO_3 nanosheets and their enhanced acetone sensing properties, Materials Letters, 186 (2017) 66-69.
[52] S. Zhang, C. Wang, F. Qu, S. Liu, C.-T. Lin, S. Du, Y. Chen, F. Meng, M. Yang, ZnO nanoflowers modified with RuO_2 for enhancing acetone sensing performance, Nanotechnology, 31 (2020) 115502.
[53] D. Xue, F. Zong, J. Zhang, X. Lin, Q. Li, Synthesis of Fe_2O_3/WO_3 nanocomposites with enhanced sensing performance to acetone, Chemical Physics Letters, 716 (2019) 61-68.
[54] C. Liu, B. Wang, T. Wang, J. Liu, P. Sun, X. Chuai, G. Lu, Enhanced gas sensing characteristics of the flower-like $ZnFe_2O_4$/ZnO microstructures, Sensors and Actuators B: Chemical, 248 (2017) 902-909.
[55] D. Zhang, Z. Yang, Z. Wu, G. Dong, Metal-organic frameworks-derived hollow zinc oxide/cobalt oxide nanoheterostructure for highly sensitive acetone sensing, Sensors and Actuators B: Chemical, 283 (2019) 42-51.
[56] J. Wang, J. Yang, N. Han, X. Zhou, S. Gong, J. Yang, P. Hu, Y. Chen, Highly sensitive and selective ethanol and acetone gas sensors based on modified ZnO nanomaterials, Materials & Design, 121 (2017) 69-76.
[57] S. Chakraborty, M. Pal, Highly selective and stable acetone sensor based on chemically prepared bismuth ferrite nanoparticles, Journal of Alloys and Compounds, 787 (2019) 1204-1211.
[58] M. Yang, S. Zhang, F. Qu, S. Gong, C. Wang, L. Qiu, M. Yang, W. Cheng, High performance acetone sensor based on ZnO nanorods modified by Au nanoparticles, Journal of Alloys and Compounds, 797 (2019) 246-252.
[59] J.M. Xu, J. Zhang, B.B. Wang, F. Liu, Shape-regulated synthesis of cobalt oxide and its gas-sensing property, Journal of Alloys and Compounds, 619 (2015) 361-367.
[60] S. Sen, S. Maity, S. Kundu, Fabrication of Fe doped reduced graphene oxide (rGO) decorated WO_3 based low temperature ppm level acetone sensor: Unveiling sensing mechanism by impedance spectroscopy, Sensors and Actuators B: Chemical, 361 (2022) 131706.
[61] J. Zhang, H. Lu, C. Yan, Z. Yang, G. Zhu, J. Gao, F. Yin, C. Wang, Fabrication of conductive graphene oxide-WO_3 composite nanofibers by electrospinning and their enhanced acetone gas sensing properties, Sensors and Actuators B: Chemical, 264 (2018) 128-138.
[62] L. Zhu, W. Zeng, Y. Li, A novel cactus-like WO_3-SnO_2 nanocomposite and its acetone gas sensing properties, Materials Letters, 231 (2018) 5-7.
[63] X. Li, X. Zhou, H. Guo, C. Wang, J. Liu, P. Sun, F. Liu, G. Lu, Design of Au@ZnO Yolk–Shell Nanospheres with Enhanced Gas Sensing Properties, ACS Applied Materials & Interfaces, 6 (2014) 18661-18667.

Chapter 5: The Effect of Phase Junction of WO_3 on Gas Sensing Performance

Introduction

This chapter explores the synthesis and gas sensing properties of WO_3, which is a promising material for chemical sensing applications. Despite advancements in designing WO_3 with various dimensional structures, achieving high-performance gas sensors remains a challenge. To address this, diverse synthesis methods have been employed to tailor WO_3 morphologies in different dimensions, accompanied by strategies such as crystal facet exposure, elemental doping, and hetero/homojunction formation. By utilizing a simple sol-gel method to fabricate WO_3 phase junctions, this study aims to elucidate the relationship between phase junction formation and gas sensing performance. In this regard, WO_3_P_1 was synthesized in the benzyl alcohol solution with WCl_6, whereas WO_3_P_2 was fabricated in the same solution with PEG 200 as surfactant.

3.5 Morphological properties

Figure 5.1 presents the FESEM results of WO_3_P_1 and WO_3_P_2. Figure 5.1a illustrates the morphology of WO_3_P_1 material synthesized using a benzyl alcohol solution containing WCl_6. The material comprises isolated nanoparticles with a cubical shape. The presence of a metal chloride like WCl_6 as a precursor introduces an intense polarization effect, making its high-valence metal ions susceptible to nucleophilic agent attack, thereby displaying high reactivity. Consequently, controlling the precipitation of WO_3 in a protic solvent becomes challenging [1, 2]. However, our morphological findings suggest that benzyl alcohol serves as an effective solvent for regulating both the reaction rate of WCl_6 and the particle formation process. Benzyl alcohol may play multiple roles, acting as a solvent, an oxygen supplier, and a capping agent [3-5]. Throughout the experimental process, the reaction of WCl_6 in benzyl alcohol leads to a series of color transformations from yellow to orange, light blue, and dark blue, indicative of various charge transfer complexes formed through ligand exchange at tungsten atoms [6, 7]. The dark blue color indicates the partial reduction of W^{VI} [6]. Moreover, the uniform formation of WO_3

particles without agglomeration can be related to the stability of the carbocation intermediate formed during the reaction due to the direct bonding of the benzene ring with the α-carbon [2].

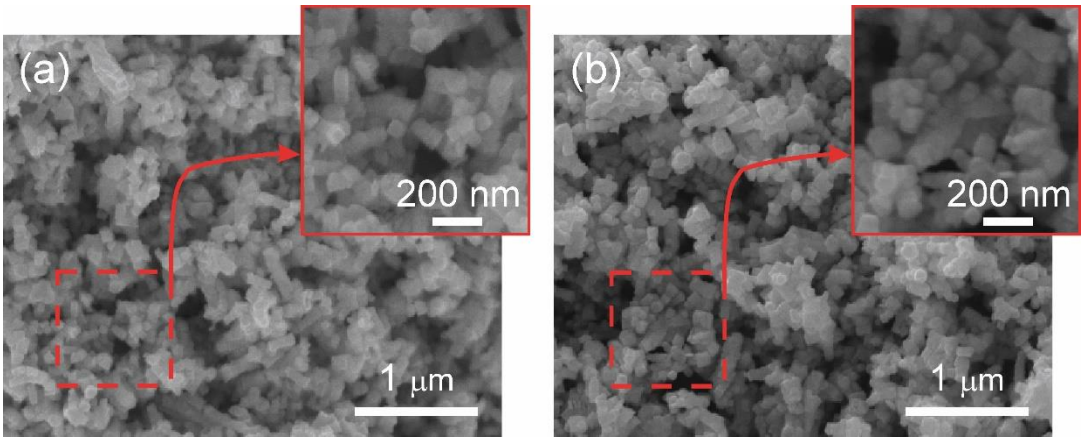

Figure 5.1 a and b) FESEM images of WO_3 nanostructures: a) The morphology of WO_3_P_1 and b) The morphology of WO_3_P_2.

As can be seen in Figure 5.2, WO_3_P_1 nanoparticles exhibit a square-rectangular shape. Both figures depict a consistent presence of a very thin layer of amorphous material (approximately 3 nm) surrounding the nanoparticles. This layer may be attributed to residual ethanol used during the TEM sample preparation and subsequently adsorbed by the material. Moreover, upon closer examination of Figure 5.2b, the entire nanoparticle structure is revealed to consist of numerous very thin nanorods (with a thickness ranging from 1 to 2 nanometers), roughly aligned along a single axis.

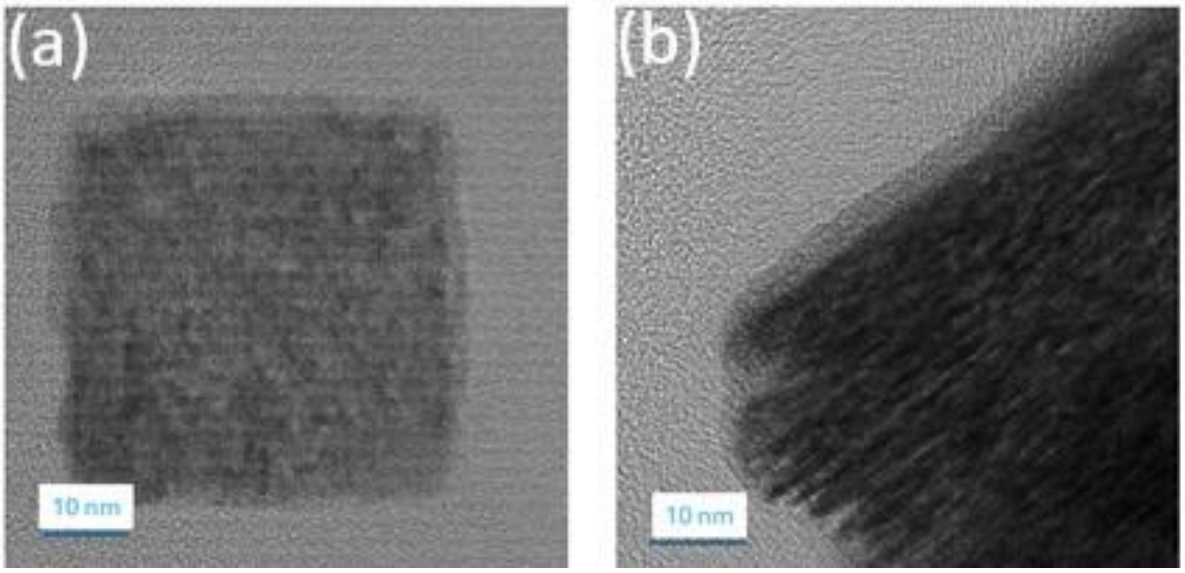

Figure 5.2 a) HR-TEM of a WO_3_P_1 nanoparticle showing a very thin layer of amorphous material and b) another HR-TEM image showing that the entire structure of the nanoparticle appears to consist of a large number of very small nanorods.

As shown in Figure 5.3, the presence of PEG 200 increases the degree of disorder in the overall structure. Generally, this type of nanoparticle looks larger, thicker, and with a more irregular shape. Additionally, the small nanorods described in Figure 5.2 seem to disappear.

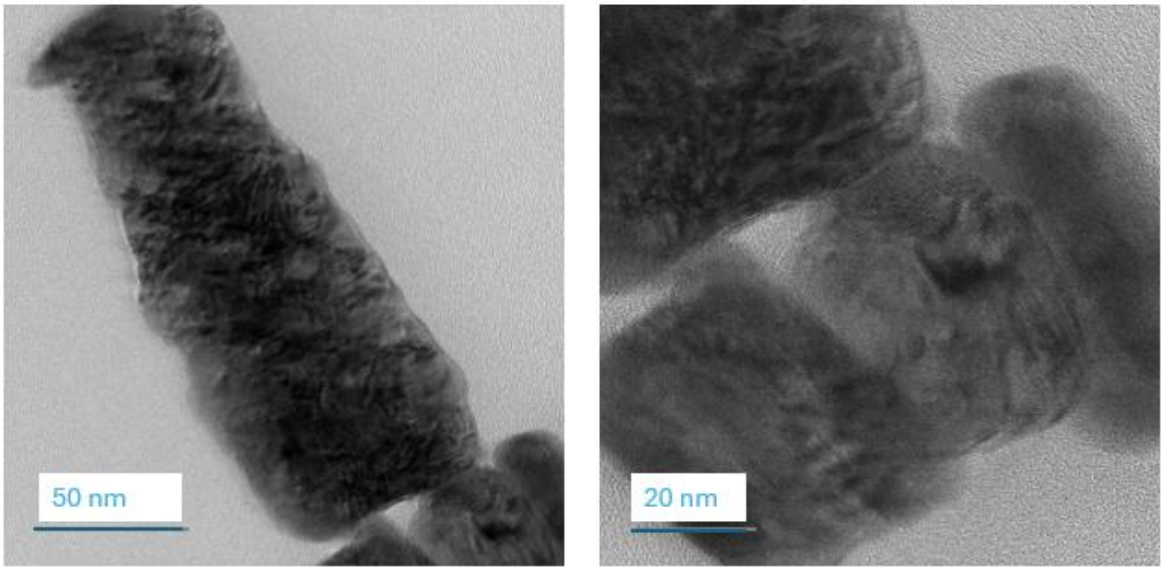

Figure 5.3 TEM images of WO_3_P_2 nanoparticles.

The size distribution of the WO_3_P_1 sample is presented in Figure 5.4a, indicating that the majority of the distribution is centered around 50 and 100 nm, with an average value of 93.86 ± 57.89 nm. The size distribution shown in Figure 5.4b suggests that the presence of PEG leads to an enlargement of the WO_3_P_2 nanoaggregates, with an average size of 120.45 ± 75.17 nm.

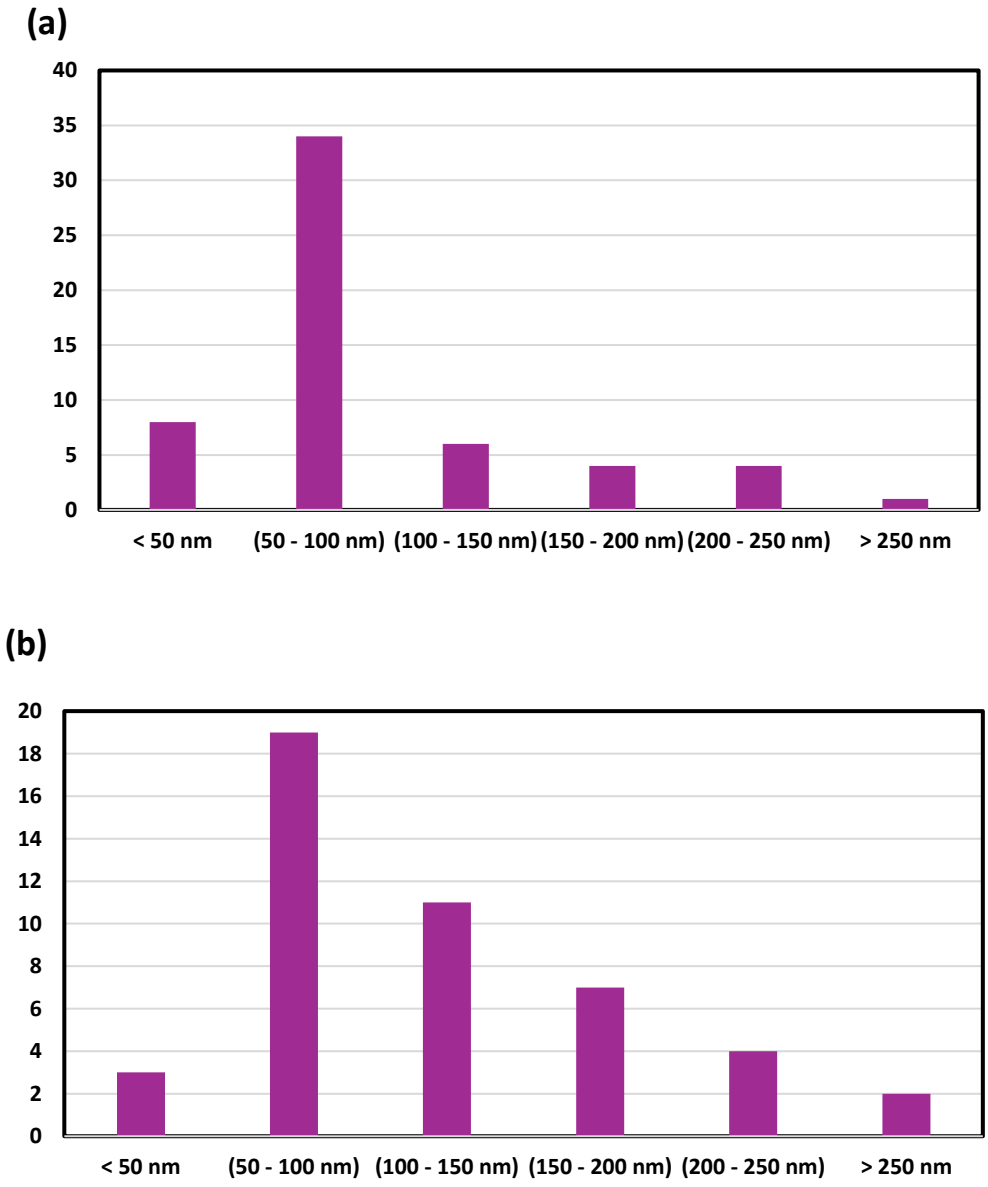

Figure 5.4 Size distribution of the a) WO_3_P_1 and b) WO_3_P_2 nanoparticles.

Figure 5.5 illustrates the X-ray dispersion of W, C, and O elements within a nanoparticle from the WO_3_P_1 sample. The distribution of the elements is quite homogeneous. Through intensity variation analysis, it is evident that the W to O ratio remains constant. The presence of C primarily arises from the grid, although a slight increase in its intensity could be related to ethanol residues.

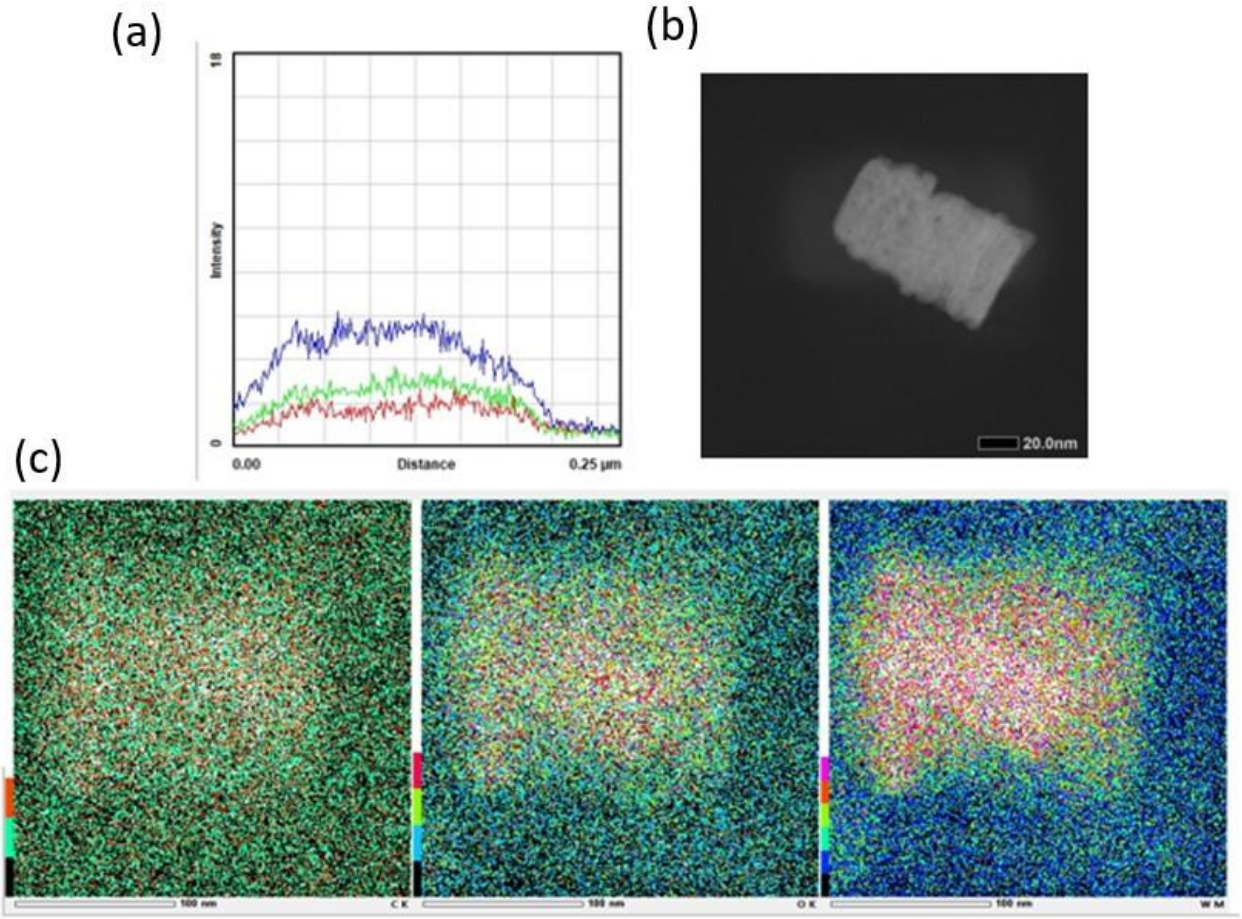

Figure 5.5 a) X-ray Intensity profile of a single WO_3_P_1 nanoparticle (W – blue line, O – green line, C – red line), b) STEM image of WO_3_P_1 nanoparticles and c) X-ray distribution map of the nanoparticle shown in b) for C, O, and W.

Examining the X-ray intensity line profile in Figure 5.6 for the WO_3_P_2 sample, it's evident that the carbon and oxygen contents are higher compared to individual WO_3 nanoparticles. Additionally, an increased concentration of carbon is depicted in the distribution map, clearly visible within the same area of the nanoparticle.

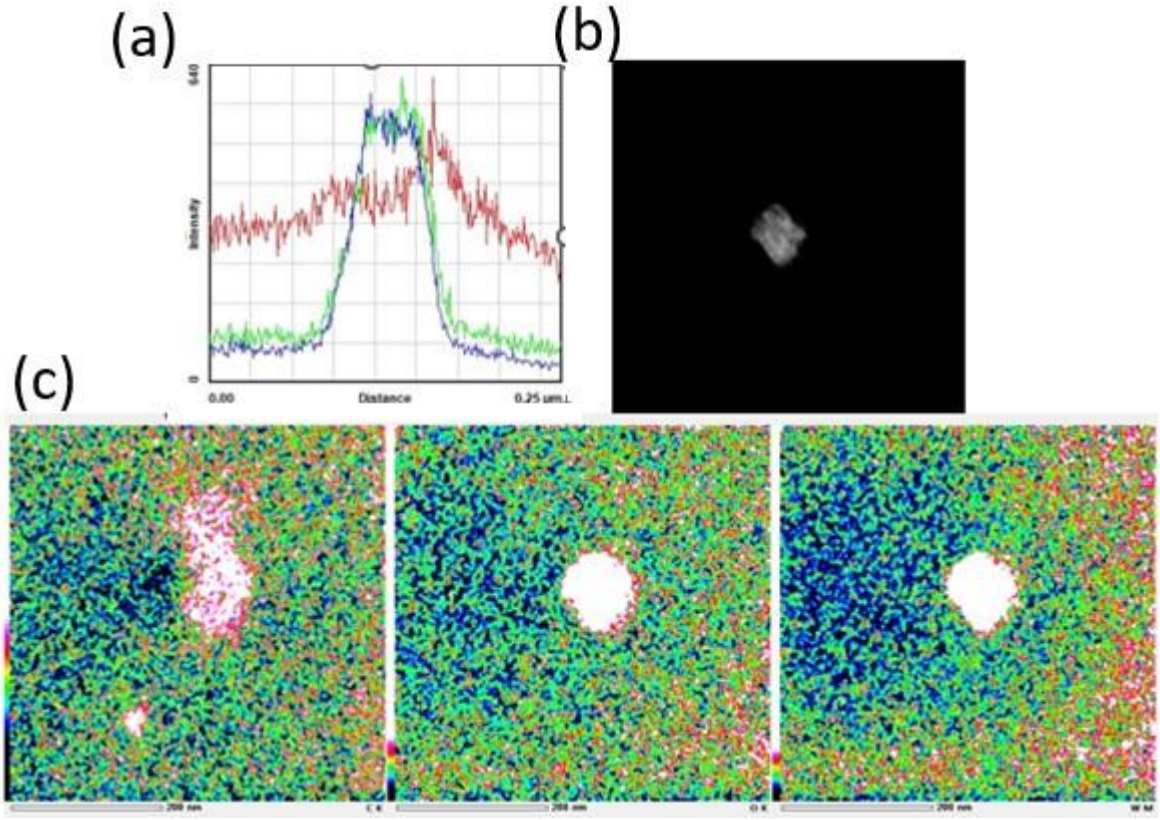

Figure 5.6 a) X-ray Intensity profile of a single WO_3_P_2 nanoparticle (W – blue line, O – green line, C – red line), b) STEM image of a WO_3 nanoparticle and c) X-ray distribution map of the nanoparticle shown in b) for C, O, and W.

3.6 Structural analysis

Figure 5.7a presents the XRD patterns of WO_3_P_1 and WO_3_P_2 nanomaterials. In the case of WO_3_P_1, primary diffraction peaks are observed at 24.1°, 33.96°, 49.36°, 51.96°, 55.13°, and 61.27°, corresponding to the (110), (200), (220), (300), (310), and (312) planes of the monoclinic phase (JCPDS no. 98-003-9121, space group: P 1 c 1), respectively. Conversely, the XRD pattern of WO_3_P_2 exhibits peaks at 23.228°, 23.801°, 24.495°, 26.777°, 28.858°, 50.006°, 80.297°, and 87.111°, assigned to the (020), (002), (200), (102), (121), (104), (541), and (136) planes of the orthorhombic phase (JCPDS no. 98-004-9836, space group: P b c n). Additional peaks at 33.951°,

35.651°, 41.802°, 47.404°, 48.430°, 54.035°, 55.509°, 62.474°, and 67.365° correspond to the (10-2), (12-1), (122), (200), (040), (202), (212), (04-3), and (05-2) planes of the monoclinic phase (JCPDS no. 98-007-1692, space group: P 1 21/c 1 and space group number: 14). The peak intensities in WO_3_P_2 appear sharper and narrower compared to those in WO_3_P_1, indicating that PEG 200 enhances the crystallinity of WO_3 nanomaterial. Thus, the presence of PEG in the synthesis process significantly influences the formation of a crystalline WO_3 nanostructure and provides a means to control its crystallinity [8-10].

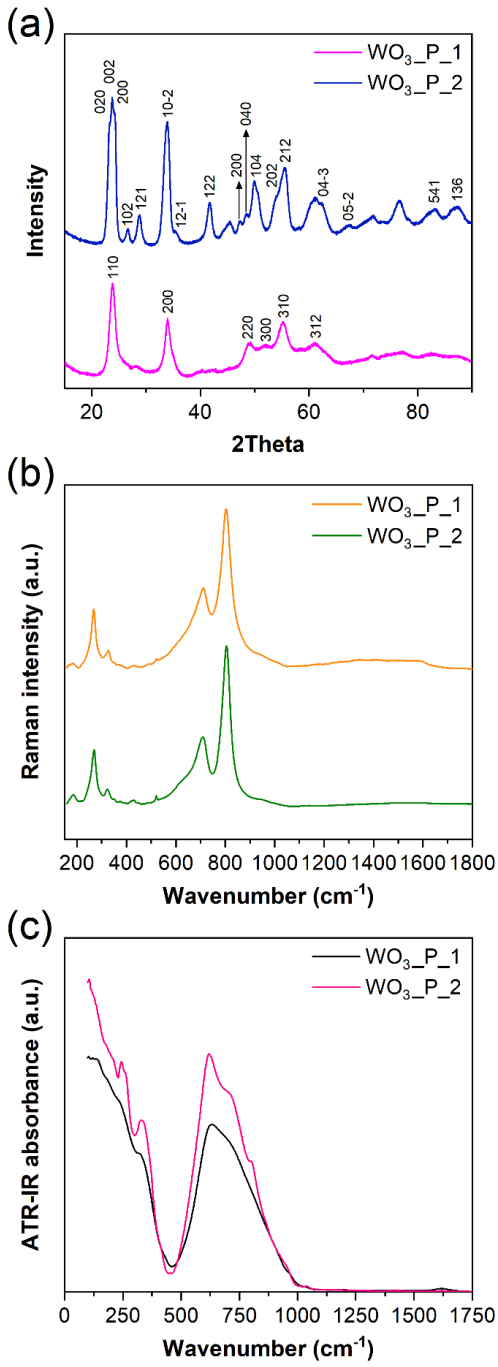

Figure 5.7 a) XRD patterns of WO_3_P_1 and WO_3_P_2 samples, b) Raman Spectra of WO_3_P_1 and WO_3_P_2 and c) ATR-IR spectra of WO_3_P_1 and WO_3_P_2.

The Raman spectra presented in Figure 5.7b illustrate the vibrational characteristics of WO_3_P_1 and WO_3_P_2. Both spectra display prominent vibrational bands at 184, 324, 710, and 805 cm^{-1}, associated with the monoclinic phase. The bands at 805 and 710 cm^{-1} can be attributed to the stretching vibration of O–W–O [11-15], while the band at 324 cm^{-1} corresponds to the O–W–O

bending vibration. Additionally, the presence of a peak at 184 cm^{-1} is ascribed to the lattice mode, and a frequency shift to higher values is observed in the WO_3_P_2 sample.

Furthermore, in contrast to the WO_3_P_1 material, the spectrum of WO_3_P_2 exhibits peaks and shoulders indicative of the orthorhombic phase (Table 5.1). Notably, three main vibrational bands (269, 376, and 632 cm^{-1}) characteristic of the orthorhombic phase are evident. The bands at 632 cm^{-1} and 376 cm^{-1} are attributed to the stretching vibration of the bridging oxygen O–W–O [16], while the peak at 269 cm^{-1} corresponds to the deformation of W–O–W [11, 16]. Additionally, the highest frequency peak at 940 cm^{-1} observed in both samples can be related to the W=O stretching vibration of terminal oxygen [15, 17]. This particular vibration is typically absent in three-dimensional structures like orthorhombic and monoclinic phases [16].

Table 5.1 Raman peak positions and chemical group assignment of WO_3_P_1 and WO_3_P_2 nanomaterials.

Frequency position (cm^{-1}) Sample WO_3 _P_1	**Frequency position (cm^{-1}) Sample WO_3_P_2**	**Assignment**
184	186	ν(W−O−W)[14, 16] lattice mode[11]
268	270	δ(O−W−O)[11, 14, 16]*
328	324	O−W−O deformation mode[14, 16, 18] ν(W−OH_2)[11]
	353	
370		
	376	orthorhombic[16]
	397	

430	431	[11]
522	521	Si−O
	616	
	633	Orthorhombic[16]
713	713	ν (O−W−O)[16, 19] Monoclinic [11]
804	806	stretching (O−W−O)[11, 16]
940	940	Stretching (W=O)* [15, 16]

The ATR-IR spectra, illustrated in Figure 5.7c, highlight the characteristics of WO_3_P_1 and WO_3_P_2 samples, and detailed absorption frequencies reported in Table 5.2 with their assigned vibrational modes. In the far-IR region, WO_3_P_1 displays main characteristic bands at 348 cm^{-1}, 326 cm^{-1}, and 234 cm^{-1}, attributed to δ(W–O), ν(W–OH_2), and ν(W–O–W) vibrations, respectively [11, 20-22]. The band at 369 cm^{-1} is associated with vibrational modes of water molecules [20, 22]. In the very low-frequency region (below 200 cm^{-1}), IR bands are assigned to lattice modes of WO_3 and its hydrates [20], with more intense ones located at 182, 145, 120, and 105 cm^{-1}. The dominant broad band at 633 cm^{-1}, along with shoulders at 714 and 730 cm^{-1}, corresponds to the ν(W–O) vibrational modes [20, 22]. Peaks identified through 2nd derivative analysis are found at 816 and 970 cm^{-1}, corresponding to ν(O–W–O) and ν(W=O), respectively [21]. Furthermore, the ATR-IR spectrum of WO_3_P_1 exhibits two IR bands at 1621 and 1600 cm^{-1}, representing the bending mode of H_2O molecules and indicating the water content in the sample [23, 24].

In the far-IR region, the ATR-IR spectrum of the WO_3_P_2 sample reveals primary characteristic bands at 343 cm^{-1} (corresponding to δ(W–O)), 323 cm^{-1} (representing ν(W–OH_2)), and 243 cm^{-1}

(associated with ν(W–O–W)) [11, 20-22]. The band at 370 cm^{-1} is attributed to the vibration modes of water molecules [20, 22]. In the low-frequency region, primary absorption bands are assigned to WO_3 lattice modes and its hydrates, which are identified at 178, 148, 120, and 105 cm^{-1} [20]. The broad intense band at 633 cm^{-1}, along with a shoulder at 718 cm^{-1}, corresponds to the ν(W–O) vibrational modes [20, 22]. Two shoulders identified around 753 and 869 cm^{-1} are associated with ν(O–W–O) vibrations, indicative of the bridging vibration of the corner-sharing WO_6 octahedron in the WO_3 crystal [21, 25]. Weak bands in the spectral regions of 1450−1510 cm^{-1}, 1310–1410 cm^{-1}, and 1260−1350 cm^{-1} are attributed to C=C–C aromatic ring stretching, O–H bend, and O–H in plane bend (as observed in phenol), respectively. Notably, bands at 1481, 1343, and 1272 cm^{-1} can be assigned to PEG 200 [26, 27]. The ATR-IR spectrum of the WO_3_P_2 structure displays an IR band at 1621 cm^{-1}, indicating the presence of water content in the sample.

The comparison depicted in Figure 5.7c reveals slight difference between the spectra of WO_3_P_1 and WO_3_P_2 within the 600–1000 cm^{-1} spectral range. It is well-known that the vibrational spectra of different WO_3 polymorphs exhibit variations. However, many studies in the literature seem to overlook the description of the low-frequency range spanning 200–500 cm^{-1} [22, 24, 28]. Notably, it is evident from Figure 5.7c that the major difference between the WO_3_P_1 and WO_3_P_2 materials is particularly visible within the low-frequency range of 50 to 500 cm^{-1}. In this range, both samples display absorption bands at 57, 72, 105, 120, 138, 145, 194, 323, and 370 cm^{-1}. Additionally, significant variations in peak positions are evident between the WO_3_P_1 and WO_3_P_2 samples. Specifically, the lattice mode peak at 87 cm^{-1} in the WO_3_P_1 spectrum shifts to a higher frequency of 92 cm^{-1} in the WO_3_P_2 spectrum, while the peak at 182 cm^{-1} shifts to a lower frequency of 178 cm^{-1} in the spectrum of WO_3_P_2. Furthermore, the absorption band at 234 cm^{-1} in the WO_3_P_1 spectrum, associated with the ν(W–O–W) vibration, shifts to a higher frequency of 243 cm^{-1} in the WO_3_P_2 spectrum. Lastly, the absorption related to the W–O bending at 348 cm^{-1} in the WO_3_P_1 spectrum shifts to 343 cm^{-1} in the WO_3_P_2 spectrum.

Furthermore, the significant difference is observed in the mid-infrared region between the spectra of the two materials, which can be related to the utilization of PEG 200 as a surfactant

[26, 27]. The signal intensity related to the H_2O bending mode, observed at 1621 and 1600 cm^{-1}, is more pronounced in the spectrum of WO_3_P_1 in comparison to WO_3_P_2, indicating a higher water content in the sample prepared without the use of PEG. Additionally, both samples display vibrational bands above 3000 cm^{-1}, associated with the CH stretching of the benzyl alcohol solvent.

Table 5.2 Infrared peak/band positions and chemical group assignments of WO_3_P_1 and WO_3_P_2 nanomaterials.

Frequency position (cm^{-1}), Sample WO_3_P_1	**Frequency position (cm^{-1}), Sample WO_3_P_2**	**Assignment**
57	59	lattice modes
72	75	lattice modes
87	-	lattice modes
-	92	lattice modes
105	105	lattice modes
120	120	lattice modes
139	137	lattice modes
145	148	lattice modes
-	178	lattice modes
182	-	lattice modes
194	194	lattice modes
-	212	lattice modes
234	-	ν(W–O–W)
	243	ν(W–O–W)
326	323	ν(W–OH_2)
348	343	δ(W–O)
369	370	ν(W–OH_2)
-	417	water libration

430	-	
-	453	
	554	
602	601	
618	617	
633	**633**	v(W−O)
715	**717**	v(W−O)
730	-	v(W−O)
756	753	v(O−W−O)
787	-	
	806	
816	-	v(O−W−O)
	869	v(O−W−O)
	926	
	961	v(W=O)
970		v(W=O)
	1012	
1039	1038	
	1093	
	1130	
	1184	
	1272	OH in plane bend
	1343	OH in plane bend
1377	-	OH -bend
1413	1408	deformation OH
	1436	
	1481	due to PEG C=C−C aromatic ring stretching

1540		
1600		deformation OH
1621	1621	deformation OH
1805	1804	Aromatic combination Bands
1828	1828	Aromatic combination Bands
1947	1946	Aromatic combination Bands
	2660	
2848		ν(C−H)
	2863	ν(C−H) due to PEG
2871		ν(C−H)
2918		ν(C−H)
	2928	ν(C−H)
2955	2958	ν(C−H)
3234	3234	ν(O−H)
3343	3343	ν(O−H)
3545	3545	ν(O−H) due to $WO_3.2H_2O$
3560		ν(O−H)

3.7 Gas sensing result

Figure 5.8a illustrates the response of WO_3_P_1 and WO_3_P_2 sensors to 10 ppm of acetone at various operating temperatures and 40% relative humidity (RH) in the test chamber. The response values for both materials are provided in Table 5.3. WO_3_P_1 shows minimum sensitivity to acetone at 200 °C, with a response value of 0.01. However, its response improves

to 3 at 250 °C, slightly increasing to 3.1 at 300 °C. The response curve exhibits a more significant slope from 300 to 400 °C, reaching its maximum value of 8.7 at 400 °C. A similar trend is observed for WO_3_P_2, with its response increasing as the operating temperature rises from 200 to 300 °C and further from 300 to 400 °C. Notably, between 300 and 400 °C, WO_3_P_2 exhibits a significantly higher improvement in sensing response compared to WO_3_P_1, with the response value increasing from 9 to 62. Consequently, WO_3_P_2 exhibits a remarkably superior acetone sensing response compared to WO_3_P_1.

Table 5.3 Response of materials towards 10 ppm of acetone at different temperatures.

Temperature (°C)	**Response of WO_3_P_1**	**Response of WO_3_P_2**
200	0.01	1.3
250	3	3.3
300	3.1	9
350	5.3	27.3
400	8.7	62

Figure 5.8b illustrates the dynamic response of WO_3_P_1 and WO_3_P_2 materials to various concentrations of acetone at an optimal operating temperature of 400 °C. The baseline conductance of sensors stabilizes in the presence of environmental oxygen adsorption on their surface. Upon exposure to acetone, the conductance values of the structures increase, a characteristic behavior of n-type semiconductor materials owing to the adsorption of reducing gaseous on their surface. Acetone molecules interact with adsorbed oxygen species on the nanostructure's surface, releasing electrons back to the conduction band. After the gas chamber is purified with a synthetic air flow, the recovery of each material's conductance to its initial air value confirms its reversible sensing properties. Moreover, the response curves versus acetone concentration for both sensors (Figure 5.8c) confirm the superior functionality of WO_3_P_2 over WO_3_P_1. Notably, WO_3_P_2, which was prepared using PEG 200, demonstrates a high response even toward low concentrations (200 ppb) of acetone.

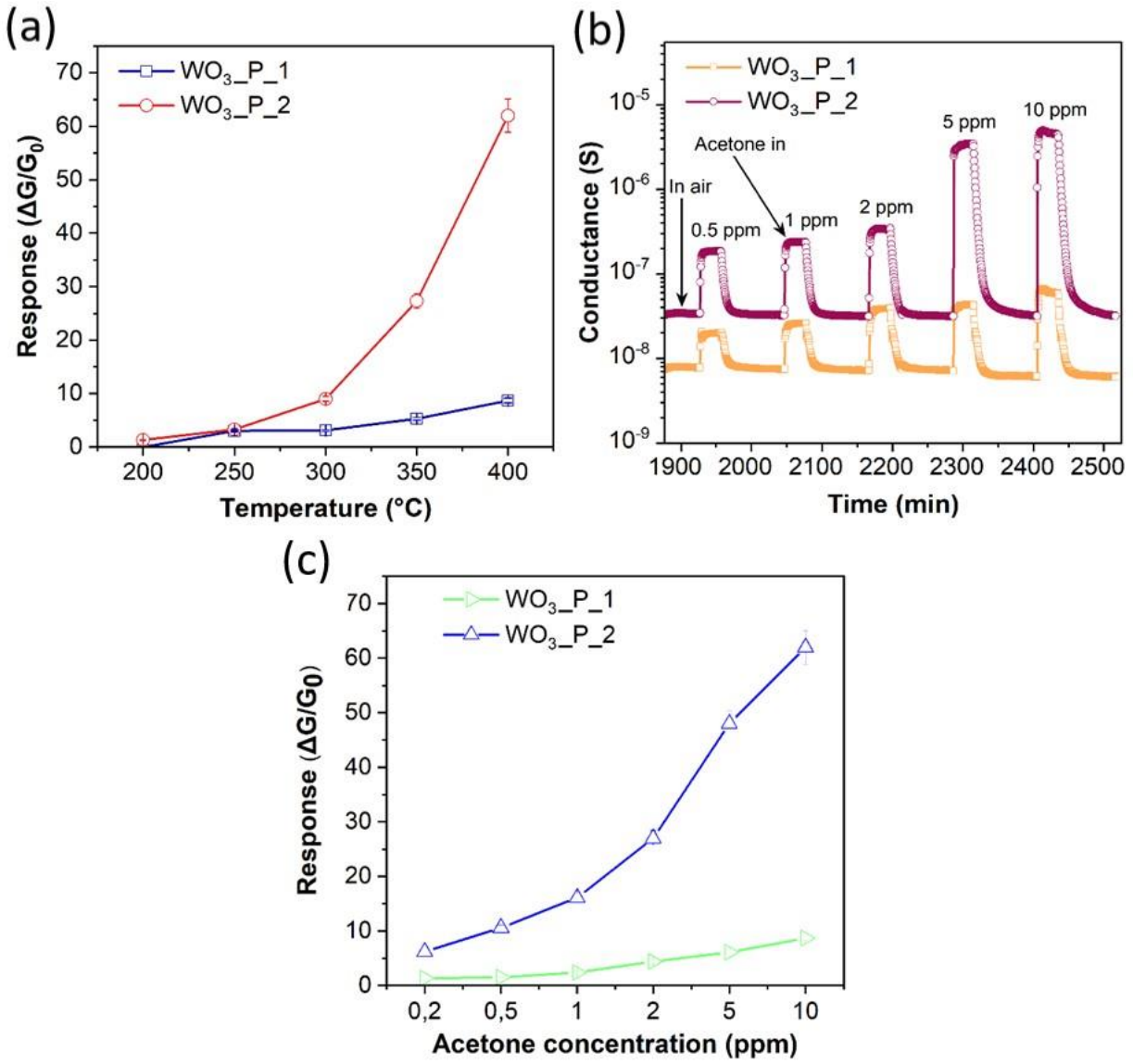

Figure 5.8 a) Response vs temperature dependence of WO_3_P_1 and WO_3_P_2 sensors toward 10 ppm of acetone (40% RH), b) Dynamic response of WO_3_P_1 and WO_3_P_2 toward different concentrations of acetone at RH of 40% and c) Gas sensing response of WO_3_P_1 and WO_3_P_2 toward 0.2−10 ppm of acetone at 400 °C.

Figures 5.8b and 5.9a−b illustrate that the use of PEG 200 as a surfactant contributes to the enhancement in the conductance of WO_3_P_2. The disparity in conductance between WO_3_P_1 and WO_3_P_2 may be attributed to the exposure of different crystal surfaces, influencing the pre-adsorbed oxygen ions at specific temperatures [29, 30]. Additionally, ATR-IR results confirm

the presence of carbon in WO_3_P_2, suggesting a potential increase in charge transfer and resulting in increasing its conductance.

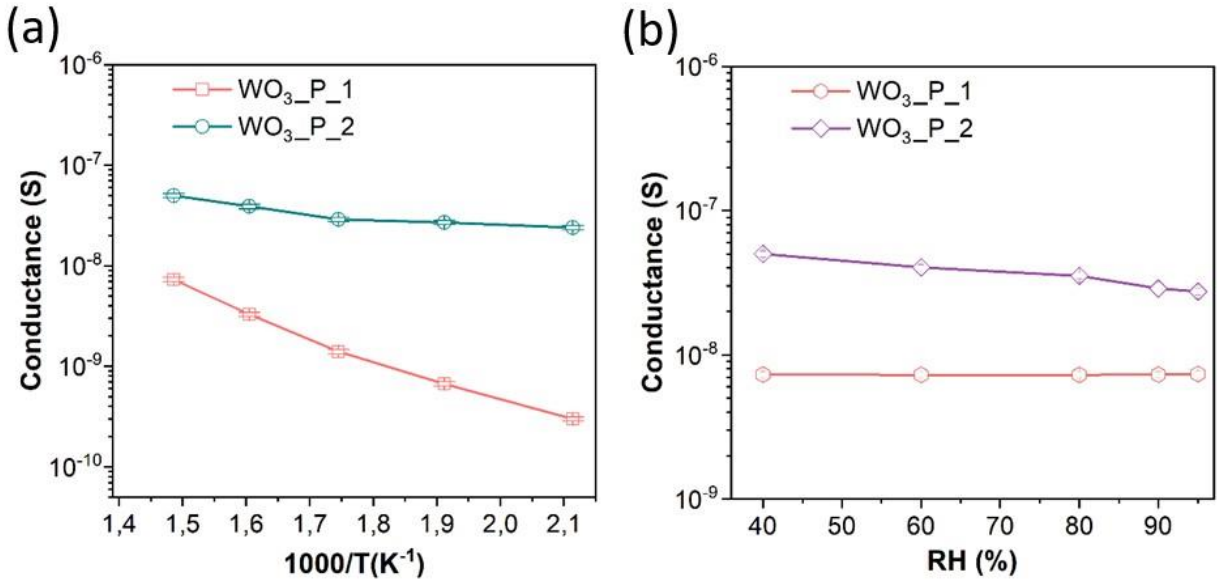

Figure 5.9 a) Temperature-dependent conductance of WO_3_P_1 and WO_3_P_2 structures (200−400 °C) and b) Humidity- dependent Conductance of WO_3_P_1 and WO_3_P_2 materials (40−95%).

ATR-IR analyses reveals specific bands (e.g., those at 1481, 1343, and 1272 cm^{-1}) indicative of residual PEG presence in the WO_3 matrix. Since PEG exhibits conductivity properties, the observed higher conductivity in WO_3_P_2 compared to WO_3_P_1 aligns with the findings from FTIR investigations. Considering this, it is plausible that PEG 200 may influence sorption mechanisms, potentially contributing to the enhanced sensitivity in the WO_3_P_2 material.

However, a more significant observation pertains to the displacement of water content in the precursor material due to the presence of the PEG 200 surfactant. Chacon et al. have previously reported that during the synthesis of WO_3, a low concentration of water in the initial solution favors the orthorhombic crystal structure, while a higher water content leads to dominance of the monoclinic phase [31]. This finding aligns precisely with our observations. Specifically, the XRD pattern and Raman spectra (Figures 5.7a and b) indicate a mixture of orthorhombic and

monoclinic phases in the WO_3_P_2 sample, whereas only the monoclinic phase is detected in WO_3_P_1.

The significant improvement in acetone sensitivity in WO_3_P_2 can be attributed to the dual effects of inhibiting hydrate formation and the presence of ortho/mono n-n homojunction in the WO_3 polymorph. The use of PEG 200 as a surfactant effectively prevents hydrate formation, leading to a notable rise in the number of active adsorption sites on the material's surface. Moreover, the inhibition of hydrate formation and an increase in the surface acidity of the WO_3_P_2 sensor significantly enhances acetone adsorption, particularly benefiting from acetone's weak basic properties.

However, a more detailed investigation is required to check the formation of ortho/mono homojunctions and understand the impact of ortho/mono homojunctions on sensitivity. In this regard, our collaborations are carrying out the UPS and XPS analysis and DFT calculation.

Moreover, we explored the effect of RH on the electrical and sensing properties of the prepared materials by increasing its concentration in the test chamber up to 95% (Figures 5.9b and 5.10a). The interaction between H_2O vapor and WO_3 involves the dissociation of H_2O molecules, forming OH^- hydroxyl groups and H^+ protons on the WO_3 surface. This phenomenon arises from various interaction mechanisms between H_2O vapor and WO_3 nanostructures. The competitive adsorption of water and acetone on the WO_3 surface is a complex process, where adsorbed water molecules may influence the formation and number of oxidized species for acetone adsorption. Additionally, H_2O can catalyze adsorption reactions on metal oxide surfaces [19, 32]. The findings reveal that, even at a low concentration of acetone (200 ppb), there are no notable changes in the conductance and response of WO_3_P_1 and WO_3_P_2 sensors with the rise in RH level (up to 95%) in the chamber. Hence, the findings provide insights into the properties of WO_3_P_2 to detect acetone in breath analysis due to its excellent gas sensing performances even in highly humid environments (95%).

In Figure 5.10b, the response of WO_3_P_1 and WO_3_P_2 to various gaseous compounds is illustrated, highlighting the excellent selectivity of both materials. WO_3_P_2, in particular, demonstrates high sensitivity to acetone. A comparison of its acetone sensing performances

with those of other semiconductor gas sensors based on pure and composite structures is presented in Table 5.4. The results underscore the significant impact of WO_3 nanostructure and the appropriate modification of its crystalline structure on its functional properties.

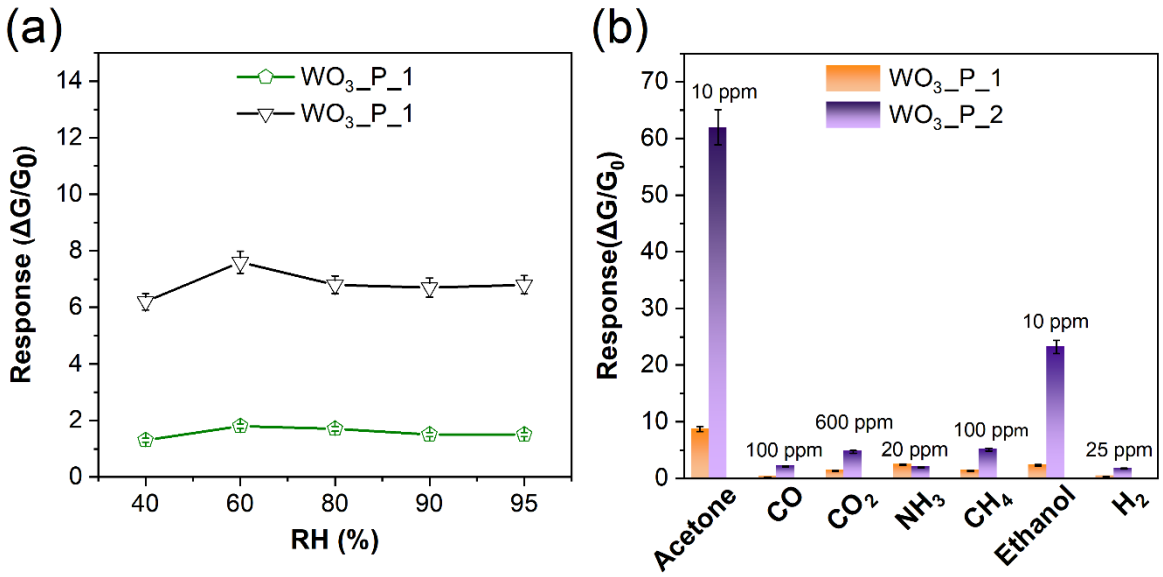

Figure 5.10 a) Response values of WO_3_P_1 and WO_3_P_2 sensors to 200 ppb of acetone at different concentrations of RH (40−95%) in the test chamber. The operating temperature of sensors is 400 °C and b) Sensing response of WO_3_P_1 and WO_3_P_2 toward different gaseous and volatile organic compounds at their optimum operating temperature (400 °C).

Table 5.4 Acetone sensing properties of different metal oxide structures.

Material	Temperature (℃)	Concentration (ppm)	Response	Ref.
WO_3	200	100	28.7	[29]
Au/WO_3	410	1.5	7.6	[33]
Ru-SnO_2	250	100	340	[34]
PdO@ZnO–SnO_2	400	1	5.1	[35]
TiO_2	320	100	12.1	[36]
Pt- WO_3	300	2	4.11	[37]
WO_3	260	1	4.6	[30]
ZnO	350	5	42	[38]
PdO–Co_3O_4	350	5	2.51	[39]
Sb_2O_3/WO_3	200	100	49.8	[40]
Rh_2O_3-WO_3	250	5, 2	41.2,7.9	[41]
Bi–$ZnSnO_3$/CuO	375	100	386.19	[42]
WO_3_P_2	400	10	62	This work
	350	10	27.3	
	300	10	9	
	250	10	3.3	
	200	10	1.3	

Conclusions

The study explored the morphology, structure, and gas sensing properties of WO_3_P_1 and WO_3_P_2. Notably, PEG 200 influences crystallinity, enhancing the sensitivity of WO_3_P_2 to acetone. The inhibition of hydrate formation and the presence of ortho/mono n-n homojunction contributed to improve acetone adsorption in WO_3_P_2. WO_3_P_2 demonstrates consistent gas sensing performance at different humidity levels (40 to 95%), making it promising for breath analysis. The comparison with other sensors underscores the pivotal role of WO_3 nanostructure and crystalline modification in functional efficiency.

References

[1] X.-L. Li, T.-J. Lou, X.-M. Sun, Y.-D. Li, Highly Sensitive WO_3 Hollow-Sphere Gas Sensors, Inorganic Chemistry, 43 (2004) 5442-5449.

[2] M. Hu, J. Xu, J. Gao, S. Yang, J.S.P. Wong, R.K.Y. Li, Benzyl alcohol-based synthesis of oxide nanoparticles: the perspective of S_N1 reaction mechanism, Dalton Transactions, 42 (2013) 9777-9784.

[3] M. Niederberger, M.H. Bartl, G.D. Stucky, Benzyl alcohol and titanium tetrachloride a versatile reaction system for the nonaqueous and low-temperature preparation of crystalline and luminescent titania nanoparticles, Chemistry of Materials, 14 (2002) 4364-4370.

[4] D. Malwal, G. Packirisamy, Recent advances in the synthesis of metal oxide (MO) nanostructures, Synthesis of Inorganic Nanomaterials, (2018) 255-281.

[5] M. Niederberger, N. Pinna, J. Polleux, M. Antonietti, A general soft-chemistry route to perovskites and related materials: synthesis of $BaTiO_3$, $BaZrO_3$, and $LiNbO_3$ nanoparticles, Angewandte Chemie, 116 (2004) 2320-2323.

[6] I. Olliges-Stadler, J. Stötzel, D. Koziej, M.D. Rossell, J.-D. Grunwaldt, M. Nachtegaal, R. Frahm, M. Niederberger, Study of the Chemical Mechanism Involved in the Formation of Tungstite in Benzyl Alcohol by the Advanced QEXAFS Technique, Chemistry – A European Journal, 18 (2012) 2305-2312.

[7] M. Niederberger, Nonaqueous Sol–Gel Routes to Metal Oxide Nanoparticles, Accounts of Chemical Research, 40 (2007) 793-800.

[8] Y. Li, Z. Liu, X. Liang, J. Ya, T. Cui, Z. Liu, Synthesis and electrochromic properties of PEG doped WO_3 film, Materials Technology, 29 (2014) 341-349.

[9] C. Santato, M. Odziemkowski, M. Ulmann, J. Augustynski, Crystallographically Oriented Mesoporous WO_3 Films: Synthesis, Characterization, and Applications, Journal of the American Chemical Society, 123 (2001) 10639-10649.

[10] J.K. Kim, K. Shin, S.M. Cho, T.-W. Lee, J.H. Park, Synthesis of transparent mesoporous tungsten trioxide films with enhanced photoelectrochemical response: application to unassisted solar water splitting, Energy & Environmental Science, 4 (2011) 1465-1470.

[11] M. Daniel, B. Desbat, J. Lassegues, B. Gerand, M. Figlarz, Infrared and Raman study of WO_3 tungsten trioxides and WO_3, xH_2O tungsten trioxide tydrates, Journal of solid state chemistry, 67 (1987) 235-247.

[12] U.O. Krašovec, A.Š. Vuk, B. Orel, IR Spectroscopic studies of charged–discharged crystalline WO_3 films, Electrochimica Acta, 46 (2001) 1921-1929.

[13] E. Cazzanelli, C. Vinegoni, G. Mariotto, A. Kuzmin, J. Purans, Low-temperature polymorphism in tungsten trioxide powders and its dependence on mechanical treatments, Journal of Solid State Chemistry, 143 (1999) 24-32.

[14] K. Thummavichai, N. Wang, F. Xu, G. Rance, Y. Xia, Y. Zhu, In situ investigations of the phase change behaviour of tungsten oxide nanostructures, Royal Society open science, 5 (2018) 171932.

[15] M.P. Thi, G. Velasco, Raman study of WO_3 thin films, Solid State Ionics, 14 (1984) 217-220.

[16] B. Pecquenard, H. Lecacheux, J. Livage, C. Julien, Orthorhombic WO_3 Formed via a Ti-Stabilized $WO_3{\cdot}13H_2O$ Phase, Journal of Solid State Chemistry, 135 (1998) 159-168.

[17] G. Ramans, J. Gabrusenoks, A. Veispals, Structure of tungstic acids and amorphous and crystalline WO_3 thin films, Physica Status Solidi. A, Applied Research, 74 (1982) K41-K44.

[18] R.F. Garcia-Sanchez, T. Ahmido, D. Casimir, S. Baliga, P. Misra, Thermal effects associated with the Raman spectroscopy of WO_3 gas-sensor materials, The Journal of Physical Chemistry A, 117 (2013) 13825-13831.

[19] V. Galstyan, N. Poli, A. D'Arco, S. Macis, S. Lupi, E. Comini, A novel approach for green synthesis of WO_3 nanomaterials and their highly selective chemical sensing properties, Journal of Materials Chemistry A, 8 (2020) 20373-20385.

[20] M. Gotić, M. Ivanda, S. Popović, S. Musić, Synthesis of tungsten trioxide hydrates and their structural properties, Materials Science and Engineering: B, 77 (2000) 193-201.

[21] C. Balázsi, M. Farkas-Jahnke, I. Kotsis, L. Petrás, J. Pfeifer, The observation of cubic tungsten trioxide at high-temperature dehydration of tungstic acid hydrate, Solid State Ionics, 141-142 (2001) 411-416.

[22] G.N. Kustova, Y.A. Chesalov, L.M. Plyasova, I.Y. Molina, A.I. Nizovskii, Vibrational spectra of $WO_3{\cdot}nH_2O$ and WO_3 polymorphs, Vibrational Spectroscopy, 55 (2011) 235-240.

[23] S.M. Kanan, C.P. Tripp, Synthesis, FTIR studies and sensor properties of WO_3 powders, Current Opinion in Solid State and Materials Science, 11 (2007) 19-27.

[24] T.M. Bushkova, A.A. Egorova, A.V. Khoroshilov, O.S. Ivanova, A.D. Yapryntsev, A.E. Baranchikov, V.K. Ivanov, Selective Synthesis of γ-WO_3 and β-$WO_3{\cdot}H_2O$ by the Hydrothermal Treatment of Peroxotungstic Acid, Russian Journal of Inorganic Chemistry, 66 (2021) 496-501.

[25] H.F. Pang, X. Xiang, Z.J. Li, Y.Q. Fu, X.T. Zu, Hydrothermal synthesis and optical properties of hexagonal tungsten oxide nanocrystals assisted by ammonium tartrate, physica status solidi (a), 209 (2012) 537-544.

[26] Z. Varga, J. Mihály, S. Berényi, A. Bóta, Structural characterization of the poly (ethylene glycol) layer of sterically stabilized liposomes by means of FTIR spectroscopy, European polymer journal, 49 (2013) 2415-2421.

[27] K. Shameli, M.B. Ahmad, S.D. Jazayeri, S. Sedaghat, P. Shabanzadeh, H. Jahangirian, M. Mahdavi, Y. Abdollahi, Synthesis and characterization of polyethylene glycol mediated silver nanoparticles by the green method, International journal of molecular sciences, 13 (2012) 6639-6650.

[28] R. Hatel, M. Baitoul, A novel approach to synthesize nanostructured WO_3 and graphene/WO_3 nanocomposites: Structural and morphological investigations, Materials Chemistry and Physics, 225 (2019) 169-173.

[29] Q. Wang, X. Cheng, Y. Wang, Y. Yang, Q. Su, J. Li, B. An, Y. Luo, Z. Wu, E. Xie, Sea urchins-like WO_3 as a material for resistive acetone gas sensors, Sensors and Actuators B: Chemical, 355 (2022) 131262.

[30] S. Wei, S. Li, R. Wei, S. Liu, W. Du, Different morphologies of WO_3 and their exposed facets-dependent acetone sensing properties, Sensors and Actuators B: Chemical, 329 (2021) 129188.

[31] C. Chacón, M. Rodríguez-Pérez, G. Oskam, G. Rodríguez-Gattorno, Synthesis and characterization of WO_3 polymorphs: monoclinic, orthorhombic and hexagonal structures, Journal of Materials Science: Materials in Electronics, 26 (2015) 5526-5531.

[32] H. Pakdel, V. Galstyan, A. D'Arco, T. Mancini, S. Lupi, A. Moumen, M. Borsi, E. Comini, Synthesis of WO_3 nanopowder using a green surfactant for efficient gas sensing applications, Ceramics International, 49 (2023) 30501-30509.

[33] X. Zhang, B. Dong, W. Liu, X. Zhou, M. Liu, X. Sun, J. Lv, L. Zhang, W. Xu, X. Bai, Highly sensitive and selective acetone sensor based on three-dimensional ordered WO_3/Au nanocomposite with enhanced performance, Sensors and Actuators B: Chemical, 320 (2020) 128405.

[34] J. Li, J. Xian, W. Wang, K. Cheng, M. Zeng, A. Zhang, S. Wu, X. Gao, X. Lu, J.-M. Liu, Ultrafast response and high-sensitivity acetone gas sensor based on porous hollow Ru-doped SnO_2 nanotubes, Sensors and Actuators B: Chemical, 352 (2022) 131061.

[35] W.-T. Koo, J.-S. Jang, S.-J. Choi, H.-J. Cho, I.-D. Kim, Metal–organic framework templated catalysts: dual sensitization of PdO–ZnO composite on hollow SnO_2 nanotubes for selective acetone sensors, ACS applied materials & interfaces, 9 (2017) 18069-18077.

[36] S. Cao, N. Sui, P. Zhang, T. Zhou, J. Tu, T. Zhang, TiO_2 nanostructures with different crystal phases for sensitive acetone gas sensors, Journal of Colloid and Interface Science, 607 (2022) 357-366.

[37] S.-J. Choi, I. Lee, B.-H. Jang, D.-Y. Youn, W.-H. Ryu, C.O. Park, I.-D. Kim, Selective diagnosis of diabetes using Pt-functionalized WO_3 hemitube networks as a sensing layer of acetone in exhaled breath, Analytical chemistry, 85 (2013) 1792-1796.

[38] X. Zhou, A. Wang, Y. Wang, L. Bian, Z. Yang, Y. Bian, Y. Gong, X. Wu, N. Han, Y. Chen, Crystal-defect-dependent gas-sensing mechanism of the single ZnO nanowire sensors, ACS sensors, 3 (2018) 2385-2393.

[39] W.-T. Koo, S. Yu, S.-J. Choi, J.-S. Jang, J.Y. Cheong, I.-D. Kim, Nanoscale PdO catalyst functionalized Co3O4 hollow nanocages using MOF templates for selective detection of acetone molecules in exhaled breath, ACS applied materials & interfaces, 9 (2017) 8201-8210.

[40] Q. Wang, H. Wu, Y. Wang, J. Li, Y. Yang, X. Cheng, Y. Luo, B. An, X. Pan, E. Xie, Ex-situ XPS analysis of yolk-shell Sb_2O_3/WO_3 for ultra-fast acetone resistive sensor, Journal of Hazardous Materials, 412 (2021) 125175.

[41] L. Cai, X. Dong, G. Wu, J. Sun, N. Chen, H. Wei, S. Zhu, Q. Tian, X. Wang, Q. Jing, Ultrasensitive acetone gas sensor can distinguish the diabetic state of people and its high performance analysis by first-principles calculation, Sensors and Actuators B: Chemical, 351 (2022) 130863.

[42] L. Jiang, K. Xue, Z. Chen, Q. Cui, S. Xu, High performance of gas sensor based on Bi-doped $ZnSnO_3$/CuO nanocomposites for acetone, Microporous and Mesoporous Materials, 329 (2022) 111532.

Chapter 6: Gas Sensing Performance of CuO-ZnO Composite

Introduction

Focusing on enhancing the detection of NO_2 below critical limits, the research explores the utilization of metal oxide nanostructures, with particular emphasis on CuO and the widely recognized sensing properties of ZnO. The study leads to the synthesis of CuO-ZnO composites using an innovative polyol technique, aiming to improve gas sensing performance through this structure formation.

6.1 Morphological properties

Figures 6.1a, b, and e–i present the distinct morphological characteristics of CuO, ZnO, CuO-ZnO_95 (the specific atomic ratio Zn:Cu is 0.95:0.05), and CuO-ZnO_90 (the specific atomic ratio Zn:Cu is 0.90:0.10) observed by field-emission scanning electron microscopy (FESEM). The morphology of the CuO powder is illustrated in Figures 6.1a and b. The low magnification SEM image displays a hierarchical structure composed of microspheres with an average diameter of 735.84 nm (Figures 6.1a and c). By examining high magnification SEM images, it is evident that microspheres consist of nanoparticles with an average particle size of 59.99 nm (Figures 6.1b and d). The morphology of the surfactant-free synthesized ZnO microstructure is shown in Figures 6.1e-g. The zinc oxide precursor powder before annealing is displayed in Figure 6.1e, while Figures 6.1f and g exhibit the porous structure of ZnO. Figure 6.1h demonstrates that the CuO-ZnO_95 powder morphology is similar to the ZnO one. On the other hand, CuO-ZnO_90 exhibits a structure consisting of sphere-like CuO and porous ZnO nanoparticles (Figure 6.1i). The CuO structure consists of nanometer-sized crystals that are arranged into larger micrometer-scale structures called microspheres (Figures 6.1a and b). These microspheres form during the polyol process, which minimizes surface energy by forming spherical precipitates. As time passes, these spherical particles dissolve slightly and then reform, gradually altering their shape. With a relatively low precursor concentration, there are only a few nucleation centers. The growth of new particles on the sphere's surface occurs slowly through diffusion. As this slow growth process continues, tiny particles attach to the nucleation centers on the original spherical particles' surface, leading to a change in shape and the formation of particles [1-4].

This 3D hierarchical structure offers a high specific surface area of CuO and facilitates the diffusion of analytes towards the surface. Figures 6.1f and g clearly show that the fabricated particles become porous structures after the thermal treatment. When ethylene glycol (EG) molecules are exposed to high temperatures, they produce OH^- ions that react with Zn^{2+} to form $Zn(OH)_2$ as an initial powder. During the phase transition from $Zn(OH)_2$ to ZnO, pores are formed, resulting in a high surface-to-volume ratio [5]. The ZnO porous structure is achieved without the use of any additives, making it a cost-effective, simple, and environmentally friendly method. To synthesize composite materials, both bare metal oxide precursors were prepared using the polyol method under the same conditions before calcination. Then, CuO and ZnO were mixed by heating at 100 °C with isopropyl alcohol as a solvent. The morphological properties of the composite structures were not significantly affected by the second step in the synthesis method due to the short reaction time.

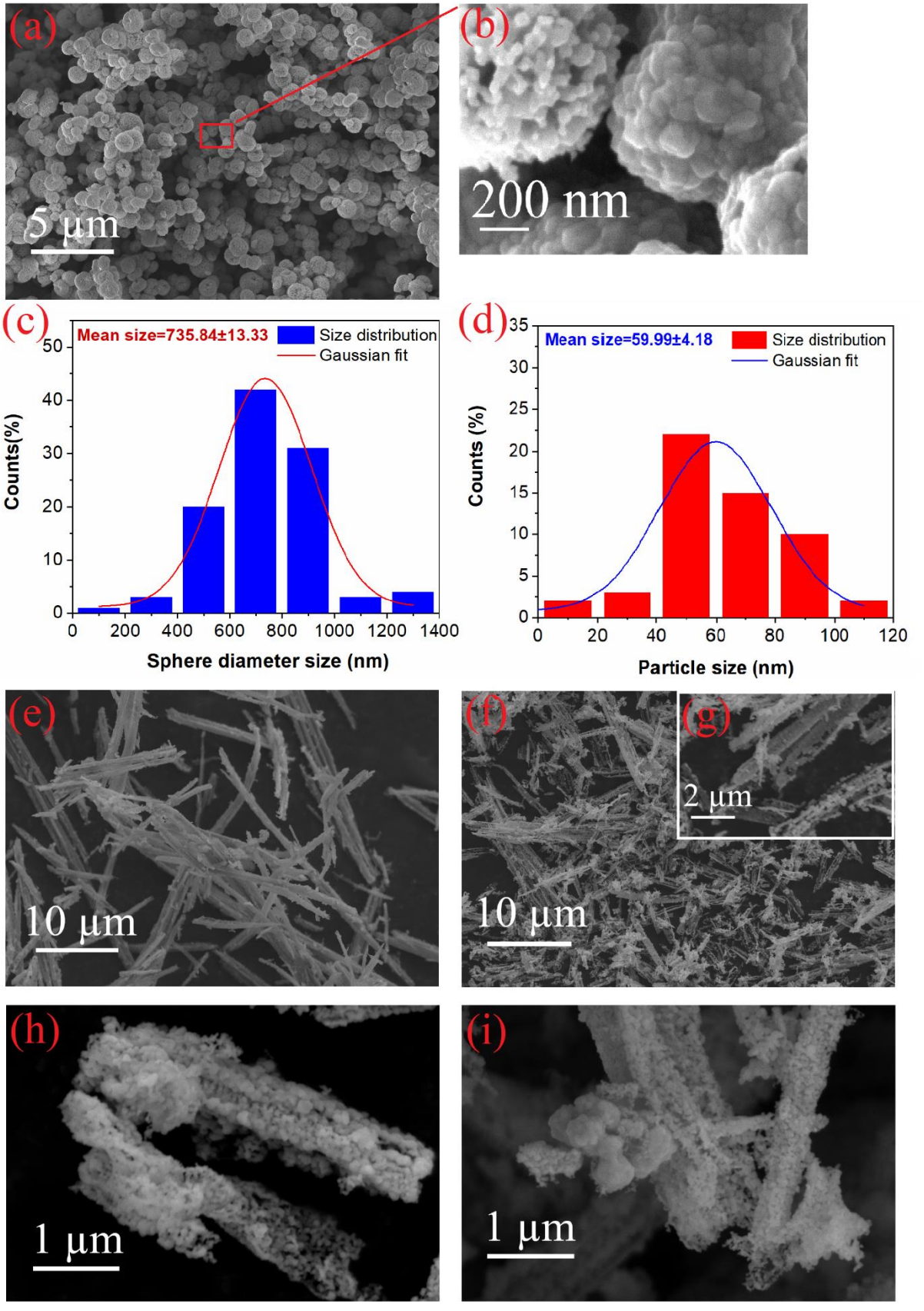
(a)
5 μm
(b)
200 nm
(c)
Mean size=735.84±13.33
Size distribution
Gaussian fit
Counts(%)
Sphere diameter size (nm)
(d)
Mean size=59.99±4.18
Size distribution
Gaussian fit
Counts (%)
Particle size (nm)
(e)
10 μm
(f)
10 μm
(g)
2 μm
(h)
1 μm
(i)
1 μm

Figure 6.1 FESEM images of prepared (a) and (b) CuO hierarchical structure synthesized using the polyol method, (c) and (d) size distribution histogram of obtained CuO microsphere and nanoparticles, SEM images of resultant (e) ZnO micro rod using EG as a solvent before calcination, (f) and (g) ZnO porous structure annealed at 500 °C Synthesized composite utilizing isopropyl alcohol, where the proportions of Zn and Cu weight are (h) 0.95:0.05 (CuO-ZnO_95) and (i) 0.9:0.1 (CuO-ZnO_90).

6.2 Structural properties

The X-ray diffraction spectroscopy was employed to investigate the crystal structures of CuO, ZnO, CuO-ZnO_95 and CuO-ZnO_90 (Figure 6.2). The synthesis process of CuO involves a two-step procedure: initially, copper acetate reacts with EG, producing organocopper precursors; subsequently, these precursors are annealed to prepare the CuO powder. It is noteworthy that the XRD pattern obtained from the calcinated sample of CuO confirms its crystallinity. Moreover, the diffraction pattern of the CuO structure corresponds to monoclinic (space group: C1 2/c 1, space group number:15, PDF No: 01-089-5897). Significantly, no additional peaks corresponding to secondary Cu or Cu_2O phases were detected.

The pattern of ZnO powder reveals its hexagonal crystalline structure (space group: P 63 m c, space group number: 186, PDF No: 01-079-2205). The diffraction peaks match well with the hexagonal structure and there are no secondary phases present. The diffraction peaks of CuO-ZnO composites are similar to pure ZnO, but there are a few peaks that correspond to the monoclinic CuO in the XRD pattern. When the organocopper precursor is added to the Zinc acetate precursor solution (CuO-ZnO_95 and CuO-ZnO_90), a peak appears at 38.73°, which corresponds to the (111) crystal plane of monoclinic CuO. Additionally, there are peaks at 66.3°, 68.03°, and 72.56°, which can be assigned to the (31-1), (220), and (311) planes of monoclinic CuO, as well as the (020), (112), and (004) planes of hexagonal ZnO, respectively. In the XRD pattern of CuO-ZnO_90, an additional peak at 35.46° was observed, which corresponds to the (11-1) plane of the CuO monoclinic structure. The intensity of the diffraction peak is enhanced as the organocopper precursor concentration increases.

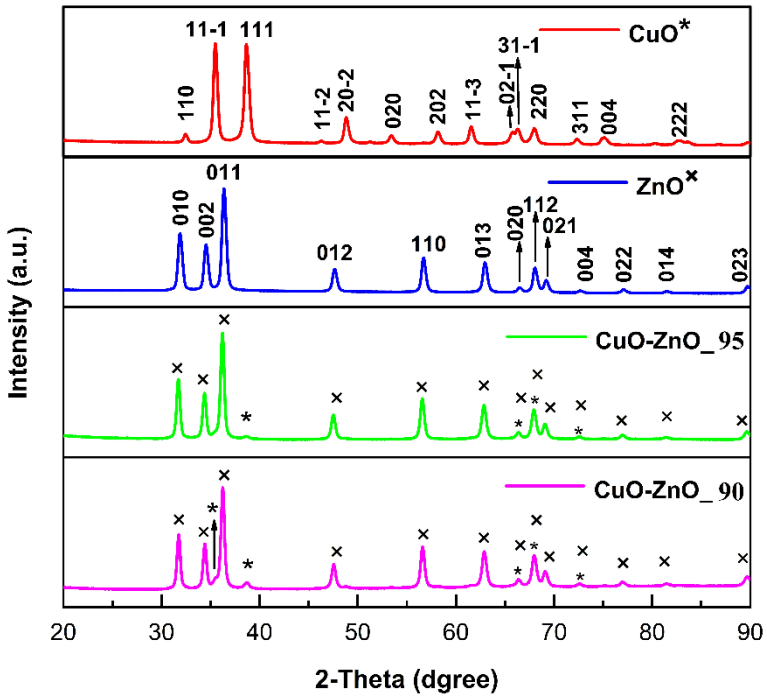

Figure 6.2 XRD pattern of CuO, ZnO, CuO-ZnO_95 and CuO-ZnO_90.

6.3 Optical properties

UV-vis spectroscopy was employed to assess the optical properties of the samples, aiming to calculate the band gap energy values for CuO, ZnO, CuO-ZnO_95, and CuO-ZnO_90. Band gap energy values were determined by analyzing the absorption data (as shown in Figure 6.3a) using Equation 1, where A is a constant, α represents the absorption coefficient, and hv corresponds to the energy of the incident photon [6]. The band gap (E_g) was then derived from a Tauc plot, plotting $(\alpha hv)^2$ against hv. The E_g value was determined by extending the linear portion of the plot until α reached 0 in Figure 6.3b. The obtained result revealed a direct band gap of approximately 1.25 eV for CuO, consistent with the reported data in Table 6.1 [7]. The calculated E_g of ZnO in Table 6.1 was 3.09 eV, which differs slightly from the band gap range of 3.2−3.4 eV reported in the literature [8]. The slight variation could be attributed to defects in the pure ZnO structure [9]. The calculated band gap energy values for CuO-ZnO_95 and CuO-ZnO_90 were

2.92 and 2.81 eV, respectively. The band gap value decreases as the concentration of CuO in the composite increases. The presence of Cu atoms in the ZnO lattice introduces defects that influence the band structure, resulting in a lower band gap energy for the CuO-ZnO composite [10-12]. This reduction in the band gap is attributed to an increased carrier concentration, which leads to a narrower band gap [13]. Conversely, the addition of CuO to ZnO can create more active sites on the material's surface. These sites play a role in facilitating the transfer of mass (molecules and atoms) and electrons between ZnO and CuO. This enhanced electron transfer plays a crucial role in reducing the band gap of the composite compared to the pristine samples [13]. The decrease in band gap suggests a higher electron transfer, which can enhance the gas sensing performance of the composite [14].

$$\alpha h\nu = A(h\nu - E_g)^{1/2} \quad (1)$$

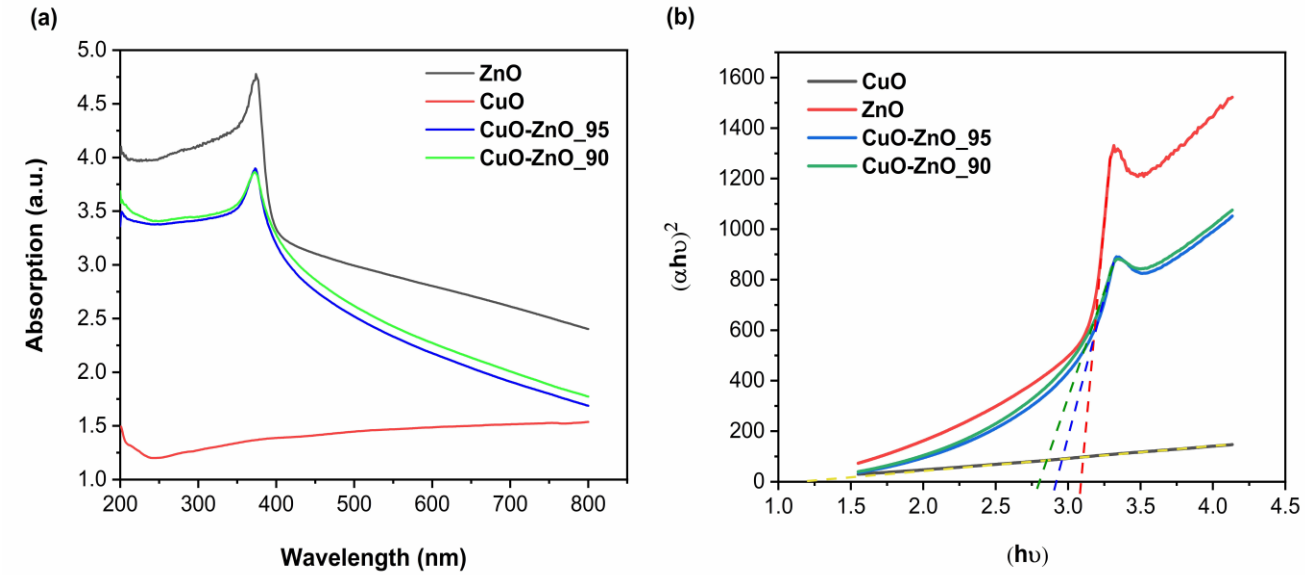

Figure 6.3 a) UV-vis absorbance spectra and b) Tauc's plot for band gap estimation of CuO, ZnO, CuO-ZnO_95 and CuO-ZnO_90.

Table 6.1 The band gap of ZnO, CuO, CuO-ZnO_95, CuO-ZnO_90.

Samples	Band gap (eV)
ZnO	3.09
CuO	1.25
CuO-ZnO_95	2.92
CuO-ZnO_90	2.81

6.4 Gas sensing performance

The adsorption/desorption reaction on the gas sensing material surface in conductometric sensors is greatly influenced by the operating temperatures. To investigate the gas sensing performances of CuO microsphere, ZnO structure, CuO-ZnO_95, and CuO-ZnO_90 composites, tests were conducted at temperatures ranging from 250 to 400 °C and 40% relative humidity. The gas sensing response of ZnO, CuO, CuO-ZnO_95, and CuO-ZnO_90 towards 5 ppm of NO_2 is shown in Figure 6.4. The results indicate that the gas sensing response increases as the operating temperature rises up to 350 °C, but decreases at 400 °C. Therefore, the maximum gas response occurs at 350 °C for ZnO, CuO-ZnO_95, and CuO-ZnO_90, while the highest response for CuO is observed at 250 °C.

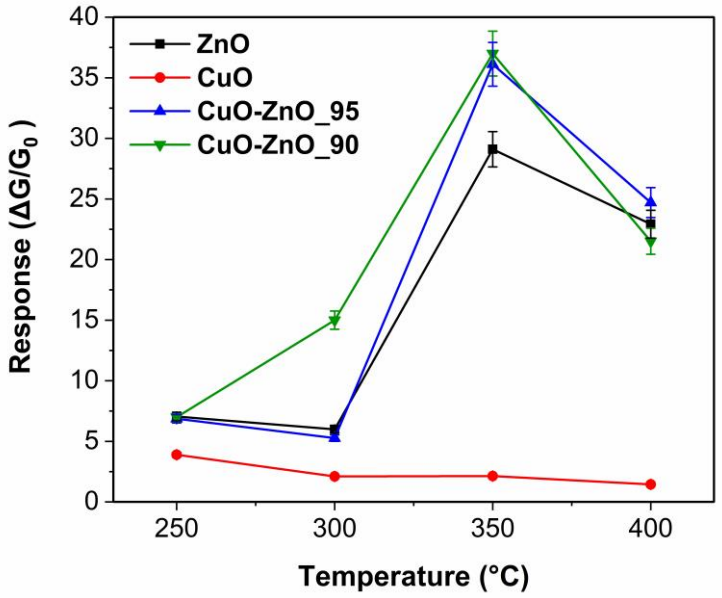

Figure 6.4 Gas sensing properties of pristine materials and their composite toward 5 ppm NO_2 at various temperatures.

Distinct behaviors in the dynamic responses of the four samples are evident in Figures 6.5a–d. The gas sensing measurements of materials were conducted toward various concentrations of NO_2 (1, 2, and 5 ppm) at their optimum operating temperature and 40% RH. First, the gas sensing material was exposed to the surrounding air environment, and then NO_2 was injected into the chamber. Finally, the test chamber was purified by restoring airflow. In Figure 6.4a, the conductance of ZnO, a typical n-type metal oxide, decreases upon exposure to NO_2 and returns to its baseline after airflow restoration. Similarly, the CuO-ZnO_95 and CuO-ZnO_90 composites show similar behaviors to ZnO nanomaterial due to the high percentage of ZnO (Figures 6.5c and d). In contrast, the increasing conductance of CuO confirms its p-type metal oxide behavior towards NO_2, which acts as an oxidizing gas (Figure 6.5b). Equations 2–5 demonstrate that oxygen molecules are adsorbed on the metal oxide surface, capturing electrons from the conduction band and forming oxygen ions on the material's surface [15, 16].

$$O_2(gas) \leftrightarrow O_2(ads) \quad (2)$$

$$O_2(ads) + e^- \leftrightarrow O_2^-(ads) \quad (3)$$

$$O_2^-(ads) + e^- \leftrightarrow 2O^-(ads) \quad (4)$$

$$O^{-}(ads) + e^{-} \leftrightarrow O^{2-}(ads) \quad (5)$$

When exposed to NO_2 gas, the nanostructures interact with the NO_2 molecules on their surface, resulting in redox reactions as shown in Equation 6. The NO_2 molecules that are adsorbed can capture electrons from the conduction band of the materials, leading to the formation of the species shown in Equation 7 [17, 18]. Furthermore, the NO_2 molecules, which have a higher electronegativity than oxygen, can react with oxygen species present on the surface (O^{2-} and O^{-}), as demonstrated in Equations 8 and 9 [18-20].

$$NO_2(gas) \rightarrow NO_2(ads) \quad (6)$$

$$NO_2(ads) + e^{-} \rightarrow NO_2^{-}(ads) \quad (7)$$

$$NO_2 + O_2^{-} + 2e^{-} \rightarrow NO_2^{-}(ads) + 2O^{-}(ads) \quad (8)$$

$$NO_2^{-}(ads) + 2O^{-}(ads) + e^{-} \rightarrow NO_2(gas) + 2O^{2-}(ads) \quad (9)$$

Figures 6.5a–d illustrate a significant increase in composite resistance (10^3 times) compared to the pristine material. This increase can be attributed to the band bending caused by the formation of a p-n junction at the surface of CuO and ZnO (the formation of a Zn–O–Cu bond) [21-24]. Additionally, the dynamic response of CuO-ZnO_95 and CuO-ZnO_90 shows a stable baseline and rapid recovery compared to the pristine materials. The addition of CuO nanospheres further enhances the response of the composite compared to CuO and ZnO shown in Figure 6.4. This enhancement can be related to the presence of more active sites, which increases the depletion layer and facilitates charge transfer [25, 26].

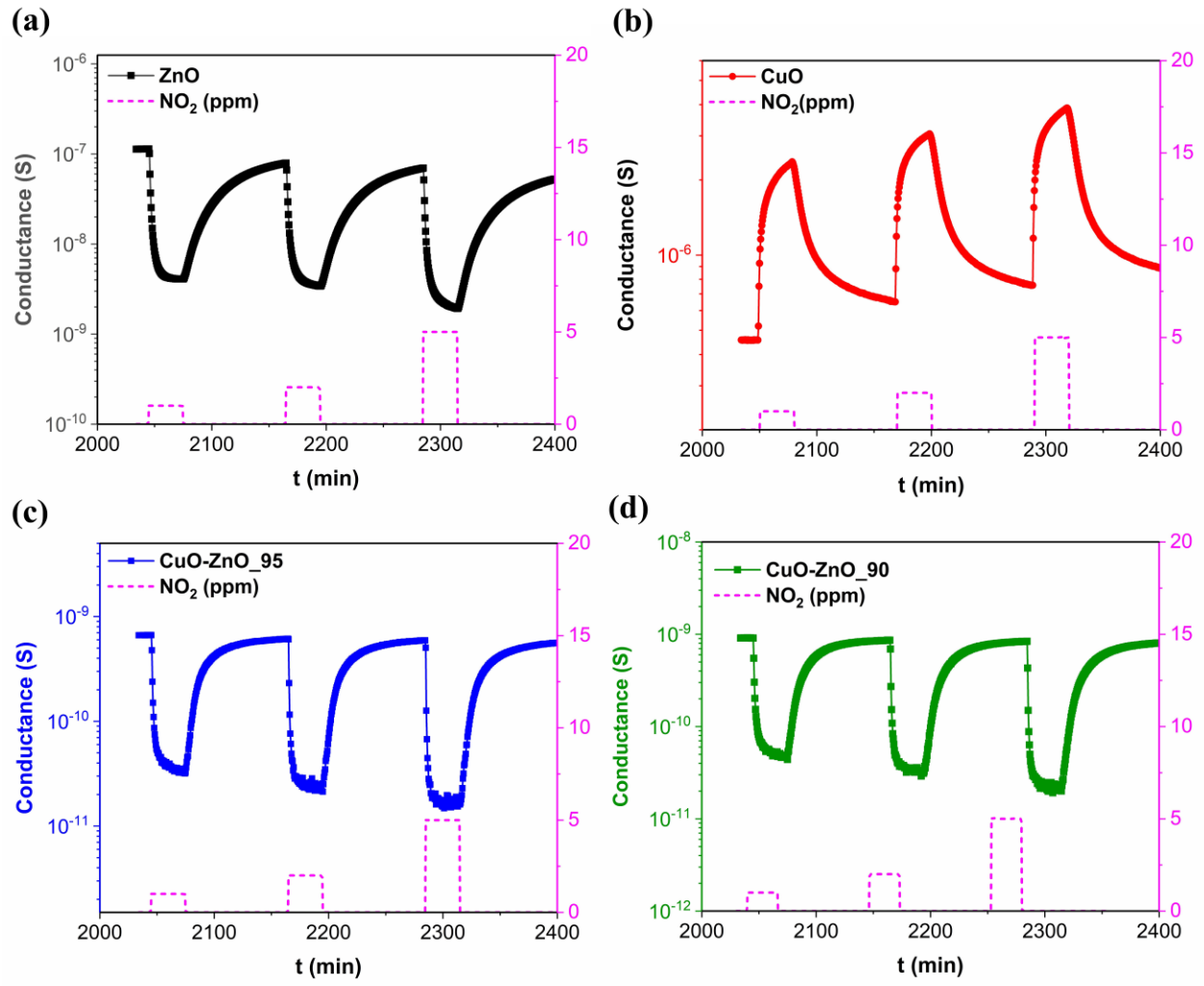

Figure 6.5 Dynamic response of a) ZnO, b) CuO, c) CuO-ZnO_95 and d) CuO-ZnO_90 toward 1, 2, 5 ppm NO_2 at their optimal operating temperature.

Figure 6.6a demonstrates the gas sensing performances of CuO-ZnO_90 and CuO-ZnO_95 towards various concentrations (0.1, 0.2, 0.5, 1, 2, and 5 ppm) of NO_2 at a temperature of 350 °C and a relative humidity of 40%. It is evident that the gas sensing response of the CuO-ZnO composites increases as the concentration of NO_2 increases. The results reported in Table 6.2 show a good response toward 100 ppb of NO_2, with response values of 1.6 and 1.2 for CuO-ZnO_95 and CuO-ZnO_90, respectively. Similarly, the response values of CuO-ZnO_95 and CuO-ZnO_90 toward 200 ppb are 3.3 and 2.8, respectively. Detecting low concentrations of NO_2 is crucial for environmental monitoring. Additionally, the threshold limit value (TLV) of NO_2 is defined 5 ppm, while the guidelines established by the Scientific Committee on Occupational

Exposure Limits (SCOEL) of the European Commission, which defines an 8-hour time-weighted average (TWA) and a short-term exposure limit (STEL) of 0.5 and 1 ppm, respectively [27-29].

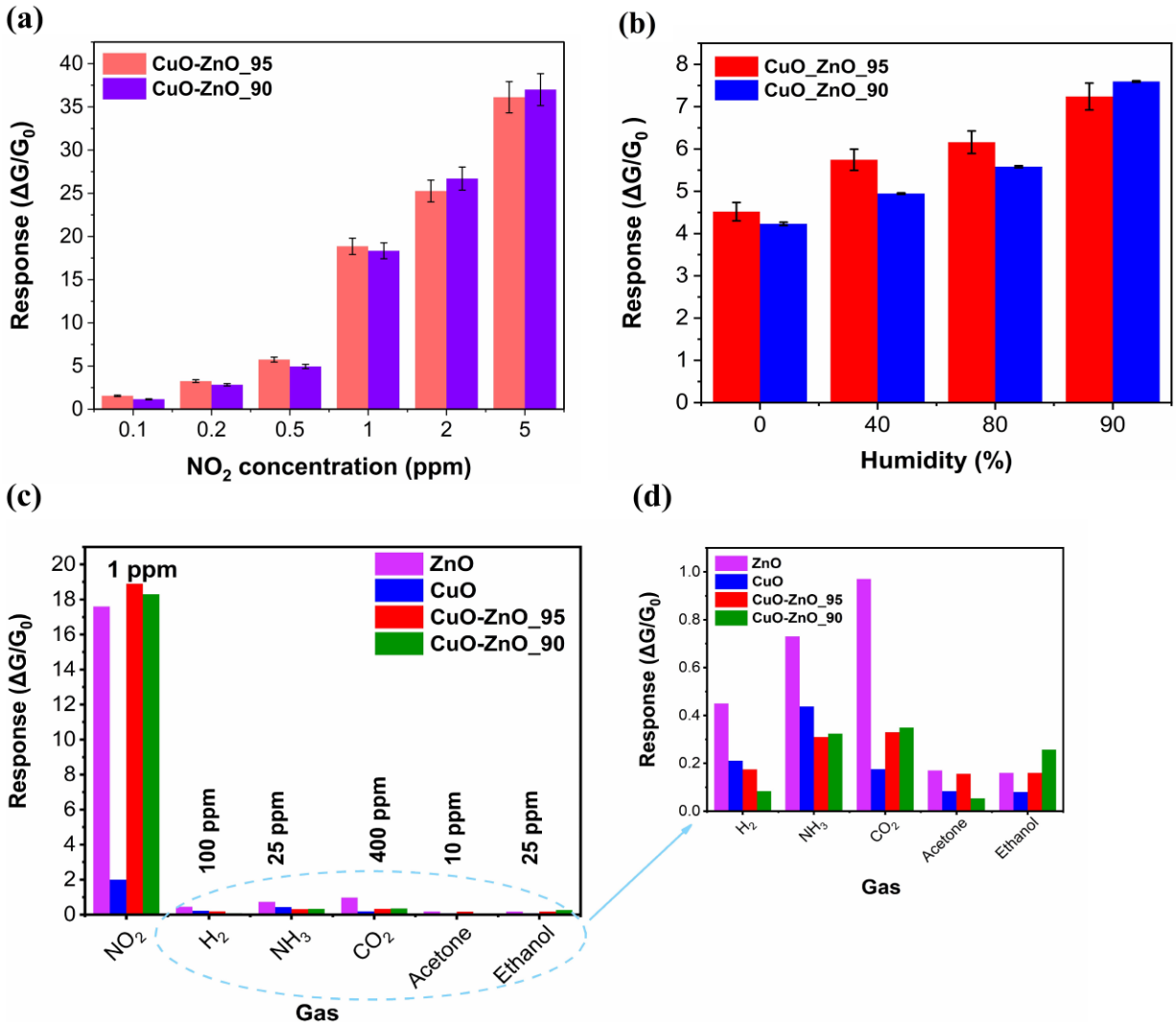

Figure 6.6 a) Response of CuO-ZnO_95 and CuO-ZnO_90 toward various concentrations of NO_2 (0.1−5 ppm) at an operating temperature of 350 °C, b) Gas sensing response of CuO-ZnO_95 and CuO-ZnO_90 to 500 ppb of NO_2 at different relative humidity levels (0-90%) and an operating temperature of 350 °C, c) Response of ZnO, CuO, CuO-ZnO_95 and CuO-ZnO_90 toward various analytes (NO_2, H_2, NH_3, CO_2, acetone and Ethanol) at 350 °C (40% RH) and d) A magnified section from Figure (c) where the response of four samples toward interfering gases (H_2, NH_3, CO_2, acetone, ethanol) can be seen.

Table 6.2 Response of CuO-ZnO_95 and CuO-ZnO_90 toward various concentrations of NO_2 at 350 °C.

Concentration	Response of CuO-ZnO_95	Response of CuO-ZnO_90
0.1	1.6	1.2
0.2	3.3	2.8
0.5	5.7	4.9
1	18.3	18.9
2	25.3	26.7
5	36.1	37

This study aims to investigate the effect of humidity on the performance of CuO-ZnO_95 and CuO-ZnO_90 gas sensors toward 500 ppb of NO_2 at an optimum operating temperature of 350 °C. Gas sensors were studied at different relative humidity (RH) ranging from 0 to 90%. By comparing the response of CuO-ZnO_95 and CuO-ZnO_90 sensors at different RH levels (Figure 6.6b), it is clear that humidity level has a slight effect on sensor performance. Increasing the RH from 0% to 40% resulted in a 27% increase in response for CuO-ZnO_95, while CuO-ZnO_90 showed a 17% increase. Moreover, when the RH was increased from 40% to 80%, the response of CuO-ZnO_95 and CuO-ZnO_90 increased by 7% and 13%, respectively. The response enhancement continued as the RH reached 90%. Figure 6.6b demonstrates that CuO-ZnO_95 had a 17% higher response. Similarly, CuO-ZnO_90 had a significant response enhancement of 35% at 90% RH compared to CuO-ZnO_95.

The influence of humidity on the electrical and gas sensing characteristics of materials is important, and this study contributes to a better understanding of this phenomenon. Examining the conductance behavior of composite materials at 350 °C (Figure 6.7a), it was observed that the conductance of CuO-ZnO_95 and CuO-ZnO_90 was slightly increased at 40% RH compared to dry air conditions. Remarkably, significant variations in conductance were not observed at

higher RH levels, ranging from 40% to 90%. These variations in response to humidity changes are ascribed to the dissociation of water molecules on the sensor's surface, leading to the formation of hydroxyl (OH^-) and proton (H^+) groups [30-32]. The presence of these protons can introduce additional electrons into the sensing mechanism, thereby influencing the response toward NO_2. It is important to note that the interaction between water molecules, other gaseous compounds, and the material surface is a complex process influenced by various factors, including operating conditions. Additionally, water may act as a catalyst for the interaction between the analyte and the material surface [33, 34]. Figure 6.7a demonstrates the consistent electrical conductance stability of both composites at 40–90% RH, with a slight increase in conductance from 0 to 40% RH. At high operating temperatures (350°C), the influence of water molecules is not significant due to their evaporation.

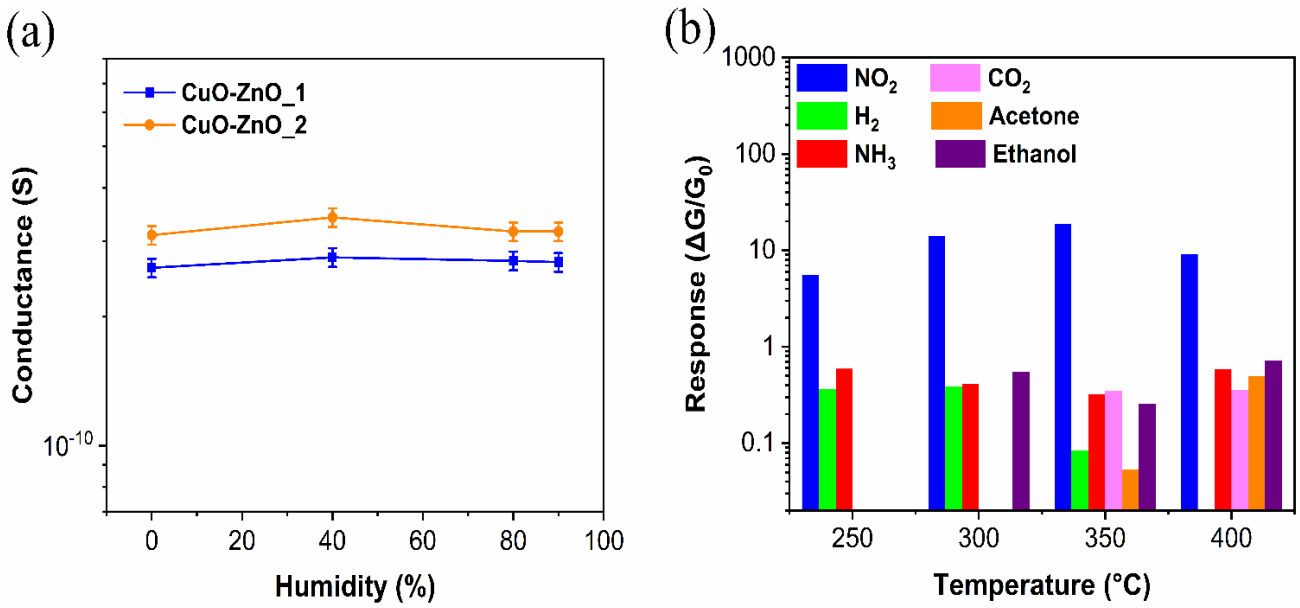

Figure 6.7 a) Conductance of CuO-ZnO_1 and CuO-ZnO_2 at different relative humidity (0-90%) and b) Response of CuO-ZnO_1 toward 1 ppm of NO_2, 100 ppm of H_2, 25 ppm of NH_3, 400 ppm of CO_2, 10 ppm of acetone and 25 ppm of ethanol.

Selectivity is a critical parameter in gas sensors. Therefore, the responses of the four samples to different gases were conducted (Figures 6.6c and d). The responses of the CuO, ZnO, CuO-ZnO_95 and CuO-ZnO_90 toward 100 ppm H_2, 25 ppm NH_3, 400 ppm CO_2, 10 ppm acetone, and 25 ppm ethanol were analyzed at 350 °C (Figure 6.6c). Figure 6.6d reveals that ZnO and CuO exhibited higher responses to hydrogen, ammonia, and carbon dioxide compared to the

composite. Furthermore, Figure 6.7b illustrates the response variation of the CuO-ZnO_90 sensor at different operating temperatures. The sensor exhibits high selectivity to NO_2 at various operating temperatures (250−400 °C) (Figure 6.7b). The remarkable selectivity of the four sensors towards NO_2 can be attributed to following detailed explanations. Firstly, NO_2, among various gases, shows remarkably low bond dissociation energy at 305.0 kJ/mol, compared to other gases (436 kJ/mol for H_2, 391.0 kJ/mol for NH_3, 532 kJ/mol for CO_2, 798.9 kJ/mol for acetone, and 441.0 kJ/mol for ethanol) (Table 6.3) [35-38]. This lower value justifies that the dissociation of NO_2 molecules on the sensor's surface requires less energy than other interfering gases, providing a favorable reaction between gas sensing material and NO_2. Furthermore, the increased reactivity of the four gas sensing materials to NO_2 compared to reducing gases can be explained by the higher electron affinity of NO_2 gas molecules (2.21 eV) [39], even larger than the electron affinity of CO_2 as an oxidizing gas (0.6 eV) [40]. Finally, the excellent selectivity of gas sensors toward NO_2 is attributed to the acid-base characteristics of the sensors. ZnO and CuO exhibit strong basic and weak basic properties, respectively [27, 41]. Generally, sites with acidic properties facilitate the adsorption of reducing gases (which are primarily basic), while sites with basic properties promote the adsorption of acidic gases like NO_2 [27]. In all sensing materials, the dominant basic properties result in a higher response toward NO_2. Hence, the sensors' high selectivity arises from the combination of the lower energy requirement for NO_2 dissociation, the elevated electron affinity of NO_2, and the basic properties of the sensor materials favoring the adsorption of acidic gases like NO_2. The superior selectivity to NO_2 confirms its potential practical application. Both composites effectively demonstrate higher response compared to other gases, even at higher concentrations than NO_2, which is a desirable characteristic for NO_2 sensors.

Table 6.3 Bond energy of tested gas molecules [35-38].

Gas	**NO_2**	**H_2**	**NH_3**	**CO_2**	**Acetone**	**Ethanol**
Bond	O–NO	H–H	$H–NH_2$	O–CO	$H–CH_2COCH_3$	$H–OC_2H_5$
Bond energy (KJ/mole)	305.0	436.0	391.0	532.0	798.9	441.0

Table 6.4 illustrates the gas sensing performance of different materials toward NO_2 at their optimum operating temperatures. Direct comparisons with other materials are challenging due to variations in measurement conditions. Nevertheless, these findings validate the excellent gas sensing properties achieved for NO_2 at 350 °C. Notably, the developed gas sensors exhibit higher responses even at lower concentrations of NO_2 compared to the outcomes reported in previous studies.

Table 6.4 Comparison of gas sensing response of CuO- ZnO_90 toward NO_2 with literature.

Sensing materials	Operating temperature (℃)	Concentration (ppm)	Response	Ref.
CuO NPs	150	40	0.03 $(R_0-R_f)/R_f$	[42]
ZnO/g-C_3N_4 nanocomposite	200	10	14.63$(R_f-R_0)/R_0$	[43]
ZnO–CuO core–shell nanorods	300	10	1.5 $(R_0-R_f)/R_f$	[44]
ZnO nanowire/CuO nanoparticle	150	100	1.75 $(R_f-R_0)/R_0$	[25]
CuO-ZnO laminated heterostructure	350	29	9.2 (R_0/R_f)	[45]
CuO-ZnO nanocomposite	200	100	0.73 (R_f/R_0)	[11]
hierarchical CuO-Co_3O_4 spheres	160	20	0.48 (R_f-R_0/R_0)	[46]
MoS_2-ZnO nanowires	200	50	0.31 (R_f-R_0/R_0)	[47]
ZnO/rGO/Au hybrids	80	100	0.33 $(R_0-R_f)/R_f$	[48]
nanoporous CuO@ZnO	RT	5	3.37 $(R_0-R_f)/R_f$	[49]
CuO nanowires/ZnO NPs	250	200	4.1 (R_0/R_f)	[50]
Cu:ZnO thin film	200	100	3.26 $(R_f-R_0)/R_0$	[51]
ZnO nanorods	200	1	1.31 $(I_0-I_f)/I_f$	[52]
Ce doped ZnO nanoarray	250	10	34.3 (R_f/R_0)	[53]
Pt/ZnO/g-C_3N_4	150	10	53 (R_f/R_0)	[54]
CuO-ZnO_90	400	1	9.2 $(G_0-G_f)/G_f$	This work

CuO-ZnO_90	350	1	18.9 $(G_0-G_f)/G_f$	This work
CuO-ZnO_90	300	1	14.1 $(G_0-G_f)/G_f$	This work
CuO-ZnO_90	250	1	5.6 $(G_0-G_f)/G_f$	This work

Note: I_0: Current of sensor in air, I_f: Current of sensor in gas, R_0: Resistance of sensor in air and R_f: Resistance of sensor in gas.

Conclusion

In summary, the study explores CuO-ZnO composites for gas sensing applications, detailing their morphological, structural, and optical characteristics. The sensors exhibited excellent selectivity to NO_2 at 350 °C, demonstrating superior performance even at low concentrations. These findings confirm the potential of CuO-ZnO composites for practical environmental monitoring, offering enhanced gas sensing properties.

References

[1] A.-M. Cao, J.-S. Hu, H.-P. Liang, W.-G. Song, L.-J. Wan, X.-L. He, X.-G. Gao, S.-H. Xia, Hierarchically Structured Cobalt Oxide (Co_3O_4): The Morphology Control and Its Potential in Sensors, The Journal of Physical Chemistry B, 110 (2006) 15858-15863.
[2] J. Liu, X. Huang, Y. Li, K.M. Sulieman, X. He, F. Sun, Hierarchical nanostructures of cupric oxide on a copper substrate: controllable morphology and wettability, Journal of Materials Chemistry, 16 (2006) 4427-4434.
[3] L. Suber, I. Sondi, E. Matijević, D.V. Goia, Preparation and the mechanisms of formation of silver particles of different morphologies in homogeneous solutions, Journal of Colloid and Interface Science, 288 (2005) 489-495.
[4] A.-m. Cao, J.D. Monnell, C. Matranga, J.-m. Wu, L.-l. Cao, D. Gao, Hierarchical Nanostructured Copper Oxide and Its Application in Arsenic Removal, The Journal of Physical Chemistry C, 111 (2007) 18624-18628.
[5] T. Ghoshal, S. Kar, S. Chaudhuri, ZnO Doughnuts: Controlled Synthesis, Growth Mechanism, and Optical Properties, Crystal Growth & Design, 7 (2007) 136-141.

[6] P. Makuła, M. Pacia, W. Macyk, How to correctly determine the band gap energy of modified semiconductor photocatalysts based on UV–Vis spectra, ACS Publications, 2018, pp. 6814-6817.
[7] M. Mashock, K. Yu, S. Cui, S. Mao, G. Lu, J. Chen, Modulating gas sensing properties of CuO nanowires through creation of discrete nanosized p–n junctions on their surfaces, ACS applied materials & interfaces, 4 (2012) 4192-4199.
[8] R.E. Marotti, P. Giorgi, G. Machado, E.A. Dalchiele, Crystallite size dependence of band gap energy for electrodeposited ZnO grown at different temperatures, Solar Energy Materials and Solar Cells, 90 (2006) 2356-2361.
[9] F.K. Shan, Y.S. Yu, Band gap energy of pure and Al-doped ZnO thin films, Journal of the European Ceramic Society, 24 (2004) 1869-1872.
[10] N. Datta, N.S. Ramgir, S. Kumar, P. Veerender, M. Kaur, S. Kailasaganapathi, A.K. Debnath, D.K. Aswal, S.K. Gupta, Role of various interfaces of CuO/ZnO random nanowire networks in H_2S sensing: An impedance and Kelvin probe analysis, Sensors and Actuators B: Chemical, 202 (2014) 1270-1280.
[11] S.M. Mali, S.S. Narwade, Y.H. Navale, S.B. Tayade, R.V. Digraskar, V.B. Patil, A.S. Kumbhar, B.R. Sathe, Heterostructural CuO–ZnO Nanocomposites: A Highly Selective Chemical and Electrochemical NO_2 Sensor, ACS Omega, 4 (2019) 20129-20141.
[12] M.T. Qamar, M. Aslam, I.M.I. Ismail, N. Salah, A. Hameed, Synthesis, Characterization, and Sunlight Mediated Photocatalytic Activity of CuO Coated ZnO for the Removal of Nitrophenols, ACS Applied Materials & Interfaces, 7 (2015) 8757-8769.
[13] A.M.M. Musa, M. Rasadujjaman, M.A. Gafur, A.T.M.K. Jamil, Synthesis and characterization of dip-coated ZnO–CuO composite thin film for room-temperature CO_2 gas sensing, Thin Solid Films, 773 (2023) 139838.
[14] K.G. Krishna, S.R. Parne, P. Nagaraju, An optical study of heterojunction n-ZnO/p-CuO nanosheets and detection of n-butanol vapour at room temperature, Journal of Materials Science, 58 (2023) 15660-15675.
[15] M.J. Madou, S.R. Morrison, 10 - Thin-Film Gas Sensors, in: M.J. Madou, S.R. Morrison (Eds.) Chemical Sensing with Solid State Devices, Academic Press, San Diego, 1989, pp. 419-435.
[16] M.J. Madou, S.R. Morrison, 3 - Solid/Gas Interfaces, in: M.J. Madou, S.R. Morrison (Eds.) Chemical Sensing with Solid State Devices, Academic Press, San Diego, 1989, pp. 67-104.
[17] Y. Zhong, W. Li, X. Zhao, X. Jiang, S. Lin, Z. Zhen, W. Chen, D. Xie, H. Zhu, High-response room-temperature NO_2 sensor and ultrafast humidity sensor based on SnO_2 with rich oxygen vacancy, ACS applied materials & interfaces, 11 (2019) 13441-13449.
[18] H. Bai, H. Guo, J. Wang, Y. Dong, B. Liu, Z. Xie, F. Guo, D. Chen, R. Zhang, Y. Zheng, A room-temperature NO_2 gas sensor based on CuO nanoflakes modified with rGO nanosheets, Sensors and Actuators B: Chemical, 337 (2021) 129783.
[19] V.L. Patil, S.S. Kumbhar, S.A. Vanalakar, N.L. Tarwal, S.S. Mali, J.H. Kim, P.S. Patil, Gas sensing properties of 3D mesoporous nanostructured ZnO thin films, New Journal of Chemistry, 42 (2018) 13573-13580.
[20] A. Govind, P. Bharathi, M.K. Mohan, J. Archana, S. Harish, M. Navaneethan, Highly sensitive near room temperature operable NO_2 gas-sensor for enhanced selectivity via nanoporous CuO@ZnO heterostructures, Journal of Environmental Chemical Engineering, 11 (2023) 110056.
[21] X. Wang, S. Li, L. Xie, X. Li, D. Lin, Z. Zhu, Low-temperature and highly sensitivity H_2S gas sensor based on ZnO/CuO composite derived from bimetal metal-organic frameworks, Ceramics International, 46 (2020) 15858-15866.
[22] Y. Chen, Z. Shen, Q. Jia, J. Zhao, Z. Zhao, H. Ji, A CuO–ZnO nanostructured p–n junction sensor for enhanced N-butanol detection, RSC Advances, 6 (2016) 2504-2511.
[23] F. Shao, M.W.G. Hoffmann, J.D. Prades, R. Zamani, J. Arbiol, J.R. Morante, E. Varechkina, M. Rumyantseva, A. Gaskov, I. Giebelhaus, T. Fischer, S. Mathur, F. Hernández-Ramírez, Heterostructured p-

CuO (nanoparticle)/n-SnO_2 (nanowire) devices for selective H_2S detection, Sensors and Actuators B: Chemical, 181 (2013) 130-135.
[24] S. Zhao, Y. Shen, F. Hao, C. Kang, B. Cui, D. Wei, F. Meng, P-n junctions based on CuO-decorated ZnO nanowires for ethanol sensing application, Applied Surface Science, 538 (2021) 148140.
[25] Y.H. Navale, S.T. Navale, F.J. Stadler, N.S. Ramgir, V.B. Patil, Enhanced NO_2 sensing aptness of ZnO nanowire/CuO nanoparticle heterostructure-based gas sensors, Ceramics International, 45 (2019) 1513-1522.
[26] D.R. Miller, S.A. Akbar, P.A. Morris, Nanoscale metal oxide-based heterojunctions for gas sensing: A review, Sensors and Actuators B: Chemical, 204 (2014) 250-272.
[27] Y.J. Kwon, S.Y. Kang, A. Mirzaei, M.S. Choi, J.H. Bang, S.S. Kim, H.W. Kim, Enhancement of gas sensing properties by the functionalization of ZnO-branched SnO_2 nanowires with Cr_2O_3 nanoparticles, Sensors and Actuators B: Chemical, 249 (2017) 656-666.
[28] C.D. Burgess, L.S. Levy, CEC SCIENTIFIC EXPERT GROUP ON OCCUPATIONAL EXPOSURE LIMITS—A REVIEW OF PROGRESS 1990–1991, The Annals of Occupational Hygiene, 35 (1991) 453-455.
[29] D. Matatagui, J. Lopez-Sanchez, A. Pena, A. Serrano, A. Del Campo, O.R. de la Fuente, N. Carmona, E. Navarro, P. Marin, M. del Carmen Horrillo, Ultrasensitive NO_2 gas sensor with insignificant NH_3-interference based on a few-layered mesoporous graphene, Sensors and Actuators B: Chemical, 335 (2021) 129657.
[30] N. Agmon, The Grotthuss mechanism, Chemical Physics Letters, 244 (1995) 456-462.
[31] D.S. Vlachos, P.D. Skafidas, J.N. Avaritsiotis, The effect of humidity on tin-oxide thick-film gas sensors in the presence of reducing and combustible gases, Sensors and Actuators B: Chemical, 25 (1995) 491-494.
[32] V. Galstyan, N. Poli, A. D'Arco, S. Macis, S. Lupi, E. Comini, A novel approach for green synthesis of WO_3 nanomaterials and their highly selective chemical sensing properties, Journal of Materials Chemistry A, 8 (2020) 20373-20385.
[33] J.F. Boyle, K.A. Jones, The effects of CO, water vapor and surface temperature on the conductivity of a SnO2 gas sensor, Journal of Electronic Materials, 6 (1977) 717-733.
[34] H. Pakdel, V. Galstyan, A. D'Arco, T. Mancini, S. Lupi, A. Moumen, M. Borsi, E. Comini, Synthesis of WO_3 nanopowder using a green surfactant for efficient gas sensing applications, Ceramics International, 49 (2023) 30501-30509.
[35] J.H. Bang, M.S. Choi, A. Mirzaei, Y.J. Kwon, S.S. Kim, T.W. Kim, H.W. Kim, Selective NO_2 sensor based on Bi_2O_3 branched SnO_2 nanowires, Sensors and Actuators B: Chemical, 274 (2018) 356-369.
[36] J. Shi, Z. Cheng, L. Gao, Y. Zhang, J. Xu, H. Zhao, Facile synthesis of reduced graphene oxide/hexagonal WO_3 nanosheets composites with enhanced H_2S sensing properties, Sensors and Actuators B: Chemical, 230 (2016) 736-745.
[37] D. Zhang, Morphology genetic materials templated from nature species, Springer Science & Business Media2014.
[38] T.V.K. Karthik, H. Martínez-García, F. Ortiz-Chi, C.G. Espinosa-González, J.G. Torres-Torres, A.G. Hernandez, S. Godavarthi, M.K. Kesarla, CO_2 gas sensing properties of graphitic carbon nitride (g-C_3N_4) thin films, Diamond and Related Materials, 133 (2023) 109736.
[39] Z. Liu, L. Yu, F. Guo, S. Liu, L. Qi, M. Shan, X. Fan, Facial development of high performance room temperature NO_2 gas sensors based on ZnO nanowalls decorated rGO nanosheets, Applied Surface Science, 423 (2017) 721-727.
[40] R.N. Compton, P.W. Reinhardt, C.D. Cooper, Collisional ionization of Na, K, and Cs by CO_2, COS, and CS_2: Molecular electron affinities, The Journal of Chemical Physics, 63 (2008) 3821-3827.
[41] N.J. Abreu, H. Valdés, C.A. Zaror, T.F. de Oliveira, F. Azzolina-Jury, F. Thibault-Starzyk, Evidence of Synergy Effects between Zinc and Copper Oxides with Acidic Sites on Natural Zeolite during Photocatalytic Oxidation of Ethylene Using Operando DRIFTS Studies, Catalysts, 2023.

[42] A. Das, B. Venkataramana, D. Partheephan, A.K. Prasad, S. Dhara, A.K. Tyagi, Facile synthesis of nanostructured CuO for low temperature NO_2 sensing, Physica E: Low-dimensional Systems and Nanostructures, 54 (2013) 40-44.
[43] D. Simon Patrick, A. Govind, P. Bharathi, M. Krishna Mohan, S. Harish, J. Archana, M. Navaneethan, Hierarchical ZnO/g-C_3N_4 nanocomposites for enhanced NO_2 gas sensing applications, Applied Surface Science, 609 (2023) 155337.
[44] C. Jin, H. Kim, S. Park, S.-W. Choi, S.S. Kim, C. Lee, NO_2 gas sensing properties of ZnO sheathed CuO nanorods, Surface and Interface Analysis, 44 (2012) 1534-1537.
[45] L. Yang, C. Xie, G. Zhang, J. Zhao, X. Yu, D. Zeng, S. Zhang, Enhanced response to NO_2 with CuO/ZnO laminated heterostructured configuration, Sensors and Actuators B: Chemical, 195 (2014) 500-508.
[46] H. Fang, S. Li, H. Zhao, J. Deng, D. Wang, J. Li, Enhanced NO_2 gas sensing performance by hierarchical CuO–Co_3O_4 spheres, Sensors and Actuators B: Chemical, 352 (2022) 131068.
[47] S. Zhao, G. Wang, J. Liao, S. Lv, Z. Zhu, Z. Li, Vertically aligned MoS_2/ZnO nanowires nanostructures with highly enhanced NO_2 sensing activities, Applied Surface Science, 456 (2018) 808-816.
[48] S. Liu, Z. Wang, Y. Zhang, Z. Dong, T. Zhang, Preparation of zinc oxide nanoparticle–reduced graphene oxide–gold nanoparticle hybrids for detection of NO_2, RSC Advances, 5 (2015) 91760-91765.
[49] A. Govind, P. Bharathi, M.K. Mohan, J. Archana, S. Harish, M. Navaneethan, Highly sensitive near room temperature operable NO_2 gas-sensor for enhanced selectivity via nanoporous CuO@ZnO heterostructures, Journal of Environmental Chemical Engineering, (2023) 110056.
[50] T.-H. Han, S.-Y. Bak, S. Kim, S.H. Lee, Y.-J. Han, M. Yi, Decoration of CuO NWs Gas Sensor with ZnO NPs for Improving NO_2 Sensing Characteristics, Sensors, 2021.
[51] V.S. Kamble, R.K. Zemase, R.H. Gupta, B.D. Aghav, S.A. Shaikh, J.M. Pawara, S.K. Patil, S.T. Salunkhe, Improved toxic NO_2 gas sensing response of Cu-doped ZnO thin-film sensors derived by simple co-precipitation route, Optical Materials, 131 (2022) 112706.
[52] Y. Şahin, S. Öztürk, N. Kılınç, A. Kösemen, M. Erkovan, Z.Z. Öztürk, Electrical conduction and NO_2 gas sensing properties of ZnO nanorods, Applied Surface Science, 303 (2014) 90-96.
[53] K. Sun, G. Zhan, L. Zhang, Z. Wang, S. Lin, Highly sensitive NO_2 gas sensor based on ZnO nanoarray modulated by oxygen vacancy with Ce doping, Sensors and Actuators B: Chemical, 379 (2023) 133294.
[54] H. Tian, H. Fan, J. Ma, Z. Liu, L. Ma, S. Lei, J. Fang, C. Long, Pt-decorated zinc oxide nanorod arrays with graphitic carbon nitride nanosheets for highly efficient dual-functional gas sensing, Journal of hazardous materials, 341 (2018) 102-111.

Chapter 7: The electrochemical properties of V_2O_5 as anode material of Li-ion batteries

Introduction

This chapter explores the electrochemical properties of V_2O_5 microsheets, focusing on their potential as anode materials for lithium-ion batteries. Through structural and morphological characterizations and detailed analyses of charge/discharge behaviors, the study aims to elucidate the performance and mechanisms underlying the promising application of V_2O_5 microsheets in high-performance energy storage devices.

7.1 Structural properties

The structural properties of vanadium oxide precursor, V_2O_5_60 and V_2O_5_80 were investigated using XRD (Figures 7.1a and b). The X-ray diffraction pattern in Figure 7.1a illustrates the crystal phase of the vanadium oxide precursor before annealing, revealing the coexistence of ammonium trivanadate (V) ($NH_4(V_3O_8)$) and duttonite vanadium oxide (V_4O_{10}). The XRD pattern further demonstrates that most diffraction peaks can be indexed to the monoclinic $NH_4(V_3O_8)$ phase (Reference code. 98-005-0492, Space group: P 1 21/m 1, Space group number: 11). Furthermore, a few peaks match well with the monoclinic duttonite vanadium oxide (V_4O_{10}) (Reference code. 96-901-1015, space group: C 1 2/c 1, space group number: 15), but their diffraction intensity is weak compared to the monoclinic $NH_4(V_3O_8)$ phase. All diffraction peaks of V_2O_5_60 and V_2O_5_80 are assigned to the crystalline orthorhombic V_2O_5 phase (Reference code. 98-008-0861, space group: Pmmn, space group number: 59) without any further crystalline phase. As shown in Figure 7.1b, the narrow and sharp peaks exhibit a high crystallinity of the prepared samples.

The Williamson-Hall formula was employed to calculate the crystallite size of V_2O_5_60 and V_2O_5_80 [1], determining the crystallite sizes to be 40 and 49 nm, respectively. The results indicate an increase in crystallite size with higher synthesis temperatures, a phenomenon attributed to Ostwald ripening and oriented attachment [2].

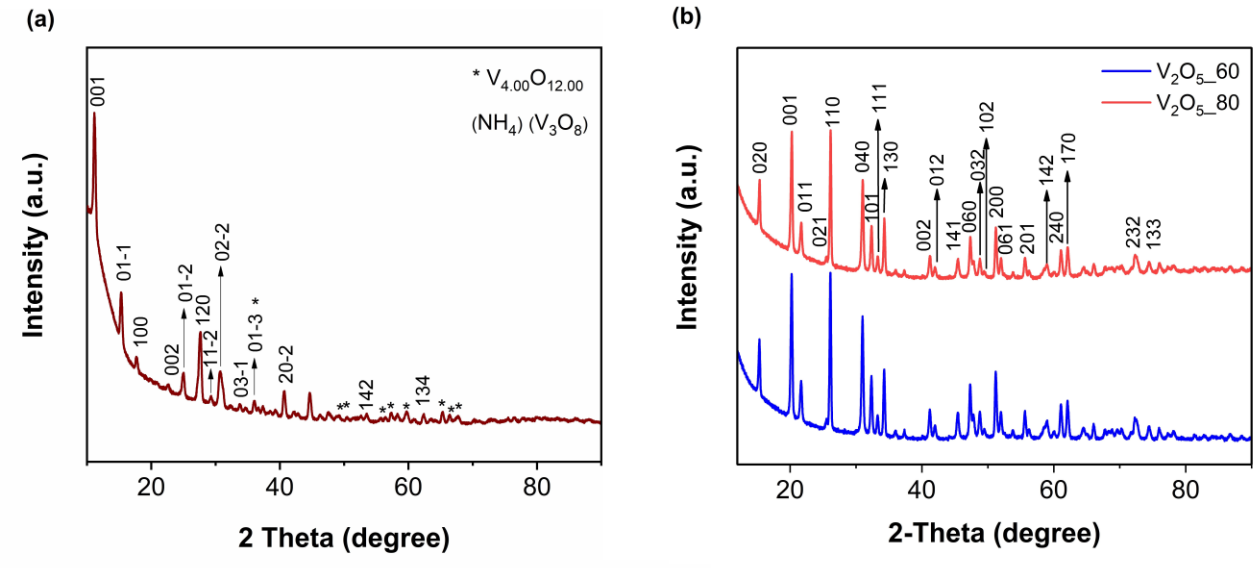

Figure 7.1 The XRD pattern of a) Vanadium oxide precursor before calcination at the reaction temperature of 60 °C and b) V_2O_5_60 and V_2O_5_80 powder prepared at a reaction temperature of 60 and 80 °C, respectively.

7.2 Morphological properties

The morphologies of vanadium oxide precursor, V_2O_5_60 and V_2O_5_80 were characterized using field-emission scanning electron microscopy (FESEM) and transmission electron microscopy (TEM). As shown in Figure 7.2a, the $NH_4V_3O_8$ and V_4O_{10} powder, were initially prepared at 60 °C before the annealing step, consists of sheets without any pores. Figure 7.2b displays the porous V_2O_5_60 microsheet prepared at a reaction temperature of 60 °C. The obtained result exhibits the porous micro sheet structure for V_2O_5_80 synthesized at 80 °C (Figures 7.2c and d).

The SEM analysis reveals that the morphology of synthesized vanadium oxide precursor is closely similar to the porous V_2O_5 microsheets. This suggests that heat treatment has a slight effect on the final morphology of sample. The annealing process primarily results in the conversion of $NH_4V_3O_8$ to V_2O_5, leading to the formation of porous structures (Figures 7.2a and b). Throughout the transformation from $NH_4V_3O_8$ to its oxide forms, internally generated NH_3 is released. Initially, the vanadium oxide layers prevent gas release, but then they fracture, allowing the trapped ammonia to be released. Simultaneously, small voids and pores are

generated. These processes occur continuously, progressing from the outer to the inner regions of sheets until $NH_4V_4O_{10}$ is entirely converted into porous V_2O_5. The decoration uniformity of V_2O_5 micro sheets is enhanced with an increasing reaction temperature from 60 °C to 80 °C, and the size of the sheet increases with the reaction temperature.

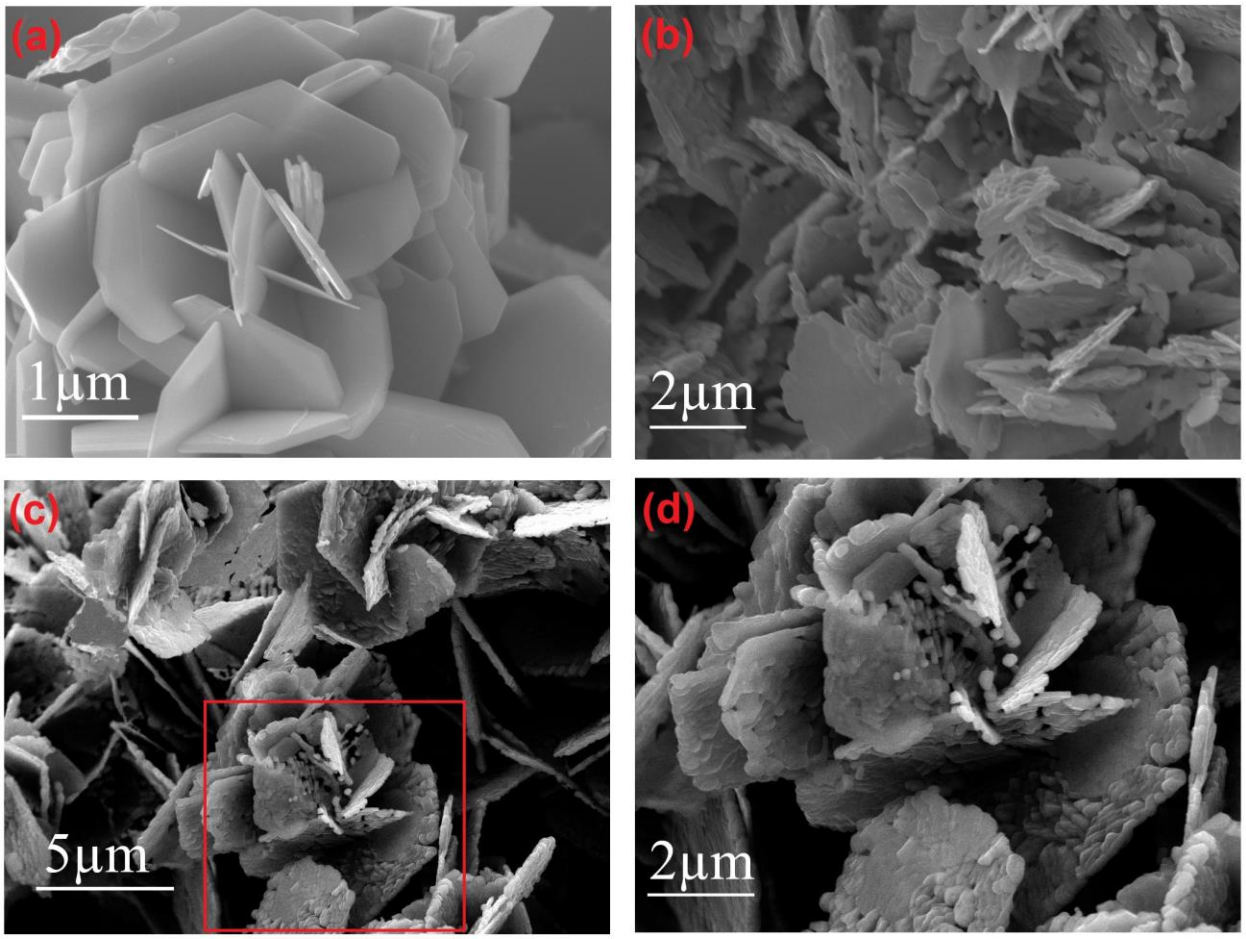

Figure 7.2 SEM image of a) Vanadium oxide precursor before annealing, b) V_2O_5_60 synthesized at a reaction temperature of 60 °C following the calcination temperature of 500 °C, c) V_2O_5_80 fabricated at a reaction temperature of 80 °C and annealed at 500 °C and d) A magnified section from Figure (c) (the area marked in the red square).

The TEM image representative of the V_2O_5_60 and V_2O_5_80 microsheets (Figures 7.3a and d) illustrates their porous structure. To examine the microstructure of both samples, high-resolution transmission electron microscopy (HRTEM) was utilized (Figures 7.3b and c). The lattice fringes presented in Figures 7.3b and c reveal the (020) and (040) facets of the orthorhombic V_2O_5_60 phase, respectively. This result indicates the high crystallinity of the

prepared V_2O_5_60 microsheets. The HRTEM image, displayed in Figures 7.3e and f, reveals a lattice fringe measuring 0.57 and 0.26 nm, corresponding to the (020) and (130) planes of V_2O_5_80. The selected area electron diffraction (SAED), shown in the inset of Figures 7.3a and d, further confirms the polycrystalline nature of the fabricated V_2O_5_60 and V_2O_5_80, respectively. These results match well with the XRD structure shown in Figure 7.2b.

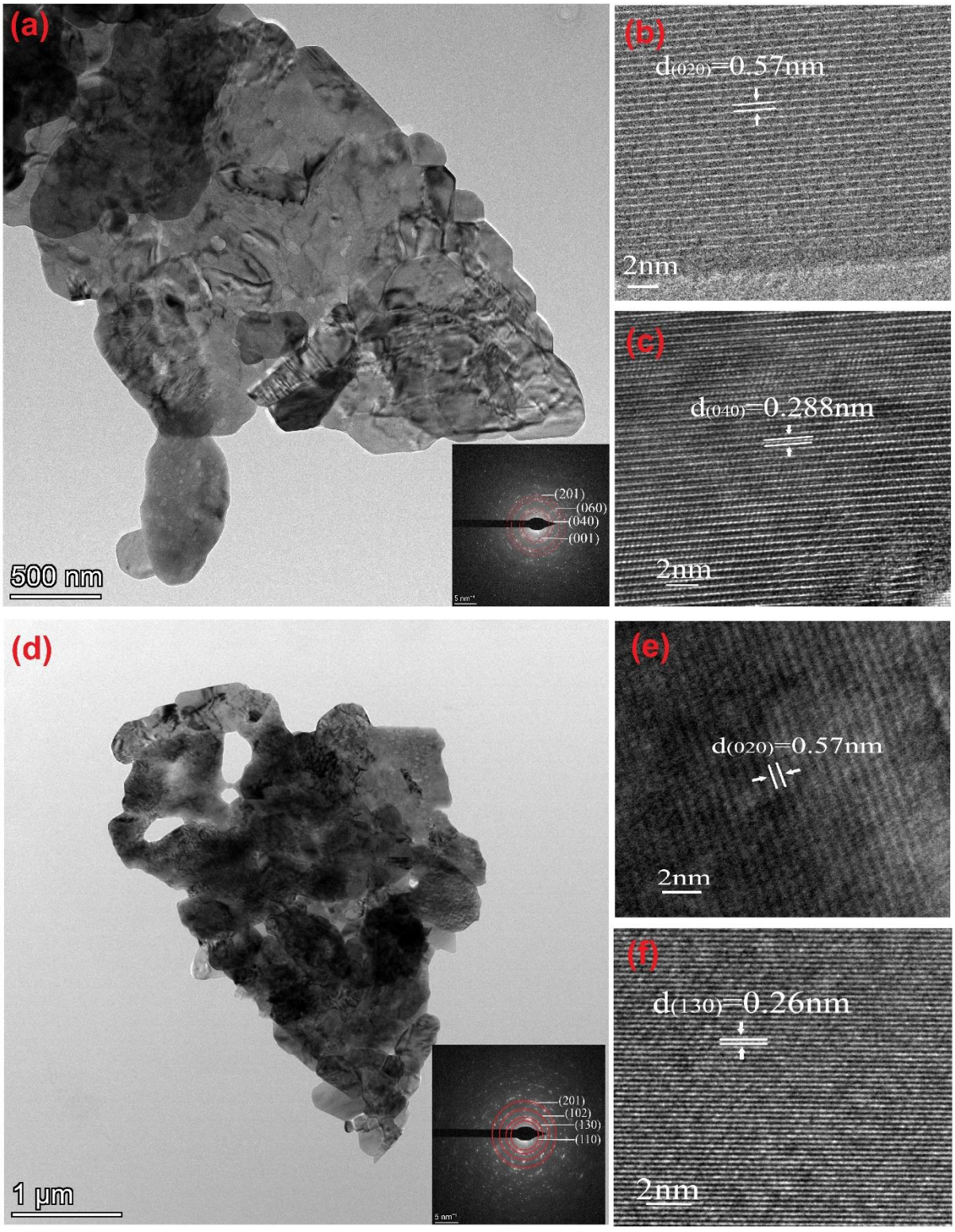
(a)
500 nm
(201)
(060)
(040)
(001)
(b)
d(020)=0.57nm
2nm
(c)
d(040)=0.288nm
2nm
(d)
1 μm
(201)
(102)
(130)
(110)
(e)
d(020)=0.57nm
2nm
(f)
d(130)=0.26nm
2nm

Figure 7.3 a) TEM images of V_2O_5_60, b and c) HRTEM images of V_2O_5_60, d) TEM images of V_2O_5_80, e and f) A high-resolution micrograph of V_2O_5_80 microsheet. The insets in (a) and (d) are selected area electron diffraction patterns of V_2O_5_60 and V_2O_5_80, respectively.

7.3 Electrochemical properties of V_2O_5

To further elucidate the charge and discharge characteristics of V_2O_5_60 and V_2O_5_80 microsheet, we conducted initial four cyclic voltammograms (CV) at 0.1 mV s^{-1} and galvanostatic charge and discharge profiles at 0.1 A g^{-1} within the voltage range of 0.01–3.0 V vs. Li/Li^+. Figures 7.4a and b depict CV curves of both samples during the initial, second, third and fourth cycles at a scan rate of 0.1 mV s^{-1}. Notably, the CV curves exhibit a relatively stable state after the initial cathodic scan, attributed to overlapping profiles in all anodic processes [3]. Furthermore, the first cycle reveals different redox peaks that disappear after the initial cycle within the voltage range of 0.01 to 3.0 V, suggesting potential multiple-phase transitions during redox processes, the formation of solid electrode interphase (SEI) film, and the influence of electrolyte reduction [3, 4]. These transitions include the transformation from α-$Li_xV_2O_5$ ($x < 0.01$) to ε-$Li_xV_2O_5$ ($0.35 < x < 0.7$), ε-$Li_xV_2O_5$ to δ-$Li_xV_2O_5$ ($0.7 < x < 1$), δ-$Li_xV_2O_5$ to γ-$Li_xV_2O_5$ ($1 < x < 2$), and γ-$Li_xV_2O_5$ to ω-$Li_xV_2O_5$ ($2 < x < 3$) between 0.01–3 V [5, 6]. Notably, the last redox peak exhibits high reversibility across all cycles, becoming the primary contributors to charge storage. Also, the overlapping curves from the second cycle indicate highly reversible electrochemical processes in the subsequent cycles and/or the establishment of a robust SEI layer. It is widely acknowledged that lithium storage primarily involves intercalation above 1.5 V, while below 1.5 V, decomposition and conversion reactions dominate [7]. Furthermore, ω-$Li_3V_2O_5$ may face challenges accommodating extra lithium ions while maintaining its high structural stability, and the additional capacity could potentially arise from a conversion reaction [7-9]. In contrast, recent research suggests that the disordered rock salt $Li_{3+x}V_2O_5$ could reversibly insert two lithium ions at approximately 0.6 V vs. Li/Li^+ [10]. Therefore, the reduction peak at around 0.5 V may be primarily attributed to either the conversion reaction or lithium insertion into $Li_{3+x}V_2O_5$ [10, 11].

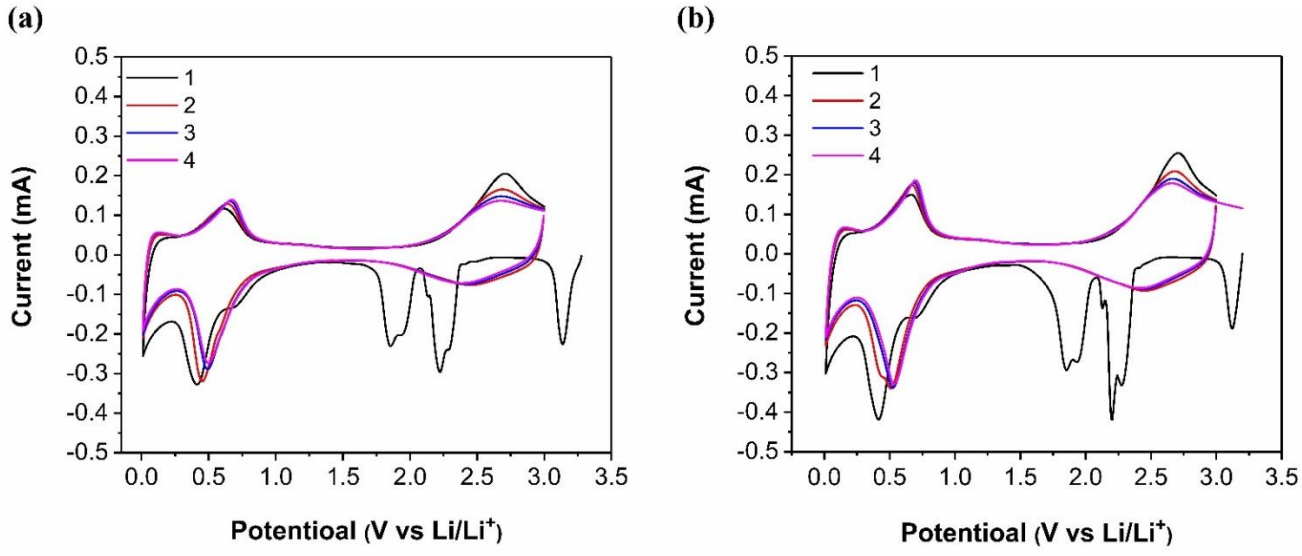

Figure 7.4 CV curve at a scan rate of 0.1 mV s^{-1} a) V_2O_5_60 and b) V_2O_5_80.

In the initial discharge process at 0.1 A g^{-1}, different lithiation plateaus appeared within the potential profile in the range of 0.01–3.0 V vs. Li/Li^+, indicating the multistep electrochemical reaction between V_2O_5_60 (or V_2O_5_80) and Li^+ due to multiple phase transitions (Figures 7.5a and b) [12]. These profiles demonstrate that the progression between the initial and subsequent charge/discharge curves matches the redox peaks observed in cyclic voltammograms. Voltage plateaus of both samples emerge at approximately 2.25 V, 2.15 V, 1.9 V, 0.8 and 0.5 V during the initial discharge profile due to phase transformations [13]. This significant shift in voltage profiles between the initial and subsequent cycles primarily results from their differing electrochemical responses to applied voltages and corresponding to the redox peaks identified in cyclic voltammograms. The discharge-charge profile at 0.1 A g^{-1} reveals capacity fading in the second discharge profile, attributed to an irreversible phase transition. Furthermore, Figures 7.5a and b exhibit the higher initial capacity for the V_2O_5_60 structure compared to V_2O_5_80.

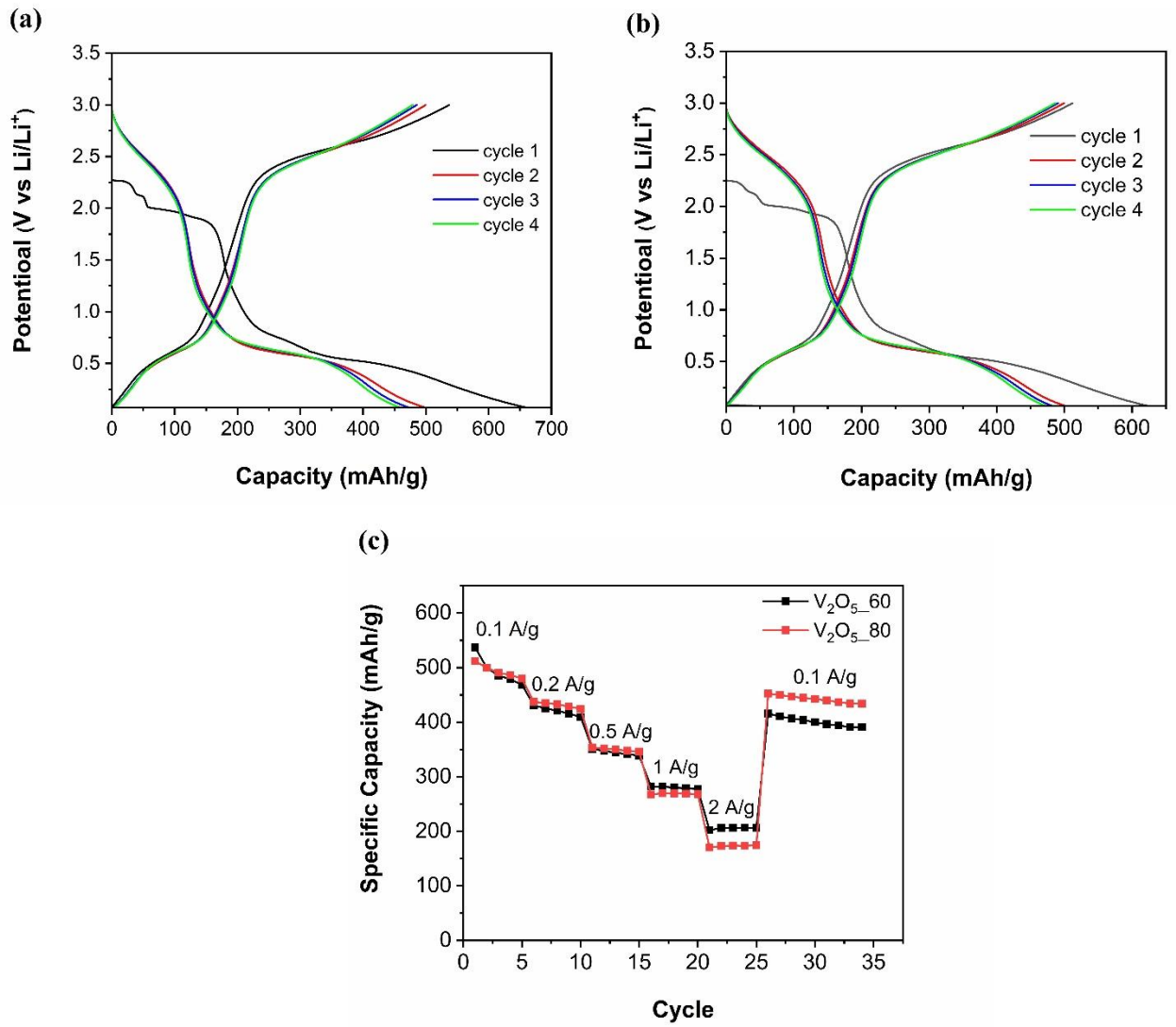

Figure 7.5 Galvanostatic charge and discharge profile of a) V_2O_5_60 at 0.1 A g^{-1} within the potential profile in the range of 0.01–3.0 V vs. Li/Li^+, b) V_2O_5_80 at 0.1 A g^{-1} within the potential profile in the range of 0.01–3.0 V vs. Li/Li^+, and c) Specific capacity versus cycle number at different current density.

Figure 7.5c illustrates the V_2O_5_60 and V_2O_5_80 performance at various current densities (ranging from 0.1 A g^{-1} to 2 A g^{-1}) for each current density in five cycles. The V_2O_5_60 microsheets exhibit a 2nd cycle capacity of 499.6 mA h g^{-1} at a current density of 0.1 A g^{-1}, gradually reducing to 425.3, 347, 281.9, and 206 mA h g^{-1} at 0.2, 0.5, 1, and 2 A g^{-1}, respectively. In contrast, the V_2O_5_80 microsheet demonstrates a capacity of 173 mA h g^{-1} at 2 A g^{-1}, even though its discharge capacities at 0.1, 0.2, 0.5, 1 A g^{-1} are approximately similar to those of V_2O_5_60 nanosheets. Following the high-rate measurement, the V_2O_5_60 and V_2O_5_80

microsheet electrode achieve a capacity of 415 and 452 mA h g^{-1} when the current density returns to 0.1 A g^{-1} in the 31st cycle. The reduction in capacity values at higher current densities is primarily attributed to limited ionic penetration [14]. The consistent performance over multiple cycles at each current density indicates good reversibility, with the V_2O_5_60 Li-ion anode showing better performance at 2 A g^{-1} compared to V_2O_5_80.

Figures 7.6a–d illustrates the cycling performance of V_2O_5_60 and V_2O_5_80 at 0.5 and 1.0 A g^{-1} within the potential range of 0.01–3.0 V vs. Li/Li^+. The initial capacities of V_2O_5_60 and V_2O_5_80 at 0.5 A g^{-1} were 462.4 and 426.6 mA h g^{-1}, respectively. Furthermore, the capacities of V_2O_5_60 and V_2O_5_80 at 1.0 A g^{-1} were 492 and 375.1 mA h g^{-1}, respectively. The capacity had a gradual decrease for the initial ~90 cycles at 0.5 A g^{-1} and ~160 cycles at 1.0 A g^{-1}, followed by a steady increase until stabilization. This behavior is commonly observed when using transition metal oxides as anodes for lithium-ion batteries and is often attributed to the formation of electrolyte-derived surface layers, interfacial charge storage, and/or surface redox reactions [15, 16]. Notably, the reversible specific capacity of V_2O_5_60 and V_2O_5_80 reached 340.7 and 351 mA h g^{-1}, respectively, after 505 cycles at 0.5 A g^{-1}, with a coulombic efficiency of >99%. Even after 1500 cycles at 1.0 A g^{-1}, V_2O_5_60 maintained a high capacity of 303.9 mA h g^{-1} with a coulombic efficiency ranging from 99% to 100%, while V_2O_5_80 exhibited a capacity of 149.4 mA h g^{-1}. The high Coulombic efficiencies demonstrate good reversibility between the discharge and charge processes.

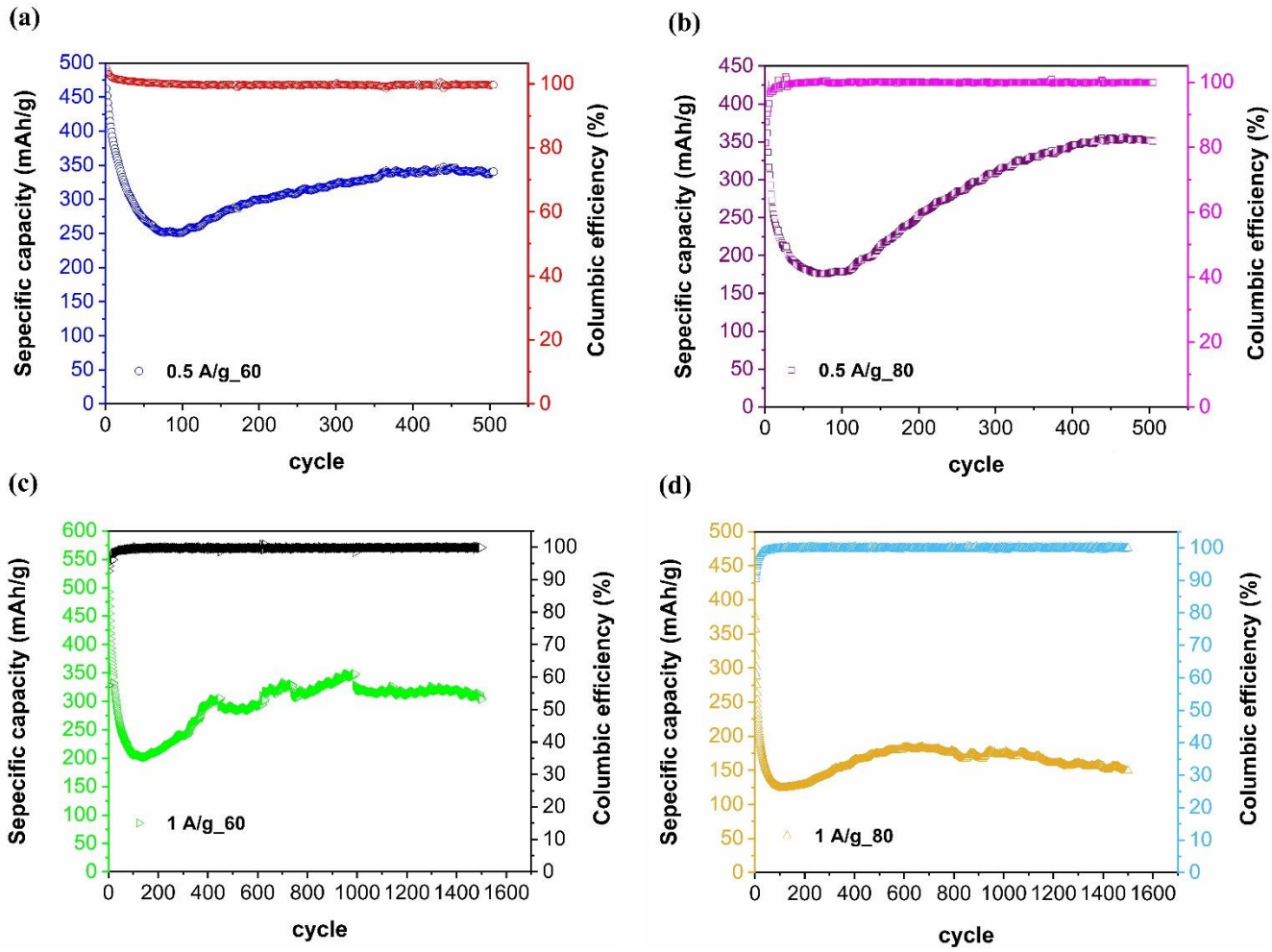

Figure 7.6 Capacity and coulombic efficiency of a) V_2O_5_60, b) V_2O_5_80 at 0.5 A g^{-1}, c) V_2O_5_60 and d) V_2O_5_80 at 1.0 A g^{-1}.

These results demonstrate the excellent Li^+ storage performance, higher cyclic ability, and good reversibility of the V_2O_5_60 nanosheet electrode at a high current density of 1 A g^{-1}. A comparison of the electrochemical performance of our porous V_2O_5 microsheets with reported V_2O_5 nanostructure materials is presented in Table 7.1. The outstanding cycling stability exhibited by the Li-ion battery anode using the V_2O_5 structure at 1 A g^{-1} within a voltage range of 0.01–3.0 V represents the best-reported performance to date. This remarkable achievement can be attributed mainly to the unique V_2O_5 microsheet structure.

Table 7.1 comparison of the electrochemical performance of lithium-ion batteries using V_2O_5-based anode.

Structure	Current density (A g^{-1})	Specific capacity (mA h g^{-1})	Number of cycle	Ref.
V_2O_5 hollow sphere	0.5	416	200	[11]
	3	260	400	
Hollow porous V_2O_5 microspheres	1	408	700	[17]
V_2O_5-SnO_2	0.25	673	50	[6]
Amorphous V_2O_5 films coating on graphene	1	519	200	[7]
V_2O_5 sheet network	0.1	600	40	[18]
Triple-hollow-shell structured V_2O_5	0.1	600	250	[19]
Core-shell structured V_2O_5@VO_2@V_2C@VC	0.5	252	200	[20]
Amorphous V_2O_5	0.1	600	50	[13]
V_2O_5 microspheres	1	206	500	[21]
V_2O_5 (Defect engineering)	2	175	500	[22]
V_2O_5 hierarchical structures	0.2	542	200	[23]
V_2O_5 micro sheet-60	0.5	340.7	505	This work
	1	303.9	1500	
V_2O_5 micro sheet-80	0.5	351	505	This work
	1	149.4	1500	

The influence of this structure on the rate capability is further explained by comparing the results of the electrochemical impedance spectrum (EIS) of the prepared porous V_2O_5_60 with V_2O_5_80. The Nyquist plots of both electrodes exhibit a high-frequency semicircle and a low-frequency line (Figure 7.7a). The intersection point on the Z' axis in the high-frequency region corresponds to the resistance of the electrolyte (R_s), while the diameter of the semicircles in the spectra represents the charge transfer resistances (R_{ct}) at the interface between the electrolyte and the electrode [24]. The R_{ct} value of V_2O_5_60 (111 ohms) is lower than that of V_2O_5_80 (137.8 ohms), indicating faster charge transfer in the V_2O_5_60 electrode. Therefore, reduced R_{ct} at the electrode/electrolyte interface can be attributed to an increased surface area between the active site and the electrolyte, facilitating a better ion diffusion and faster charge transfer in the V_2O_5_60 electrode compared to the V_2O_5_80 sample [5]. The porous structure of the V_2O_5 microsheet also proves beneficial for accommodating the change in volume during discharge/charge processes [25, 26].

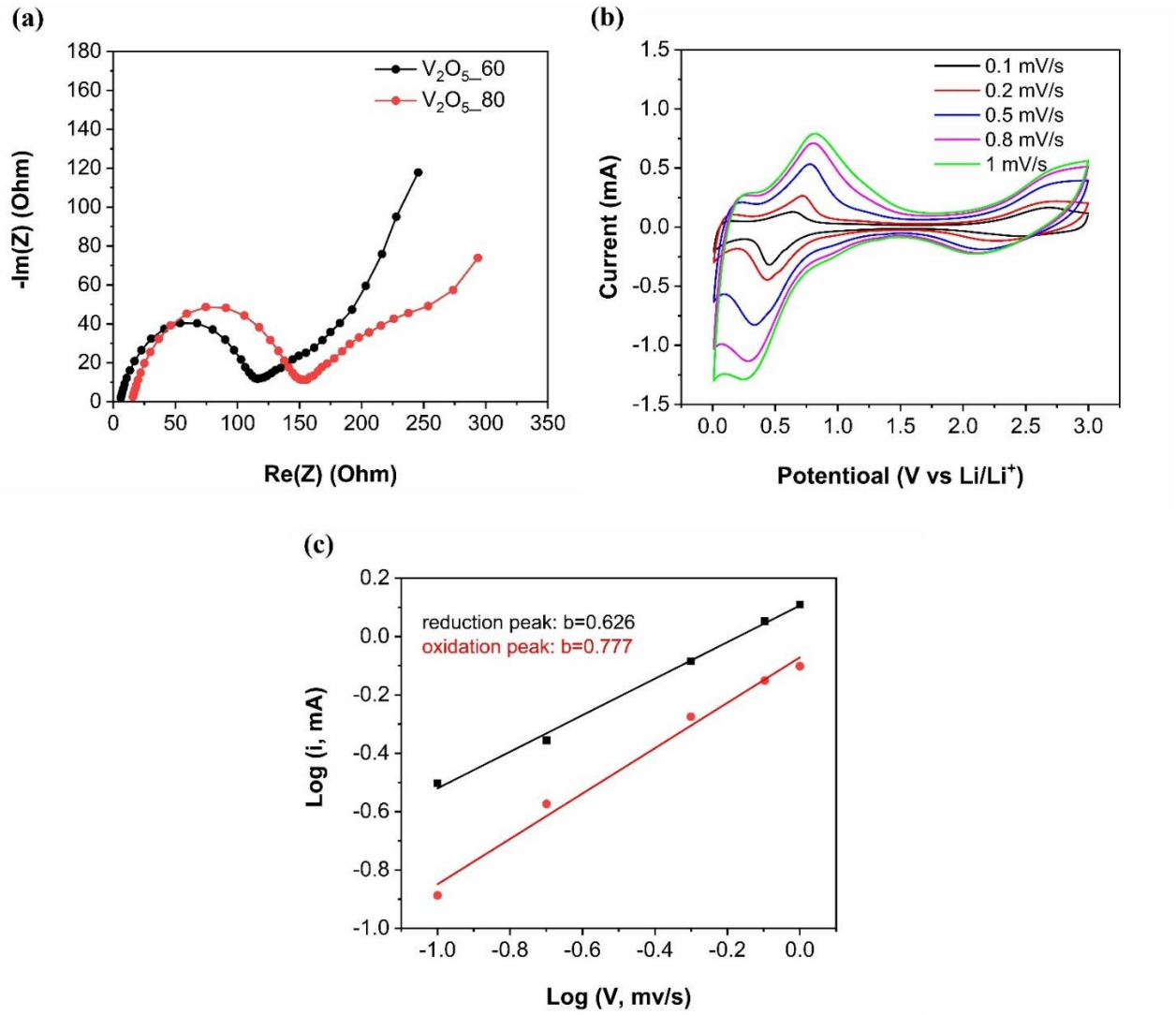

Figure 7.7 a) Nyquist plots of V_2O_5_60 and V_2O_5_80, b) CV curve of V_2O_5_60 at different scan rate and c) Logarithmic relationship between peak current intensity (i) and scan rate (υ) of V_2O_5_60.

To elucidate the mechanism of charge storage in V_2O_5_60, involving pseudocapacitive or faradaic behavior, we examined cyclic voltammograms at different scan rates, as illustrated in Figure 7.7b. All reduction peaks exhibited a negative shift, and the corresponding oxidation peaks shifted to a positive potential as the scan rate increased, accompanied by an increase in peak intensity. Previous reports have shown that the recorded peak current (i) in CV curves follows a power-law relationship with the scan rate (υ), expressed as $i=a\upsilon^b$ or $\log(i)=\log(a) + b \log(\upsilon)$, while the value of b serves as an indicator for interpreting the storage mechanism. Two

distinct conditions were established: the pseudocapacitive mechanism (b = 1.0) and the diffusion mechanism (b = 0.5) [27]. As illustrated in Figure 7.7c, derived slopes (b values) of 0.626 and 0.777 were obtained, differing from the well-defined conditions. This suggests the coexistence of the charge-storage mechanisms mentioned above during the electrochemical process. The CV curves are subjected to a theoretical model proposed by Dunn et al. This model demonstrates that the current density (i) at a given voltage is related to the two terms of the scan rates (υ) through the following equation [28].

$$i(V,\upsilon) = k_1(V)\,\upsilon + k_2(V)\,\upsilon^{1/2} \quad (1)$$

Dunn's method explains the capacity contribution by separating the cyclic voltammogram into diffusion ($k_2\upsilon^{1/2}$) and pseudocapacitive ($k_1\upsilon$) components (Equation 1) [29]. Figure 7.8a presents experimental CV analyses at a scan rate of 0.1 mV/s, with the light blue curve representing the experimental data. The diffusion contribution at this scan rate is depicted in grey. Bar plots in Figure 7.8b illustrate the capacitive and diffusion contributions. Pseudocapacitive behavior predominates across the explored scanning rates, exhibiting an increase with the scanning rate (Figure 7.8b). At the lower scanning rate of 0.1 mV/s, the device shows a minimal capacitive contribution of only 24%, while the predominant diffusion contribution makes up the remaining 76%. As the scan rate increases, there is a notable rise in the capacitive contribution and a decrease in the diffusion contribution. At the highest scan rate of 1 mV/s, the capacitive contribution is recorded as 56%, whereas the diffusion contribution measures 44%. This observation suggests that at lower scan rates, sufficient time is provided for the positive electrode (battery-grade) to complete the redox reaction, resulting in a larger diffusion contribution to the overall device capacity. Conversely, at higher scan rates, the capacitive-type electrode (negative) has enough time for the physical adsorption of charges at the electrode/electrolyte interface, leading to a more substantial capacitive contribution to the overall device performance. These findings provide insight into the possibility of a supercapattery concept, offering its ability to integrate characteristics from both supercapacitors and batteries [28, 30, 31].

The correlation between the peak current and the CV scan rate can be described using the Randles and Sevcik equation:

$$i_p = 2.06 \times 10^5 n^{\frac{3}{2}} A C_0 D^{\frac{1}{2}} v^{\frac{1}{2}} \quad (2)$$

Here, i_p denotes the peak current (A), n represents the charge-transfer number, A is the geometric area of the electrode (cm^2), C_0 is the molar concentration of Li^+ in the electrode (mol cm^{-3}), and υ is the scan rate (V/s). By analyzing the slope of i_p vs. $\upsilon^{1/2}$ plots in Figure 7.8c, the calculated diffusion coefficients (D_{Li^+}) for oxidation and reduction processes are 4.9×10^{-12} cm^2 s^{-1} and 2.2×10^{-12} cm^2 s^{-1}, respectively. These values are comparable to, or even superior to, the diffusion coefficients of V_2O_5 electrode structure in literature [32, 33]. The good D_{Li^+} values observed in V_2O_5_60 played a significant role in enhancing the rate capability of the material, as they facilitated the diffusion of Li^+ ions. They are approximately one order of magnitude higher than those obtained for the hollow structured Li_3VO_4 anode (2.37×10^{-13} cm^2 s^{-1}) [34], confirming the high rate capability of the V_2O_5-60 anode from a kinetics perspective.

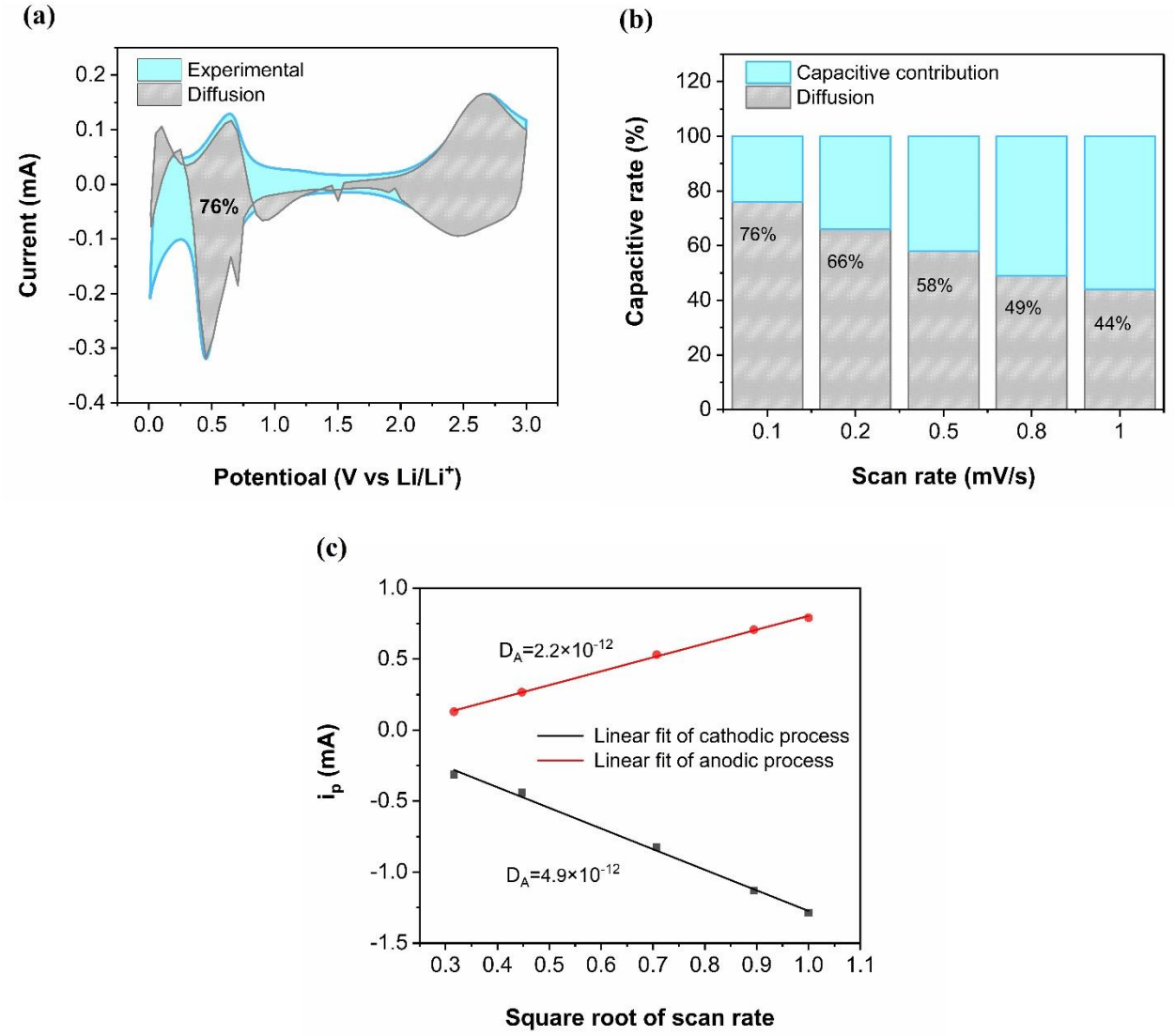

Figure 7.8 a) Experimental CV of the prepared V_2O_5_60 at 0.1 mV/s, b) Bar plots showing the capacitive and diffusive percentage at different scan rates and c) Relationship of the peak current (i_p) and the square root of scan rate ($\upsilon^{1/2}$) for V_2O_5_60.

Conclusion

In summary, this chapter investigated the electrochemical properties of V_2O_5 microsheets as an anode material for Li-ion batteries. The results demonstrated the superior performance of V_2O_5_60, characterized by excellent rate capability, cycling stability, and enhanced charge transfer kinetics, positioning it as a promising candidate for high-performance lithium-ion batteries.

References

[1] V.D. Mote, Y. Purushotham, B.N. Dole, Williamson-Hall analysis in estimation of lattice strain in nanometer-sized ZnO particles, Journal of Theoretical and Applied Physics, 6 (2012) 6.

[2] G. Madras, B.J. McCoy, Temperature effects during Ostwald ripening, The Journal of Chemical Physics, 119 (2003) 1683-1693.

[3] X. Wang, Y. Huang, D. Jia, W.K. Pang, Z. Guo, Y. Du, X. Tang, Y. Cao, Self-Assembled Sandwich-like Vanadium Oxide/Graphene Mesoporous Composite as High-Capacity Anode Material for Lithium Ion Batteries, Inorganic Chemistry, 54 (2015) 11799-11806.

[4] Y. Li, J. Yao, E. Uchaker, J. Yang, Y. Huang, M. Zhang, G. Cao, Leaf-Like V_2O_5 Nanosheets Fabricated by a Facile Green Approach as High Energy Cathode Material for Lithium-Ion Batteries, Advanced Energy Materials, 3 (2013) 1171-1175.

[5] Y. Yue, H. Liang, Micro- and Nano-Structured Vanadium Pentoxide (V_2O_5) for Electrodes of Lithium-Ion Batteries, Advanced Energy Materials, 7 (2017) 1602545.

[6] J. Liu, H. Xia, D. Xue, L. Lu, Double-Shelled Nanocapsules of V_2O_5-Based Composites as High-Performance Anode and Cathode Materials for Li Ion Batteries, Journal of the American Chemical Society, 131 (2009) 12086-12087.

[7] X. Sun, C. Zhou, M. Xie, T. Hu, H. Sun, G. Xin, G. Wang, S.M. George, J. Lian, Amorphous vanadium oxide coating on graphene by atomic layer deposition for stable high energy lithium ion anodes, Chemical Communications, 50 (2014) 10703-10706.

[8] V. Augustyn, B. Dunn, Low-potential lithium-ion reactivity of vanadium oxide aerogels, Electrochimica Acta, 88 (2013) 530-535.

[9] P. Liu, S.-H. Lee, C.E. Tracy, J.A. Turner, Stable cycling of thin-film vanadium oxide electrodes between 4 and 0 V in lithium batteries, Journal of Power Sources, 119-121 (2003) 305-309.

[10] H. Liu, Z. Zhu, Q. Yan, S. Yu, X. He, Y. Chen, R. Zhang, L. Ma, T. Liu, M. Li, R. Lin, Y. Chen, Y. Li, X. Xing, Y. Choi, L. Gao, H.S.-y. Cho, K. An, J. Feng, R. Kostecki, K. Amine, T. Wu, J. Lu, H.L. Xin, S.P. Ong, P. Liu, A disordered rock salt anode for fast-charging lithium-ion batteries, Nature, 585 (2020) 63-67.

[11] B. Yan, X. Li, X. Fu, L. Zhang, Z. Bai, X. Yang, An elaborate insight of lithiation behavior of V_2O_5 anode, Nano Energy, 78 (2020) 105233.

[12] Y. Tang, X. Rui, Y. Zhang, T.M. Lim, Z. Dong, H.H. Hng, X. Chen, Q. Yan, Z. Chen, Vanadium pentoxide cathode materials for high-performance lithium-ion batteries enabled by a hierarchical nanoflower structure via an electrochemical process, Journal of Materials Chemistry A, 1 (2013) 82-88.

[13] O.B. Chae, J. Kim, I. Park, H. Jeong, J.H. Ku, J.H. Ryu, K. Kang, S.M. Oh, Reversible Lithium Storage at Highly Populated Vacant Sites in an Amorphous Vanadium Pentoxide Electrode, Chemistry of Materials, 26 (2014) 5874-5881.

[14] M.L. Divya, S. Natarajan, Y.S. Lee, V. Aravindan, Highly perforated V_2O_5 cathode with restricted lithiation toward building “rocking-chair” type cell with graphite anode recovered from spent Li-ion batteries, Small, 16 (2020) 2002624.

[15] H. Sun, G. Xin, T. Hu, M. Yu, D. Shao, X. Sun, J. Lian, High-rate lithiation-induced reactivation of mesoporous hollow spheres for long-lived lithium-ion batteries, Nature Communications, 5 (2014) 4526.

[16] Y. Dou, J. Xu, B. Ruan, Q. Liu, Y. Pan, Z. Sun, S.X. Dou, Atomic Layer-by-Layer Co_3O_4/Graphene Composite for High Performance Lithium-Ion Batteries, Advanced Energy Materials, 6 (2016) 1501835.

[17] L. Xue, Y. Li, W. Lin, F. Chen, G. Chen, D. Chen, Electrochemical properties and facile preparation of hollow porous V_2O_5 microspheres for lithium-ion batteries, Journal of Colloid and Interface Science, 638 (2023) 231-241.

[18] Y. Xu, M. Dunwell, L. Fei, E. Fu, Q. Lin, B. Patterson, B. Yuan, S. Deng, P. Andersen, H. Luo, Two-dimensional V_2O_5 sheet network as electrode for lithium-ion batteries, ACS applied materials & interfaces, 6 (2014) 20408-20413.
[19] C. Wang, L. Zhang, M. Al-Mamun, Y. Dou, P. Liu, D. Su, G. Wang, S. Zhang, D. Wang, H. Zhao, A Hollow-Shell Structured V_2O_5 Electrode-Based Symmetric Full Li-Ion Battery with Highest Capacity, Advanced Energy Materials, 9 (2019) 1900909.
[20] R.J. Liu, L.X. Yang, G.Q. Lin, H.P. Bu, W.J. Wang, H.J. Liu, C.L. Zeng, Superior electrochemcial performances of core–shell structured vanadium oxide@ vanadium carbide composites for Li-ion storage, Applied Surface Science, 588 (2022) 152904.
[21] L.-Q. Yu, S.-X. Zhao, X. Wu, Q.-L. Wu, J.-W. Li, E.-L. Zhao, Effects of vanadium pentoxide with different crystallinities on lithium ion storage performance, CrystEngComm, 21 (2019) 6641-6651.
[22] M. Hu, Z. Liu, H. Zhang, Z.-H. Huang, F. Kang, R. Lv, Defect engineering of vanadium pentoxide for efficient lithium-ion storage, Electrochimica Acta, 333 (2020) 135513.
[23] L. Du, H. Lin, Z. Ma, Q. Wang, D. Li, Y. Shen, W. Zhang, K. Rui, J. Zhu, W. Huang, Using and recycling V_2O_5 as high performance anode materials for sustainable lithium ion battery, Journal of Power Sources, 424 (2019) 158-164.
[24] Q. Xiong, J. Tu, Y. Lu, J. Chen, Y. Yu, Y. Qiao, X. Wang, C. Gu, Synthesis of hierarchical hollow-structured single-crystalline magnetite (Fe_3O_4) microspheres: the highly powerful storage versus lithium as an anode for lithium ion batteries, The Journal of Physical Chemistry C, 116 (2012) 6495-6502.
[25] H. Song, C. Zhang, Y. Liu, C. Liu, X. Nan, G. Cao, Facile synthesis of mesoporous V_2O_5 nanosheets with superior rate capability and excellent cycling stability for lithium ion batteries, Journal of Power Sources, 294 (2015) 1-7.
[26] Q. An, P. Zhang, Q. Wei, L. He, F. Xiong, J. Sheng, Q. Wang, L. Mai, Top-down fabrication of three-dimensional porous V_2O_5 hierarchical microplates with tunable porosity for improved lithium battery performance, Journal of Materials Chemistry A, 2 (2014) 3297-3302.
[27] M.R. Lukatskaya, S. Kota, Z. Lin, M.-Q. Zhao, N. Shpigel, M.D. Levi, J. Halim, P.-L. Taberna, M.W. Barsoum, P. Simon, Ultra-high-rate pseudocapacitive energy storage in two-dimensional transition metal carbides, Nature Energy, 2 (2017) 1-6.
[28] M.Z. Iqbal, M.M. Faisal, M. Sulman, S.R. Ali, A.M. Afzal, M.A. Kamran, T. Alharbi, Capacitive and diffusive contribution in strontium phosphide-polyaniline based supercapattery, Journal of Energy Storage, 29 (2020) 101324.
[29] S. Fleischmann, J.B. Mitchell, R. Wang, C. Zhan, D.-e. Jiang, V. Presser, V. Augustyn, Pseudocapacitance: From Fundamental Understanding to High Power Energy Storage Materials, Chemical Reviews, 120 (2020) 6738-6782.
[30] M.Z. Iqbal, J. Khan, S. Alam, R. Ali, M.J. Iqbal, A.M. Afzal, S. Aftab, Enhanced electrochemical performance of battery-grade cobalt phosphate via magnetron sputtered copper interfacial layer for potential supercapattery applications, International Journal of Energy Research, 45 (2021) 18658-18669.
[31] H. Chen, J. Zhou, Q. Li, S. Zhao, X. Yu, K. Tao, Y. Hu, L. Han, MOF-assisted construction of a Co_9S_8@Ni_3S_2/ZnS microplate array with ultrahigh areal specific capacity for advanced supercapattery, Dalton Transactions, 49 (2020) 10535-10544.
[32] X. Ren, C. Shi, P. Zhang, Y. Jiang, J. Liu, Q. Zhang, An investigation of V_2O_5/polypyrrole composite cathode materials for lithium-ion batteries synthesized by sol–gel, Materials Science and Engineering: B, 177 (2012) 929-934.
[33] H. Yu, X. Rui, H. Tan, J. Chen, X. Huang, C. Xu, W. Liu, D.Y.W. Yu, H.H. Hng, H.E. Hoster, Q. Yan, Cu doped V_2O_5 flowers as cathode material for high-performance lithium ion batteries, Nanoscale, 5 (2013) 4937-4943.

[34] Y. Shi, J.-Z. Wang, S.-L. Chou, D. Wexler, H.-J. Li, K. Ozawa, H.-K. Liu, Y.-P. Wu, Hollow structured Li_3VO_4 wrapped with graphene nanosheets in situ prepared by a one-pot template-free method as an anode for lithium-ion batteries, Nano letters, 13 (2013) 4715-4720.

Chapter 8: Conclusion

This comprehensive research addressed diverse aspects in the synthesis and applications of metal oxide materials. The first study demonstrated the synthesis of WO_3 nanopowder using an environmentally friendly method, employing water as the solvent and vitamin C as a surfactant. The morphological analysis revealed that vitamin C plays a dual role as a mild reducing and capping agent, facilitating the formation of WO_3 nanoparticles without agglomeration. Although the influence of potassium sulfate on particle formation was investigated, the experimental results indicated that vitamin C was more effective as a capping agent. Furthermore, careful control of the reaction time was essential to prevent particle agglomeration and ensure the desired morphology. Compositional and structural analyses confirmed the formation of WO_3 monoclinic, which is crucial for the material's high and selective response to acetone. The sensor response is significantly enhanced with increasing operating temperature, attributed to improved adsorption of environmental oxygen on the WO_3 surface and the high activation energy required for the chemisorption of acetone and its subsequent decomposition into CO_2 and H_2O. Remarkably, the fabricated sensing structure demonstrated the ability to detect 200 ppb of acetone without the need for doping or functionalization with specific materials, as well as without the addition of noble metal catalysts. Even at 90% relative humidity, the sensor exhibits a considerably good and stable response to acetone, highlighting its robust performance in various environmental conditions. Overall, the results presented in this study offer valuable insights into the green synthesis of WO_3 nanomaterials and the development of acetone sensors. These findings not only contribute to the advancement of sensor technology but also hold promise for addressing environmental and health-related challenges associated with acetone detection in industrial and clinical settings.

Another study investigated the synthesis and gas sensing properties of WO_3_P_1 and WO_3_P_2 nanostructures. By employing a sol-gel method with benzyl alcohol as the solvent and WCl_6 as the precursor, we successfully synthesized WO_3 nanostructures with and without the presence of PEG 200 as a surfactant. Through comprehensive morphological and structural analyses using FESEM, TEM, XRD, Raman spectroscopy, and ATR-IR spectroscopy, we gained insights into the crystalline structure, morphology, and chemical composition of the synthesized materials. Our findings revealed that the presence of PEG 200 in the synthesis process significantly influenced

the crystallinity and morphology of WO_3_P_2, leading to the formation of larger aggregates with an irregular shape compared to WO_3_P_1. The XRD and Raman spectroscopy results confirmed the coexistence of orthorhombic and monoclinic phases in WO_3_P_2, whereas only the monoclinic phase was detected in WO_3_P_1. Additionally, ATR-IR analysis indicated the presence of residual PEG 200 in WO_3_P_2, which may have contributed to the enhancement of its conductivity. Regarding gas sensing performance, WO_3_P_2 exhibited superior sensitivity to acetone compared to WO_3_P_1, particularly at elevated temperatures (300−400 °C). The enhanced sensitivity of WO_3_P_2 to acetone can be attributed to the inhibition of hydrate formation and the presence of ortho/mono n-n homojunctions, which facilitated improved acetone adsorption. Furthermore, both WO_3_P_1 and WO_3_P_2 demonstrated consistent gas sensing performance at different humidity levels (40−95%), indicating their potential for breath analysis applications. The comparison with other semiconductor gas sensors highlighted the significant impact of WO_3 nanostructure and crystalline modification on gas sensing performance. Overall, the findings presented in this study contribute to advancing our understanding of the synthesis and gas sensing properties of WO_3 nanostructures, paving the way for the development of high-performance chemical sensors for various applications, including environmental monitoring and healthcare. While our study offers important insights into material synthesis and characterization, further investigation is needed to understand the formation and effect of ortho/mono heterojunctions on sensitivity. Our collaborators are conducting UPS, XPS analysis, and DFT calculations, which will provide a deeper understanding of sensor mechanisms.

Furthermore, another study presents a novel approach utilizing ethylene glycol as both a solvent and capping agent to control the morphology and crystallization of bare metal oxides, specifically focusing on hierarchical copper oxide (CuO) structures, porous zinc oxide (ZnO), and their composites. Through a straightforward and environmentally friendly polyol process, hierarchical CuO structures and porous ZnO were successfully synthesized, with CuO-ZnO composites also being fabricated via a simple procedure involving the dissolution of an organocopper precursor in isopropanol followed by heating after mixing with a prepared zinc oxide precursor. The morphological analyses using scanning electron microscopy (SEM) revealed

distinct properties of CuO, ZnO, and CuO-ZnO composites, with CuO exhibiting microsphere hierarchical structures and ZnO displaying a porous rod-like morphology. CuO-ZnO composites showed a combination of CuO sphere-like components and porous ZnO particles. Structural investigations confirmed the formation of crystalline monoclinic CuO and hexagonal ZnO, with CuO-ZnO composites closely resembling pure ZnO in their diffraction patterns, albeit with additional peaks indicating the presence of monoclinic CuO. The determination of band gaps using Tauc's method yielded values of 1.25 eV for CuO and 3.09 eV for ZnO, with the presence of CuO in the composite reducing the band gap, suggesting enhanced gas sensing performance. Gas sensing measurements conducted for NO_2 at various temperatures and humidity levels demonstrated the significant influence of both parameters, with CuO-ZnO composites showing enhanced responses at higher humidity levels. Selectivity studies further indicated excellent selectivity toward NO_2, highlighting the potential of CuO-ZnO composites as materials for NO_2 gas sensing. Overall, the findings of this study underscore the potential of CuO-ZnO composites as efficient and reliable materials for NO_2 gas sensing applications, contributing to the development of advanced gas sensors for industries and environmental monitoring. Moving forward, further research could explore optimization strategies to enhance the sensitivity and selectivity of these composites, as well as investigate their performance in real-world environments for practical application.

The final study explored the application of V_2O_5 as a promising anode material for lithium-ion batteries. Through the synthesis of V_2O_5_60 and V_2O_5_80 via the precipitation method at various reaction temperatures, coupled with comprehensive characterization techniques including XRD and morphological studies, crystalline V_2O_5 with distinct porous microsheet structures was successfully fabricated. Electrochemical measurements, including cyclic voltammetry (CV) and galvanostatic charge-discharge cycles, elucidated multiple phase transitions within the materials. Comparative analyses against other V_2O_5 nanostructures underscored the exceptional cycling stability achieved by V_2O_5_60 microsheets, particularly at 1.0 A/g, positioning it as one of the highest-performing V_2O_5-based anodes reported to date. Electrochemical impedance spectroscopy (EIS) further unveiled faster charge transfer kinetics in V_2O_5_60, facilitating enhanced ion diffusion. Further exploration into the charge storage

mechanism revealed a delicate interplay between pseudocapacitive and diffusion-controlled behaviors, suggesting the potential for a supercapattery that combines the characteristics of supercapacitors and batteries. This research not only highlights the promise of V_2O_5_60 as a high-performance anode material but also underscores the pivotal role of microstructural engineering in advancing efficient energy storage systems. The research proposed future research directions, including optimization strategies and the exploration of doping effects. Overall, this research makes noteworthy contributions to the field of energy storage technologies.

Furthermore, $ZnWO_4$-ZnO and $CuWO_4$-WO_3 composite materials were also successfully synthesized via the sol-gel method. The $ZnWO_4$-ZnO composites were prepared with various concentrations of $ZnWO_4$ and reaction times. Similarly, $CuWO_4$-WO_3 composites were synthesized with different copper precursor concentrations (10%, 15%, and 20%). These composite materials will be further investigated for their gas sensing properties in future work, exploring their potential applications in gas sensing technology.

In summary, this thesis provides valuable insights into the synthesis, properties, and applications of advanced materials, contributing to the fields of gas sensing and energy storage. The findings underscore the significance of environmentally friendly synthesis methods and microstructural engineering in enhancing the performance of functional materials for various technological applications.

List of Publications

1. **Hakimeh Pakdel**, Vardan Galstyan, Annalisa D'Arco, Tiziana Mancini, Stefano Lupi, Abderrahim Moumen, Matteo Borsi, Elisabetta Comini, Synthesis of WO_3 nanopowder using a green surfactant for efficient gas sensing applications, Ceramics International, 2023, https://doi.org/10.1016/j.ceramint.2023.06.314.
2. **Hakimeh Pakdel**, Matteo Borsi, Massimo Ponzoni, Elisabetta Comini, Enhanced Gas Sensing Performance of CuO-ZnO Composite Nanostructures for Low-Concentration NO_2 Detection, Chemosensor, 2024,12,54, https://doi.org/10.3390/chemosensors12040054.
3. **Hakimeh Pakdel**, Vardan Galstyan, Viacheslav Golovanov, Annalisa D'Arco, Tiziana Mancini, Stefano Lupi, Elisabetta Comini, Theoretical and experimental studies of WO_3 for highly selective gas sensing application (Submitted).
4. **Hakimeh Pakdel**, Yanshen Liu, Vardan Galstyan, Nicola Pinna, Elisabetta Comini, Exploring V_2O_5 as an Anode Material for Lithium-Ion Batteries: Synthesis, Characterization, and Electrochemical Performance (Submitted).
5. Hadjer Hakkoum, **Hakimeh Pakdel**, Dario Zappa, Elisabetta Comini, Simple synthesis of hematite iron oxide nanoparticles for sensing application (Under preparation).

Conference

1. Oral Presentation title “Green synthesis of WO_3 nanomaterial and their gas sensing properties” **Hakimeh Pakdel***, Vardan Galstyan, Elisabetta Comini, NANOTECH FRANCE\NANOMATEN\GAMS\NANOMETROLOGY 2023 INTERNATIONAL JOINT CONFERENCES, 28 - 30 June 2023, Paris, France.
2. Presented poster title “ Simple synthesis of hematite iron oxide nanoparticles via polyol method for sensing application” **Hadjer Hakkoum***, **Hakimeh Pakdel**, Dario Zappa, Elisabetta Comini, Eurosensors XXXV conference, 10-13 September 2023, Lecce, Italy.
3. Oral Presentation title “Synthesis and characterization of composite structure based on zinc and copper oxides for gas sensing applications” **Hakimeh Pakdel***, Vardan Galstyan,

Matteo Borsi, Elisabetta Comini, the European Materials Research Society (E-MRS) conference, 18-21 September 2023, Warsaw, Poland.

4. Oral Presentation title " Synthesis of WO_3 Nanomaterials and Their Chemical Sensing Properties" **Hakimeh Pakdel***, Vardan Galstyan, Elisabetta Comini, From surfaces to devices: novel perspectives from nanostructured oxides and carbon materials, international workshop, Brescia, December 12, 2022.
5. Oral Presentation title "Metal Oxides Nanowires for Chemical Sensing and Solid Oxide Fuel Cell Applications", Navpreet Kaur, Mandeep Singh, Gayan Chathuranga Kumarage Wadumesthree, Abderrahim Moumen, **Hakimeh Pakdel**, Dario Zappa, Vardan Galstyan, **Elisabetta Comini***, TCM-TOEO 2022, 16^{th} -21^{st} October 2022, Crete, Greece.
6. Oral Presentation title "Synthesis of metal oxide nanoparticles using precipitation method and their chemical sensing properties" **Hakimeh Pakdel***, V. Galstyan, N. Poli, E. Comini, XXI Conferenza Nazionale Sensori e Microsistemi (AISEM2022), Roma, February 10-11, 2022.
7. Oral Presentation title "Metal Oxides Nanostructures: Achievements and Advances in Chemical Sensing" **Elisabetta Comini***, Abderrahim Moumen, Giorgio Duina, Vardan Galstyan, Navpreet Kaur, Gayan Chathuranga Kumarage Wadumesthree, **Hakimeh Pakdel**, Mandeep Singh and Dario Zappa, NANOMEET2021, INTERNATIONAL MEET ON NANOTECHNOLOGY, PORTO, PORTUGAL, SEPTEMBER 13-15, 2021.

MODULO DI EMBARGO DELLA TESI

(da compilare solo se si richiede un periodo di segretazione della tesi)

Il/La sottoscritto/a……Hakimeh Pakdel…… Nato/a il……01/07/1995……

a (indicare anche l'eventuale paese estero)……Iran……

provincia di (ovvero sigla del paese estero)……Kazeroon(Città)……

Dottorato di Ricerca in ……Information Engineering……

DICHIARA

- che il contenuto della tesi **non può essere immediatamente consultabile per il seguente motivo**

Non ho ancora pubblicato tutti gli articoli che utilizzano i dati presenti nella tesi. La consultazione ritardata è necessaria per assicurare che i dati vengano pubblicati sulle riviste accademiche correttamente.

La motivazione deve essere dettagliata e controfirmata obbligatoriamente dal Primo Supervisore di tesi

(Brevetto, segreto industriale, motivi di priorità nella ricerca, motivi editoriali, altro)

- che il testo completo della tesi potrà essere reso consultabile dopo:

□ 6 mesi dalla data di conseguimento titolo

x 12 mesi dalla data di conseguimento titolo

- che sarà comunque consultabile immediatamente l'abstract della tesi, che viene caricato in Esse3, profilo studente.

Luogo e Data Brescia, 09/07/2024

Firma del Dichiarante

hakimeh
Pakdel
09.07.2024
12:19:43
GMT+01:00

Controfirma del Primo Supervisore di tesi

per la motivazione di embargo e il periodo.

Firmato digitalmente da Elisabetta Comini
Data: 09.07.2024 13:15:02 CEST
Organizzazione: UNIVERSITA' DEGLI STUDI DI BRESCIA/0177371017